POLITECNICO DI MILANO

Aerospace Science and Technology Department

Doctoral Program in Aerospace Engineering – XXVII

ENTRAINMENT EFFECTS ON COMBUSTION PROCESSES IN PARAFFIN-BASED HYBRID ROCKET MOTORS

Supervisor:
Prof. Luciano GALFETTI

Head of the Doctoral Program:
Prof. Luigi VIGEVANO

Doctoral Dissertation of:
Praskovia MILOVA

June 2015

ABSTRACT

Let's go find out!

Hybrid rocket motors have been an active area of research for many years due to the potential best-of-both-worlds which they offer by leveraging the favorable aspects of both liquid and solid rockets respectively. Compared to traditional liquid- and solid-fuel rocket motors, hybrid rocket motors offer a number of distinct advantages such as reduced mechanical complexity, the possibility of throttling and restart, and reduced fire and explosion risk. In spite of these advantages and many years of research, hybrid rocket motors have gone largely unused in space exploration due in large part to the inherently low regression rate of the solid fuel grain. While the regression rate effect can be partially ameliorated through geometrical changes in the fuel grain's design, this can lead to problems like inadequate structural strength of the fuel grain and insufficient volumetric efficiency.

Recently, a new type of hybrid rocket fuel has been proposed which uses paraffin as its base. Laboratory studies of this fuel have shown 3-4 times better regression rate performance compared to conventional fuels. The reason for this improved performance is believed to be the result of the fuel melting to form a liquid film layer which can then be entrained as droplets by the high-speed oxidizer flowing across its surface. These entrained fuel droplets may offer increased fuel surface area with which the oxidizer can react but the fact that they are entrained may mean that significant fuel mass is lost through the motor nozzle before it can be burned for thrust. Additionally, paraffin-based fuels may lack the mechanical strength and toughness to be considered for space flight applications. Fuel additives that strengthen and toughen the fuel grain may affect the viscosity of the melted fuel layer and affect how it becomes entrained in the oxidizer. These processes and interactions are not yet well understood and they must be investigated thoroughly before the benefits of these fuels can be translated to real-world design applications.

This work attempts to resolve several of the key unknowns affecting hybrid rocket design in two phases: first, materials testing to determine the effect of composition changes on the strength of the solid fuel, its melting point, and its viscosity once melted. Second, a CFD modeling strategy was developed for simulating a lab-scale hybrid rocket motor. The CFD model was used to study the sensitivity of the motor's performance to changes in the characteristics in the entrained flow like droplet size, global mixture oxidizer-to-fuel ratio, and the fraction of fuel entrained. These quantities were calculated using empirical and analytical relations available in the literature and imposed as boundary conditions in the CFD model. The results show that the presence of the fuel droplets pushes the reaction zones farther downstream, particularly for larger particles. As a consequence, for design purposes the either the mass of the unburned particles would have to be accounted for or the length of the motor would have to be

changed to allow for more complete droplet evaporation/combustion thus obtaining higher combustion efficiency.

This work gives a significant contribution in the computational modeling of hybrid rockets flowfields, with special attention to the entrainment phenomenon description, which is the most relevant physical aspect in the combustion behavior of low melting temperature fuels recently proposed to improve hybrid rocket technology.

ACKNOWLEDGEMENTS

I would like to, first of all, thank my Ph.D. supervisor, Prof. Luciano Galfetti, who was supporting and guiding me through my research with his knowledge, experience and a kind heart. It was a great pleasure to be part of the world-famous Space Propulsion Laboratory (SPLab), and to learn from the best experts in the field.

Second, I want to acknowledge the members of the committee who considered my application to the Doctoral Program at Politecnico di Milano, and who ranked my application high enough that I was not just given this fantastic opportunity, so I was admitted to the program with a scholarship.

A special gratitude I address to the combustion group at NUMECA Int, Brussels, who provided me with great support through the numerical investigation, and gave me the opportunity to significantly extend my knowledge of CFD. Jan Anker is the head of the combustion group. I also appreciate the license of FINE^{TM}/Open that was kindly granted by Colinda Goormans-Francke, so I was able to continue working even after the period as a visiting researcher was over.

CONTENTS

LIST OF FIGURES

LIST OF TABLES

NOMENCLATURE

Acronyms and abbreviations

CB	Carbon black
DSC	Differential scanning calorimetry
HRM	Hybrid Rocket Motor
HTPB	Hydroxyl-terminated polybutadiene
KH	Kelvin-Helmholtz
KR	Kossiakoff and Rice
MA	Maleic anhydride
SEBS	Polystyrene-block-poly(ethylene-ran-butylene)-block-polystyrene-graft-maleic anhydride
SEBSx	Paraffin-based fuel containing x% of SEBS TPP, and 1% of Carbon black
SIS	Polystyrene-block-polyisoprene-block-polystyrene
SISx	Paraffin-based fuel containing x% of SIS TPP, and 1% of Carbon black
SW	Solid wax / Paraffin-wax
TPP	Thermoplastic Polymer

Greek symbols

α	Phase shift between stress σ_0 and strain ε_0
γ	Ratio of specific heats
δ	Size distribution parameter
ε	Emissivity
ε_{nozzle}	Nozzle expansion area ratio
ε_0	Amplitude of strain
ε_{mech}	Strain (mechanical properties)
ϵ	Turbulence dissipation rate
ϑ	Volume fraction of droplets
μ	Dynamic Viscosity
μ_T	Turbulent or eddy viscosity
μ^*	Complex viscosity
ρ	Density
σ	Stefan-Boltzmann Constant
σ_0	Amplitude of stress
σ_l	Surface tension
σ_{mech}	Stress (mechanical properties)

Latin symbols

a	Parameter in upper-limit (Eq. 4–21)
A	Cross-sectional area
A_K	Pre-exponential coefficient
c^*	Characteristic velocity
C_p	Specific heat
C_μ	Turbulence model $(k-\epsilon)$ parameter
d	Derivative (Eq. 4–20)
d	Droplet diameter
D	Diameter of the post-combustion chamber
d_h	Hydraulic diameter of the fuel port
d_{vm}	Volume median droplet diameter
d_{max}	Maximum droplet diameter
e	Natural constant (2.718…)
E	Young modulus
E_a	Activation energy
E_t	Tensile modulus
f	Mixture fraction
f'	Mixture fraction variance
F	Force
f_{inert}	Inert mass fraction of the motor
G	Mass flux
G_{dyn}	Dynamic shear modulus
G'	Elastic/storage modulus
G''	Viscous/loss modulus
h	Enthalpy
ΔH_{evap}	Latent heat of evaporation
I_{sp}	Specific impulse
j_g	Superficial velocity of the gas in multiphase flow
j_l	Superficial velocity of the total liquid (Eq. 4–31)
k	Turbulent kinetic energy
K	Reaction rate
L	Length
L_0	Gauge length of the test specimen
ΔL_0	Increase of the specimen length between the gauge marks
$L_{\dot{m}}$	Losses of the liquid mass flow
L/D	Ratio of the length of the post combustion chamber and its diameter
m	Mass
m_{pay}	Payload mass
$\dot{m}$	Mass flow
M_w	Molecular weight
N	Number of ports of the solid fuel grain
O/F	Mixture ratio (oxygen to fuel ratio)
P	Pressure
P_c	Pressure in the combustion chamber
Pr	Prandtl number
R'	Universal gas constant

Re	Reynolds number
S	Source term
Sc	Schmidt number
Sc_T	Schmidt number turbulent
T	Temperature
$T_{melting}$	Melting point temperature
T_{motor}	Thrust
u_i	i^{th} component of the gas velocity vector
V	Volume
ΔV	Velocities difference determined by the mission
$We_{d_{vm}}$	Weber number
y	Dimensionless function of x (Eq. 4–20, 4–21)
Y	Species mass fraction
$Y+$	Non-dimensional distance from wall

Subscripts

cc	Combustion chamber
e	Exit area of the nozzle
f	Fluid properties
fin	Final
$fuel$	Fuel properties
g	Gas phase in multiphase flow
$init$	Initial
l	Liquid phase in multiphase flow
m	Hydrogen number (Eq. 4–18)
n	Carbon number
$nozzle$	Nozzle
ox	Oxidizer properties
p	Particle properties
$port$	Fuel grain port
$prop$	Propellant properties
t	Throat area of the nozzle

1 INTRODUCTION

> "The detailed physics of what goes on inside a hybrid rocket – combustion that is just as intense as that of any other kind of rocket – remain something of a mystery" Brian J. Cantwell [1].

Hybrid rocket motors had been first tested back in 1930s, but only recently have regained interest as a research topic due to the increasing demand for safer and more economical propulsion systems. Such systems combine advantages of both liquid and solid propulsion systems. As well as a liquid engine a hybrid motor would possess such characteristics as

- the possibility of throttling and restart; as long as one of the components is liquid its supply to the combustion chamber can be regulated or cut off;
- reduced fire and explosion risk due to the separation of the components;
- reduced mechanical complexity due to the only one component present in the liquid state that requires pressurant system, or turbo pump system;
- the characteristics above lead to the cost reduction.

Unfortunately, there is always another side of the coin, and despite of the fantastic characteristics listed above hybrid motors are featured some disadvantages. The main factor that is keeping HRMs away from a leading position among thermochemical propulsion systems is low regression rate of the solid fuel. Several regression rate enhancement technics have been being tested over the last decades, such as

- addition of metal powders to increase the radiative heat flux to the surface of the solid fuel [2]; this leads to higher viscosity and thus makes the manufacturing process more difficult.
- multiple ports in the fuel grain to increase the burning surface, but such complex geometry eliminates the desired simplicity.

Recently, paraffin has been proposed as a hybrid rocket fuel. Labscale investigations by Karabeyoglu, have shown 3-4 times higher regression rate compared to conventional fuels. The reason for this improvement is the different mechanisms taking place inside the combustion chamber. Karabeyoglu has extensively studied the paraffin-based hybrid fuels and developed a liquid layer theory [3], [4], [5].

The theory suggests that paraffin-based fuels form a liquid layer that becomes unstable due to the shearing flow of the oxidizer, then the roll waves formed and the liquid fuel droplets are entrained into the main stream of the oxidizer. This mechanism of spray formation increases fuel surface area (fuel grain surface + droplets surface), with which the oxidizer can react. Unfortunately, fluid dynamics are higher than the

chemical kinetics. As a result liquid fuel droplets can be blown through the combustion chamber remaining non evaporated and not reacted, which means lost with no contribution to the combustion process. Additionally, paraffin is a brittle material, so the more it's heated the more it loses its strength and thus the more melted fuel losses can be expected. To prevent that, strengthening additives were studied [6], [7]. This is a challenging task of finding a strengthening additive to paraffin that would be a good compromise between low enough viscosity for the entrainment process to occur and mechanical properties of the paraffin-based fuel.

Since the processes and interactions of properties in HRM are not well understood, the current research work attempts to resolve several of the key unknowns affecting hybrid rocket design in two phases.

First, an experimental investigation of paraffin-based fuel properties was carried out. Several formulations of paraffin blends strengthened by thermoplastic polymers were studied to determine the blend formulations effects on their melting point temperature, rheological properties and mechanical properties.

Second, a CFD model was developed for simulating internal processes of combustion in a hybrid rocket motor. The model considers geometry of the combustion chamber of a lab-scale facility at SPLab. The model included such phenomena of hybrid rocket combustion as

- gaseous non-premixed turbulent combustion;
- multiphase reacting flow (liquid paraffin droplets).

Special attention was given to chemical kinetics modeling and size droplet distributions of the liquid fuel. Mass flows were set as boundary conditions satisfying different values of oxidizer-to-fuel ratio.

So, once the liquid particles are entrained into the flow their function is to fully evaporate and burn, which is not necessarily happening in reality. Therefore sensitivity studies of how oxidizer-to-fuel ratio and liquid mass flow affect the evaporation and flame shape were performed. O/F values were varying from a lower to a higher value to simulate operating condition of a HRM. Two fractions of liquid fuel mass flow were considered – 30% and 60% – based on the experimental investigation of the rheological properties of paraffin-based fuels that showed an increase of viscosity when a strengthening material is added, which should lead to a reduction of entrained liquid phase. The cases with these two liquid fuel fractions were confronted with the baseline – a gaseous combustion case, as if the liquid film immediately and fully evaporated.

An important characteristic of any rocket engine/motor is characteristic velocity c^*. It is commonly used for combustion chamber performance evaluation and comparison between different fuel/oxidizer couples. The quantity c^* is considered a parameter of merit for the engine combustion chamber: a large value indicates a good efficiency of the thermochemical energy conversion in the combustion chamber [8].

NASA “Chemical Equilibrium with Applications” software is the most common tool for an estimation of a rocket engine/motor’s characteristics. But it has to be noted that is has been developed with certain assumptions that do not align with the hybrid rocket combustion. For instance, such assumptions as:

- Complete combustion;
- Homogeneous mixing;

Homogeneous mixing assumption is not satisfied by the definition of a diffusion-limited combustion. The efficiency of combustion in a hybrid motor configuration is a matter of study for this research work. In order to evaluate the effects of these assumptions characteristic velocity c^* was calculated using CFD modeling results.

Plan of presentation

This research thesis is presented in the following order:

- Chapter 2: the state of the art of hybrid propulsion is given with an emphasis on the novel paraffin-based fuels. A subchapter is dedicated to the state of the art of the numerical simulations.

- Chapter 3: the chapter is dedicated to characterization of novel paraffin-based fuels strengthened by thermoplastic polymers through experimental investigation.

- Chapter 4: the development of the numerical model of spray combustion for a hybrid rocket motor configuration is described.

- Chapter 5: the detailed description of settings for the numerical simulations is given; the results on spray combustion simulations and characteristic velocity evaluation are discussed.

- Chapter 6: conclusions on experimental and computational investigations as well as some suggestions for future work and developments.

2 STATE OF THE ART OF HYBRID ROCKET PROPULSION

In this chapter an overview of the development of hybrid propulsion systems is given. Fundamentals of hybrid rocket combustion are described, with an emphasis on the physical phenomena involved in paraffin-based fuels combustion. A section is dedicated to CFD modeling of hybrid rocket flowfields, conventional as well as novel paraffin-based fuels.

2.1 Fundamentals of Hybrid Rocket Propulsion

2.1.1 Introduction. Development of HRM

Hybrid rocket motors are called hybrid due to the combination of solid and liquid state of the propellant components. A classical hybrid rocket motor is when the fuel is solid and oxidizer is liquid.

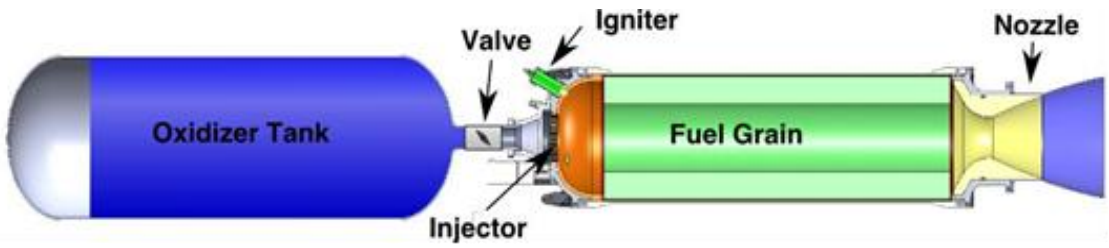

Figure 2–1 A classical hybrid rocket motor - schematic

Hybrid rockets have been the subject of research for many decades using an array of compounds for fuels ranging from wood, to rubber. The first attempts at hybrid rocket propulsion were made by soviet researches in the early 1933 who used a coagulated form of gasoline along with liquefied oxygen. Later, in 1937, attempts in Germany used fuel/oxidizer combination of coal with N2O or graphite with liquid oxygen [9], [10]. In 1953, the Pacific Rocket Society used wood from Douglas fir trees as the fuel for a series of hybrid rockets [10]. Later tests by General Electric used hydrogen peroxide and polyethylene [11]. After these initial attempts, the fuel of choice was typically gradually settled on the HTPB+N2O combination that was eventually used in what is perhaps the best-known application of a hybrid rocket motor, SpaceShipOne, produced by Mojave Scaled Composites [12], which won the Ansari X-prize in 2004. SpaceShipOne was further developed into SpaceShipTwo, a suborbital spaceplane designed for space tourism, and owned by Virgin Galactic [13] (see Figure 2–2).

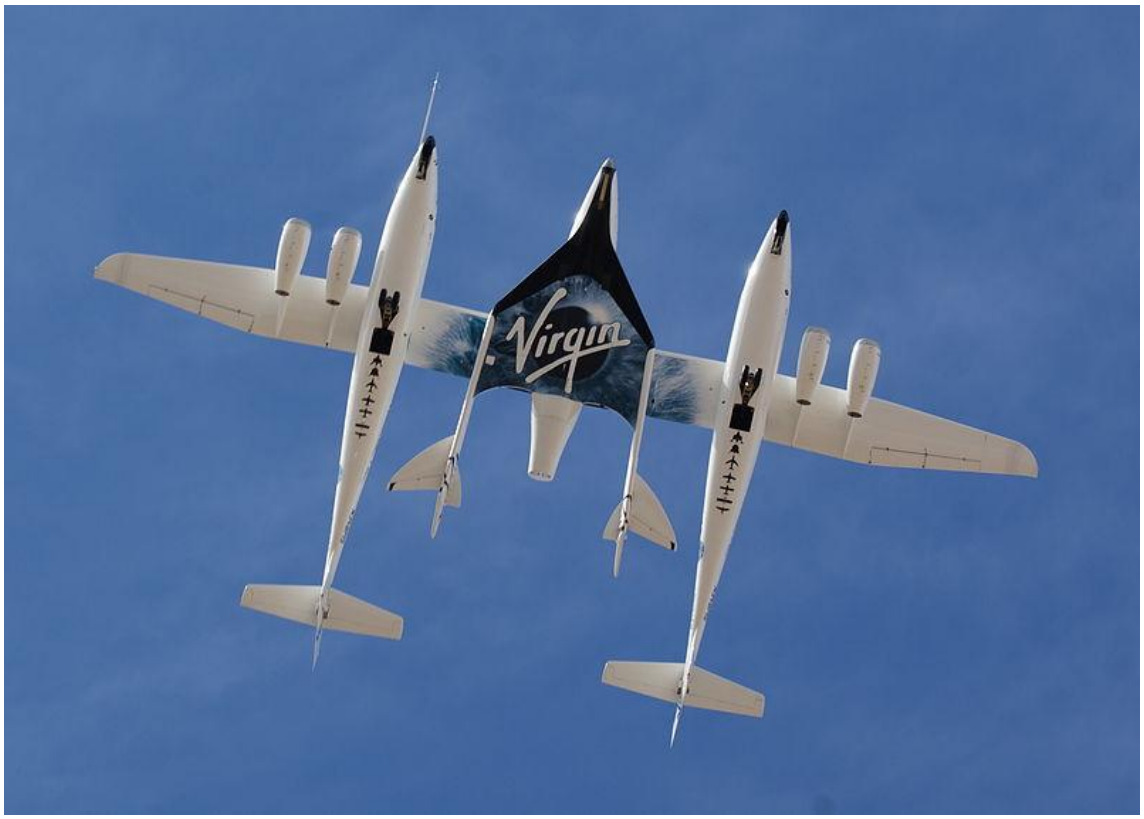

Figure 2–2 SpaceShipTwo (in the middle) carried by the mother ship carrier White Knight Two

Marxman's diffusion-limited combustion

For typical hybrid rocket motor configurations, the gaseous phase flows along the surface of the solid phase forming a turbulent boundary layer. Once initiated, the reactions release heat which diffuses or radiates back to the solid surface and thereby vaporizes more fuel which is in turn diffused back into the reaction zone. Typically the reaction rates of the kinetics in the reaction zone are much faster than the relatively slow diffusion process which provides the fuel to the flame, thus the flame is said to be diffusion-limited that increasing the speed of the reaction kinetics will have no measurable impact on the combustion process but increasing the rate of fuel transport will. In other words, total mass flux $\left(G_{ox} + G_{fuel}\right)$ is the main parameter that determines the regression rate of the fuel.

The most widely used model for hybrid rocket combustion, Marxman's diffusion-limited model [14], [15]. This model operates on the diffusion-limited assumption and derives, based on turbulent boundary layer theory (see Figure 2–3), a balance between the heat released by the diffusion rate of heat to the fuel surface with the fuel regression rate of the fuel and the amount of heat flux required to sustain such. These balance fluxes evolve in the streamwise direction to conserve mass, momentum, and energy to predict the overall performance of the motor. While this diffusion-limited approach is a helpful analysis tool, it cannot account for phenomena like thermal

radiation and fuel melting/atomization that can increase the fuel regression rate that has limited the use hybrid rockets in the past due to inadequate performance.

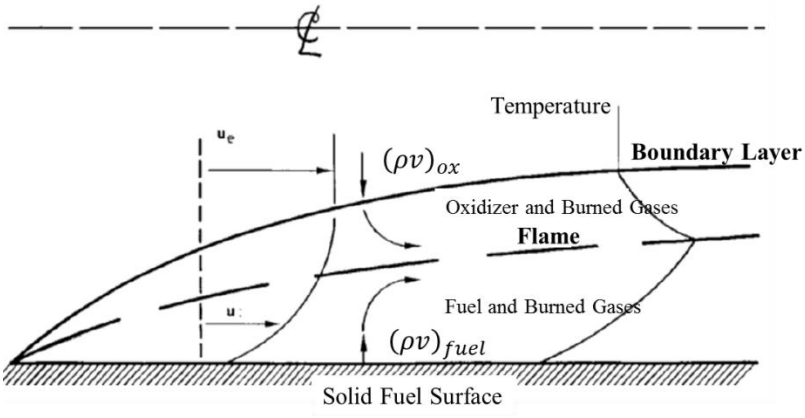

Figure 2–3 Diffusion-limited combustion - schematic

Thermal radiation effects

Thermal radiation from the flame to the solid surface cannot be accounted for in the traditional Marxman model because it transports heat independent from turbulent diffusion. While the mass vaporized by this additional heat must still be transported by turbulent diffusion to the flame which may push the flame farther away from the solid surface than without the radiation effect. The effect of thermal radiation is a very complex process that involves complex between the electromagnetic radiation emitted by the high-temperature gas molecules, and the absorption, scattering, and reradiation of this radiation energy by the surrounding gas molecules, solid surfaces, and entrained soot particles and fuel droplets. Marxman and co–workers corrected the original purely convective model by adding radiative heat transfer [16].

For small geometries with walls that are substantially colder than the gas temperature the chances for significant radiation effects are diminished and can often be neglected in favor of adding additional complexity to other, more important physical phenomena.

Fuel entrainment and Evaporation

Finally, the Marxman model does not account for the transport and evaporation of entrained fuel droplets. To account for this effect, the interaction between the droplets and turbulent eddies must be accounted for to transport them towards or away from the fuel grain a process which is highly dependent on the inertia of the particle due to its size and the characteristics of the turbulent eddies. Additionally, the evaporation rate of the droplet will depend on the rate at which heat can be transported to the

droplet, usually by diffusion from the surrounding gas, but in some situations by radiation as well. These evaporating fuel particles will affect distribution of the oxidizer-to-fuel ratio throughout the engine and thus affect the location of the flame front and the rates of diffusion of the various chemical species. For more detail on entrainment process see Chapter 2.1.3 “Regression Rate Enhancement” and Chapter 2.1.4 “Paraffin-based Fuels”.

Pressure effect

While the processes in the Marxman model are strictly convective and diffusive in nature, which implies only a secondary dependence on the operating pressure, it has been reported in the literature that the regression rate can be affected pressure independently from the oxidizer flux although the effect is only seen in some pressure ranges and within certain ranges of oxidizer flux, [17], [18], [19], and then the effect seems to be tied to the type of fuel used. To add further confusion, the effect of increased pressure in some cases leads to increased regression rate where in other cases the regression rate decreases. It has been hypothesized that these departures from the diffusion-limited trends may be the result of heterogeneous reactions at the surface of the fuel grain which may be either exo- or endothermic and which would therefore cause a deviation from the diffusion-only model while also being pressure dependent.

2.1.2 HRM characteristics

Hybrid rockets offer a number of advantages over either liquid- or solid-only rocket motors as they recover some of the best properties of each. They also suffer from some disadvantages which have historically limited their application to small niches.

Since hybrid rocket motors do not premix their fuel and oxidizer, they can be safely transported and stored for extended periods without risk of explosion. This lack of premixing also relaxes the constraints on manufacturing defects which in turn leads to increased robustness and decreased manufacturing costs. Compared to liquid rocket systems, hybrid rockets require only the oxidizer to be pumped which eliminates failure modes and further increases reliability. Compared to solid rockets, hybrid rockets feature much greater controllability and can be throttled, shut down, and restarted by simply changing the oxidizer flow rate.

Hybrid rockets further enjoy many advantages when it comes to design flexibility. Hybrid rockets have been designed to use an extremely wide range of fuels from wood, to coal, to rubber. The solid fuel grain can be tailored to various mission requirements by adding different compounds to the fuel grain such as metals to increase energy content. Further, the controllability and reliability of hybrid rockets make them a natural choice for upper stages but their low cost make them suitable for an array of different missions like orbit maintenance maneuvers. Since hybrid rocket motors

typically produce no hydrogen chloride or aluminum oxide, hybrid rockets can be a good choice for missions where environmental concerns are a factor.

Hybrid rockets exhibit several disadvantages that can limit their suitability to various missions. First, hybrid rockets typically rely on turbulent boundary layers to mix the oxidizer with the fuel as it vaporizes from the grain. This turbulent mixing may not be complete by the end of the fuel grain, this unmixed and therefore unreacted fuel and oxidizer can represent a significant loss in combustion efficiency and performance. To overcome this problem, hybrid rockets often feature mixing chambers downstream of the fuel grain to allow for the mixing and combustion to finish before reaching the nozzle. However this extra space requirement is undesirable for the rest of the rocket's systems by increasing the rockets volume and mass.

During hybrid rocket operation, the oxidizer mass flow is typically held constant while the solid fuel grain burns. As the surface of the fuel grain regresses away from the oxidizer, it typically gains surface area leading to a decrease in the amount of oxidizer flow per unit surface area of fuel grain which in turn affects the fuel's regression rate. This effect is somewhat self-compensating but still affects the global oxygen to fuel ratio inside motor which means that the equivalence ratio that gives the optimal specific impulse cannot be maintained. Fortunately the specific impulse is not strongly sensitive to equivalence ratio and the rocket motor can be designed so that the oxygen-to-fuel ratio is centered around the optimal point with the lowest point at ignition and the highest point just before burnout.

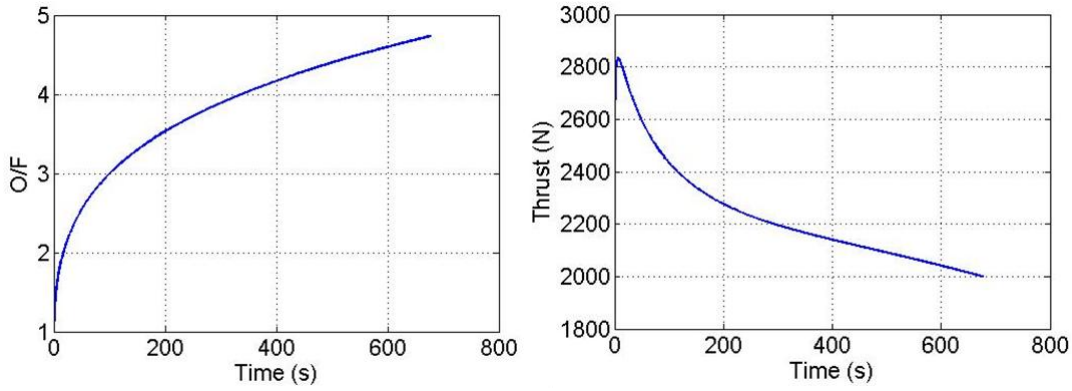

Figure 2–4 Illustration of O/F shift during burn time. Thrust decrease is illustrated as well

Perhaps the primary disadvantage which has most limited the use of hybrid rocket motors is the low regression rate. Hybrid rocket fuels are typically polymeric compounds like HTPB which, for common applications, has a regression rate an order of magnitude or more below their solid propellant counterparts. To solve this problem, hybrid rockets often use multiple oxidizer ports and have fuel grains with specialized geometries with large wetted areas. Such grains are also undesirable not only because they increase the complexity of the manufacturing process and are less structurally

sound than simpler geometries, but also because they further increase the volume of the fuel and the mass of the pressure vessel. The limited regression rates of conventional hybrid rocket motors has led to several methods that attempt to alleviate the problem.

2.1.3 Regression Rate Enhancement

Since the majority of hybrid rocket motors operate in a diffusion limited regime and suffer from the problems associated with low regression rate, several attempts to increase the regression rate have focused on using fluid dynamics to manipulate the turbulent boundary layer to increase the heat flux to the wall thereby increasing the local regression rate. To achieve increase heat flux at constant oxidizer flux, swirling flow has been well researched by several researchers: Knuth et al. [20], [21], Yuasa et al. [22], Lee et al. [23], Rice et al. [24], Haag et al. [25], and Caravella et al. [26]. Haag considered many of various geometrical configurations [27]. Latest investigations have been carried out in Japan (JAXA) including visualization of swirling flames [28].

These studies used several different types of swirling configurations with various nozzle geometries and showed clearly enhanced regression rates up to 6 times those seen in classical hybrids at the same, unswirling, oxidizer flux. To maintain the swirl number inside the motor throughout the burning process most of these geometries tended toward a low aspect ratio geometry making them unsuitable for launch vehicle stages where aerodynamics is a concern.

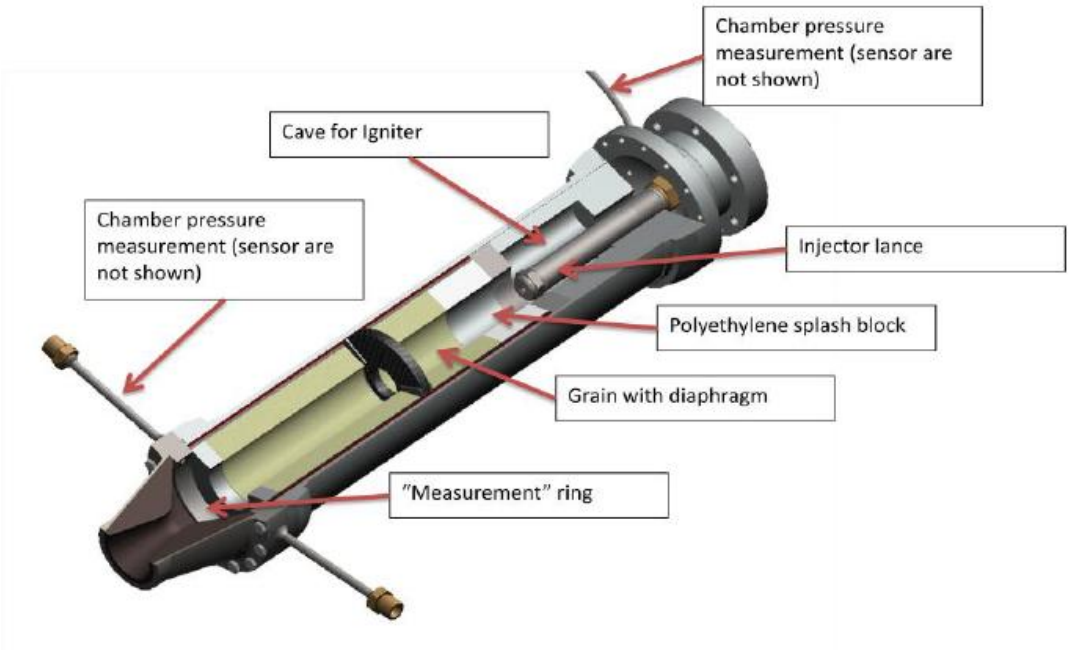

Figure 2–5 Configuration of the testing facility of diaphragms [29]

Axial-flow configurations using specialized oxidizer injection techniques have also been attempted to induce recirculation, boundary layer restart, and general boundary layer thinning in an effort to increase the heat flux to the fuel grain. One such attempt used experiments and CFD models to evaluate various diaphragm restrictor geometries in order to find an optimal configuration. These restrictors were placed at various axial locations along the length of the motor and had varying shapes cut through them to provide the restriction (see Figure 2–5). Several of these geometries showed increased performance due to enhanced mixing in the rocket compared to a restrictor-free baseline [29].

Fuel additives have also been an active area of research for increasing rocket performance. The addition of metals, aluminum in particular has been used as a way to increase the energy of the combustion reaction with the added benefit of diminishing combustion instabilities due to the presence of aluminum particles which damp acoustic waves and thicken the flame front making it less susceptible to acoustic instabilities. LiH has also been the subject of study which shows significantly enhance regression to a butyl-based solid fuel with higher levels of LiH addition [Smoot and Price]. An extensive research on how various metallic additives influence the regression rate of hybrid rocket fuels is carried out by Space Propulsion Laboratory (SPLab) at Politecnico di Milano [30], [31], [2], [32].

2.1.4 Paraffin-based Fuels

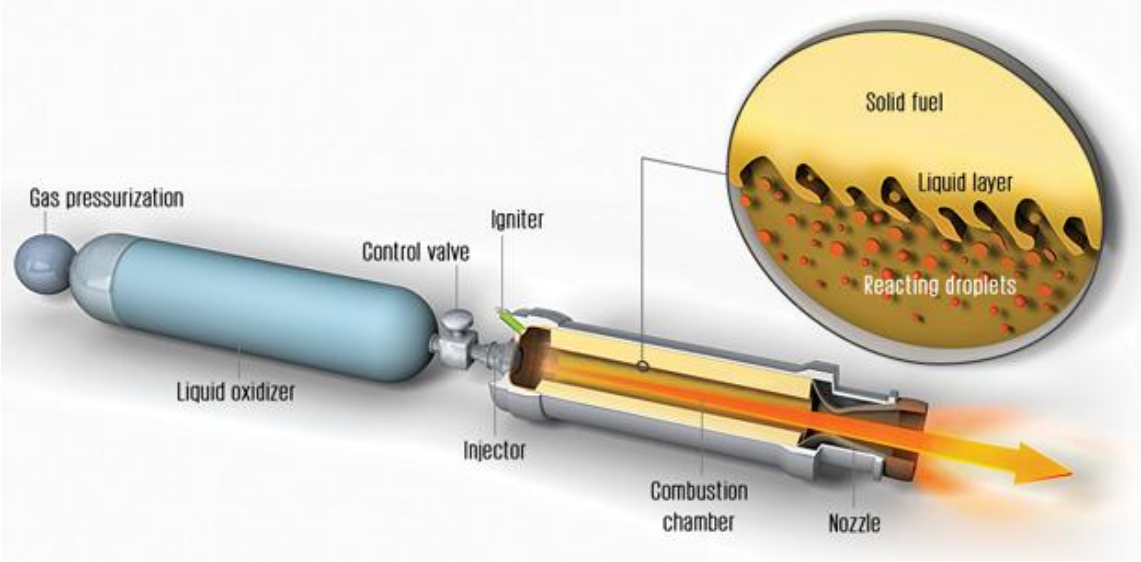

Figure 2–6 Spray formation in paraffin-based hybrid rocket motors. Illustration: Emily Cooper [1]

A more recent advance in enhanced regression rate research has come from the work of Karabeyoglu who, in the process of investigating cryogenically frozen fuels found that the regression rate of some of these fuels was 3-4 times greater than that predicted by a diffusion-limited model for conventional HTPB (see Figure 2–7) [3], [5]. The reason for this extra mass flux was hypothesized to come from the fuel melting to form a liquid film on the surface of the grain. This film then vaporizes fuel directly but also becomes entrained in the high-speed oxidizer stream where it breaks up into a fine spray of fuel droplets (see Figure 2–6).

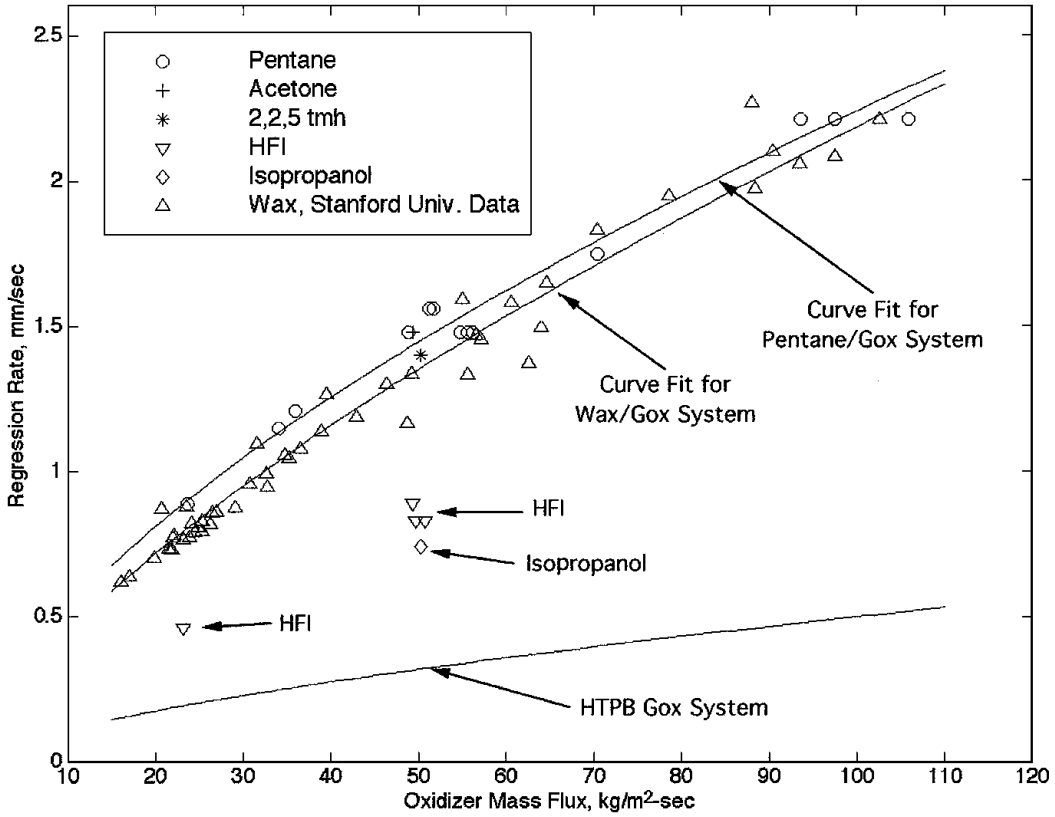

Figure 2–7 Regression rate of paraffin-based fuels increased by 3-4 times compared to the conventional HTPB-fuels

The entrainment of the melted fuel occurs in several stages as the liquid film first starts to form unstable roll waves as it is sheared along by the oxidizer (see Figure 2–8) [33]. As parts of the roll wave begin to break off in sheets and ligands, the viscous and surface tension forces that keep the larger sheets together is less than the shear and pressure forces tearing them apart and the droplets are atomized into smaller and smaller sizes which evaporate, burn, and move within the oxidizer stream. If the droplets are small enough they will finish burning before they reach the end of the motor and the increased regression rate will translate directly to increased thrust, however if the droplets are too large, if the motor is too short, or if the evaporation and burning rates are too slow, the droplets will leave the motor without burning and will represent an inefficiency that may be as detrimental to performance as low regression

rate would have been. The interaction between these various mechanisms is very complex and not accounted for by in traditional models.

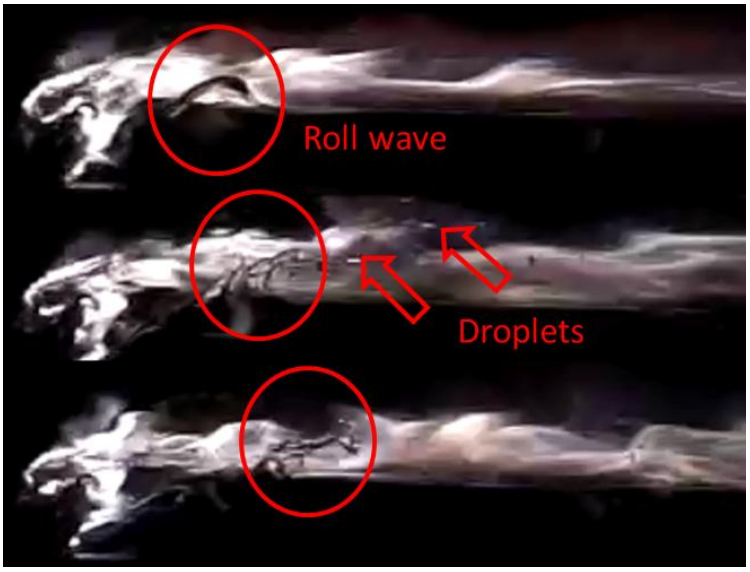

Figure 2–8 Visualization of a roll wave in the liquid layer at atmospheric pressure. Droplets can clearly be seen separating from the wave and entraining in the flow [33]

As can be seen, due to the entrainment process the number of phenomena involved in the combustion of paraffin is higher comparing to the conventional HTPB fuel. The phenomena involved in combustion of those two kinds of fuels are summarized in Table 2–1. The four main physical properties are common for both kind of fuels, while combustion of paraffin will include three more processes.

The ability to form a liquid film during combustion requires the fuel's properties to have a low melting point while also having enough strength and toughness to be able to withstand the stresses and vibrations of the combustion process. Paraffin has been found to have a sufficiently low melting point but was too brittle to be considered suitable. Fuel strengthening additives (polymers), if carefully chosen, may offer a means to improve the paraffin's suitability by increasing its strength, ductility, etc. while maintaining its ability to melt under the proper conditions. Care must also be taken to ensure that the additives effect on the viscosity of the liquefied fuel doesn't prevent the fuel from atomizing into a fine enough spray to evaporate and burn quickly before leaving the motor. Experimental testing of the mechanical properties of various fuel mixtures represents an important part of this thesis in Chapter 3 "Paraffin-based Fuels: a Way to Increase Regression Rate".

Table 2–1 Main physical phenomena involved in combustion of HTPB (4 processes) and Paraffin (7 processes)

HTPB	Paraffin-based fuel
1 Oxidizer atomization and vaporization (for liquid state)	
2 Radiation	
3 Fuel surface pyrolysis	
4 Gas-phase combustion (non-premixed)	
	5 Melting / Liquid layer formation
	6 Entrainment / Droplets formation
	7 Spray combustion

2.2 CFD Modeling of Hybrid Rocket Motors

2.2.1 CFD of Conventional HTPB HRM

Modeling of conventional hybrid rocket motors is a much simpler task than modeling paraffin-based systems that melt and atomize yet are still quite complex as it was described above (see Table 2–1). CFD models of conventional HTPB hybrids require a method for specifying the local pyrolysis rate of the solid fuel under the presence of the oxidizer and flame, either by coupling the pyrolysis rate to the local heat flux conditions or by simply imposing a given regression rate of the fuel from an experimental analysis. Either way, the reaction mechanism whereby the fuel is oxidized must interact with the turbulent mixing model used by the CFD flow solver. Several examples of these models exist in the literature and can serve as starting points from which to develop CFD modeling strategy that can account for the more complex physics of hybrid rockets where melting and entrainment occur.

High level of achievement in HTPB-based HRM modeling has been reached, such as prediction of regression rate and its validation by experimental investigations.

For instance, G. Gariani implemented a model using open source code OpenFOAM [34], [35]. The model considers two computational domains – solid and gaseous with a coupling between them. The regression rate is calculated according to a specific Arrhenius law for the HTPB pyrolysis [36] based on the solid fuel temperature coming from the flame through the radiative flux. The numerical simulations show good agreement with experimental data available from different sources in literature (see Figure 2–9).

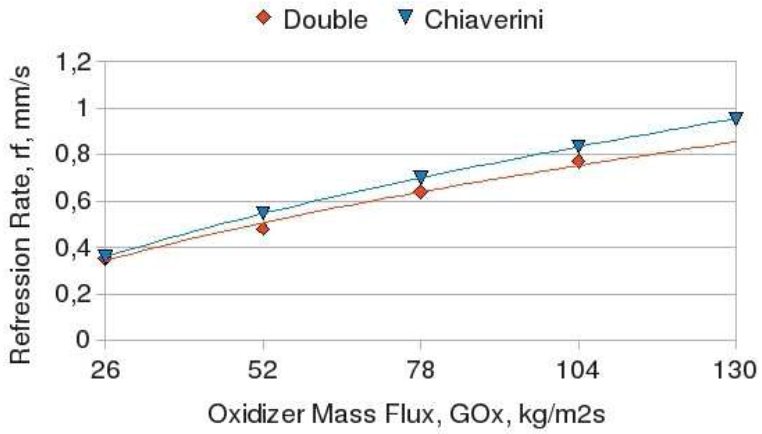

Figure 2–9 Comparison of numerical simulation results with experimental data [35]

Similar simulation work has been done by Coronetti and Sirignano [37]. A semi-empirical law of the fuel regression rate proposed by researchers at Politecnico di Milano [38] was used for several sensitivity studies such as effect of pressure, oxidizer mass flow, and oxidizer inlet temperature. The study showed good agreement with the experimental data.

Many other research groups have succeeded in instantaneous regression rate simulations of HTPB based hybrid motors [39], [40], [41], [42], and there are some groups that have implemented some extra features such as modeling of liquid oxidizer instead of gaseous [43], [44]; swirling configuration of hybrid motors [20].

2.2.2 Paraffin-based

Given the success of CFD modeling of conventional hybrid rocket motors, the extension of these models to include paraffin-based and other melting fuels seems natural. The added complexity of a seemingly minor extension is in fact enormous in a CFD framework. The additional complexity comes not only from the number of additional physical phenomena (see Table 2–1) that must be accounted for but also the degree of interaction between these phenomena as well as the difficulty inherent in accounting for multiple phases, with multiple relevant time- and length-scales within a single finite-volume framework. The additional complexity makes a comprehensive CFD model to be difficult to develop.

CFD models have been used in the past to simulate the dispersion of burning fuel droplets while other CFD models have been developed to account for the interaction between a high-speed gaseous freestream a low-speed liquid free surface, however describing the complete transition agitate free-surface to dispersed liquid droplets is still well beyond the capabilities of commercial CFD solvers and cannot be handled accurately in a RANS framework which would typically be used for a design application. Given these restrictions, the state of the art in modeling melting/entraining

fuel combustion is limited to lower-order mostly analytical models which treat transport phenomena in a very simplified manner.

Lestrade et al. [45], [46] produced a series of models that described various combinations of the melting, vaporization, entrainment, liquid film flow, and combustion processes, making broad use of simplifying assumptions to make the problems tractable in 1- and 2- dimensions. The first of these models began with a 1D model of the streamwise evolution of the gas-phase boundary layer using 1D momentum conservation along with analytical expressions for the entrainment rate, interphase heat exchange, and boundary layer profile shape, while neglecting combustion and droplet dispersion. The other models that came from this work represent a valuable tool for describing the interactions between some of the relevant phenomena and set the stage for the current work which can account for many more of these transport phenomena and the interactions between them while making far fewer assumptions leading to increased relevance in the conceptual design cycle.

Bellomo et al. [29] attempted to simulate a full hybrid motor, subsonic flow as well as supersonic expansion through the nozzle, using Ansys CFX 12 software. They simulated gaseous only combustion, not taking into account any of melting, entrainment, evaporation phenomenon. Although they showed very good agreement of the characteristic velocity obtained from simulations with the experimental ones. The error is within 5.5%.

3 PARAFFIN-BASED FUELS: A WAY TO INCREASE REGRESSION RATE

As previously explained in the Chapter 2.1 “Fundamentals of Hybrid Rocket Propulsion” the combination of ballistic and mechanical properties is a key issue for novel paraffin-based fuels. This chapter is dedicated to experimental investigation of characteristics of paraffin-based fuels. This chapter is trying to investigate how strengthening materials influence thermal, rheological and mechanical properties of paraffin-based fuels.

3.1 Tested materials

3.1.1 Paraffin Wax

Paraffin waxes are a mixture of hydrocarbons, mainly normal alkanes. Alkanes were found forming melting layers on the burning surface of a solid fuel grain during combustion which causes the entrainment effect.

Paraffin-waxes are defined as a family of saturated hydrocarbons with a crystalline structure without odor or taste. Paraffin-waxes consist of mixtures of mainly normal alkanes. The general formula of paraffin is defined as:

$$C_n H_{2n+2} \qquad 3–1$$

Paraffins having between 5 and 15 carbon atoms are liquids at room temperature, and those with more carbon atoms are waxy solids (e.g. well-known paraffin octadecane, $C_{18}H_{38}$).

Paraffin can be classified according to purity, i.e. refinement, melting point, etc. Considering the cost, however, only technical grade paraffin-wax, a by-product of oil refining, may be used as a fuel for a hybrid rocket engine.

In the scope of this work a paraffin supplied by GellyWax company with the melting point temperature around 55-60°C was used as a main ingredient. The melting point temperature suggests that the paraffin-wax’s chemical formula is close to $C_{28}H_{58}$.

3.1.2 Thermoplastic Polymers as Strengthening Materials

As it was said before a paraffin-wax itself does not have sufficiently good mechanical properties (see Table 3–1), as good as, for example, would allow a solid fuel grain to remain in solid state under high temperature environment in the combustion chamber. Thereby the need of finding a kind of strengthening additive arises.

Table 3–1 Averaged values of hardness of a typical paraffin-wax and polyethylene

	Paraffin-Wax	**Polyethylene**
Hardness* (needle penetration ASTM D1321	9-20 [47]	2-4 [48]
Melting Point [49], ° F (°C)	134 (56)	216 (102)

** smaller values denote higher hardness*

Based on previous research works [6] and looking for a suitable match, two thermoplastic polymers (TPP) were chosen [50]:

- Polystyrene-block-poly(ethylene-ran-butylene)-block-polystyrene-graft-maleic anhydride (SEBS) and
- Polystyrene-block-polyisoprene-block-polystyrene (SIS).

SEBS and SIS are low molecular weight polymers and are expected to increase hardness, tensile strength and flexibility of paraffin-wax as well as polyethylene does [49].

One of the most important properties of these two TPP is their good compatibility with paraffin-wax. A homogeneous mixture is expected due to the presence of ethylene-butylene and isoprene blocks in their chemical formulas, which are similar to paraffin structure. The blend of TPP and paraffin forms a semi-crystalline thermoplastic structure (see Figure 3–1) and ensures low manufacturing costs, homogeneous fuels and possibility to use this kind of formulations in higher-scale tests.

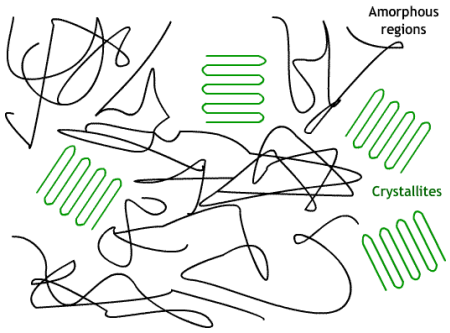

Figure 3–1 Schematic illustration of TPP-paraffin structure

SEBS

Polystyrene-block-poly(ethylene-ran-butylene)-block-polystyrene-graft-maleic anhydride (SEBS) provided by Sigma Aldrich contains 30% of styrene and 2% of maleic anhydride (MA). The chemical structure is shown on the Figure below.

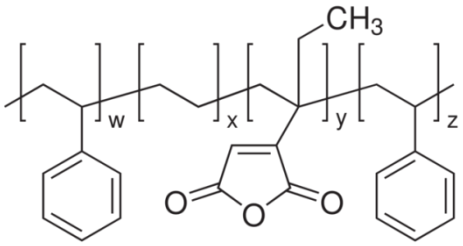

Figure 3–2 The chemical formula of SEBS

SIS

Polystyrene-block-polyisoprene-block-polystyrene (SIS) provided by Sigma Aldrich contains 17% of styrene. The molecular weight is M_n = 1900 g/mol [50].

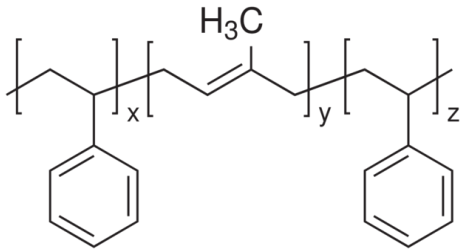

Figure 3–3 The chemical formula of SIS

Carbon black

Carbon black powder is used in paraffin-based formulations in order to enhance the possible radiative heat transfer between flame zone and the regression surface [51], [5], [52] and also to concentrate the radiation absorption in the thin layer under the regression surface.

3.1.3 Manufacturing Procedure

Tested fuels were manufactured at SPLab, Polimi. Manufacturing was performed in a chemical laboratory with dedicated facilities and controlled environment.

Operating steps:

1. Required amounts of paraffin-wax, TPP and carbon are placed in a Pyrex beaker (after check of static electric charge absence).
2. Pyrex beaker is placed in a heated oil bath with temperature of 350°C till complete melting of paraffin-wax and TPP.
3. Compound is mixed for 40 minutes by an impeller inserted in the beaker.
4. Compound is gradually poured into molds. Operation is performed in multiple steps in order to avoid possible imperfections in the solid fuel grain.
5. After complete filling, the molds are left at ambient temperature for complete cooling of the material.

3.1.4 Tested fuel formulations

Tested paraffin-based fuels were divided into two groups containing two different thermoplastic polymers. Each group consisted formulations with different content of TPP. The fuel blends were investigated and compared to the baseline - pure solid wax (SW). The fuel formulations are listed in the Table 3–2:

Table 3–2 Fuel formulations manufactured and investigated

Fuel Nomenclature	Composition (mass fractions, %)
SEBS05	SEBS 5% – SW 94% – CB 1%
SEBS10	SEBS 10% – SW 89% – CB 1%
SEBS15	SEBS 15% – SW 84% – CB 1%
SEBS20	SEBS 20% – SW 74% – CB 1%
SEBS30	SEBS 30% – SW 69% – CB 1%
SIS10	SIS 10% – SW 89% – CB 1%
SIS30	SIS 30% – SW 69% – CB 1%

3.2 Solid Fuels characterization

Three kinds of experimental investigations were conducted in order to study the thermal, rheological and mechanical properties of paraffin-wax based blends doped with

thermoplastic polymers in order to evaluate a formulation which best meets the requirements to be used as a solid fuel for hybrid rocket engines.

3.2.1 Thermal Characterization

Differential Scanning Calorimeters (DSC) measure temperatures and heat fluxes associated with thermal transitions in a material. Common usage includes investigation, selection, comparison and end-use performance evaluation of materials in research, quality control and production applications. Properties measured by TA Instruments DSC techniques include glass transitions, "cold" crystallization, phase changes, melting, crystallization, product stability, cure kinetics, and oxidative stability.

In a DSC the difference in heat flow to the sample and a reference at the same temperature, is recorded as a function of temperature. The reference is an inert material such as alumina, or just an empty aluminum pan. The temperature of both the sample and reference are increased at a constant rate.

The calorimeter consists of a sample holder and a reference holder as shown in the Figure 3–4. Both are constructed to allow high temperature operation. Under each holder there is a resistance heater and a temperature sensor. Currents are applied to the two heaters to increase the temperature at the selected rate. The difference in the power between the two holders is necessary to maintain the holders at the same temperature.

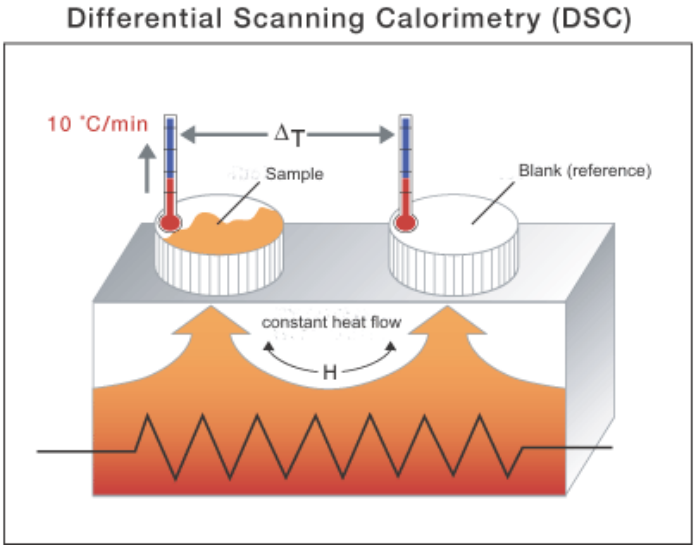

Figure 3–4 Differential scanning calorimetry (DSC)

Thermal properties such as melting temperatures, latent heats of melting of pure paraffin-wax, pure thermoplastic polymers (SEBS and SIS) and fuel blends were measured by the differential scanning calorimetry (DSC) technique. DSC was

performed by a DSC 2010 Differential Scanning Calorimeter, TA Instruments in heating and cooling cycle. Samples with a mass of ~10 mg were sealed in an aluminum pan; an empty pan was used as reference. The analyses were performed in the temperature range of –50 ÷ +150(300) °C with a heating rate of 10 °C/min and under a constant stream of nitrogen.

Test conditions

1) Sample weight: ~10mg;
2) Temperature range: –50 ÷ +150(300) °C;
3) Temperature ramp: 10°C/min.

Typical result curves of a pure TPP (SEBS), a pure paraffin-wax and a blend (SEBS30) are shown on the Figure 3–5. It can be noticed that the composites have melting point temperatures $T_{melting}$ close to paraffin-wax, while the melting of a pure TPP (SEBS or SIS) occurs when the temperature goes higher than +300°C.

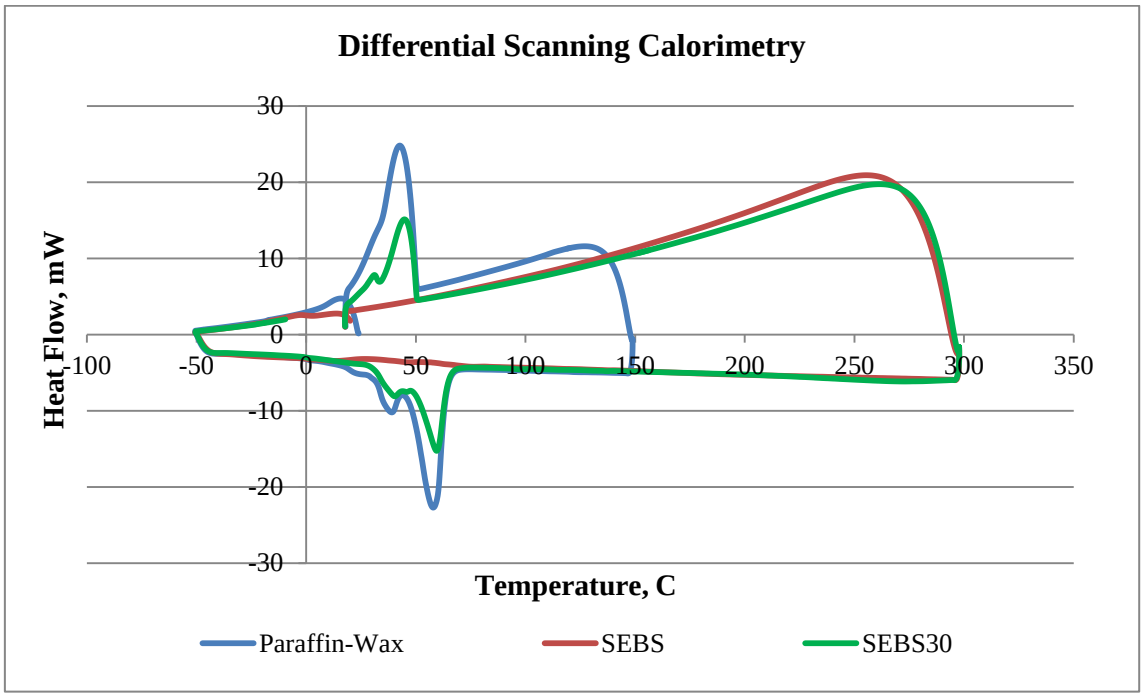

Figure 3–5 Typical Heat Flow vs. Temperature curves of investigated materials

Both kinds of used thermoplastic polymers (SEBS and SIS) show the same trend: the more TPP is contained by the composite, the lower the latent heat of the composite becomes (see Figure 3–6 and Figure 3–7). The addition of 15% of SEBS to the solid wax decreases heat flow by 20%, and 30% of SEBS decreases heat flow by 40%. The addition of 10% of SIS decreases heat flow by 1%, and 30% of SIS decreases heat flow by 48%.

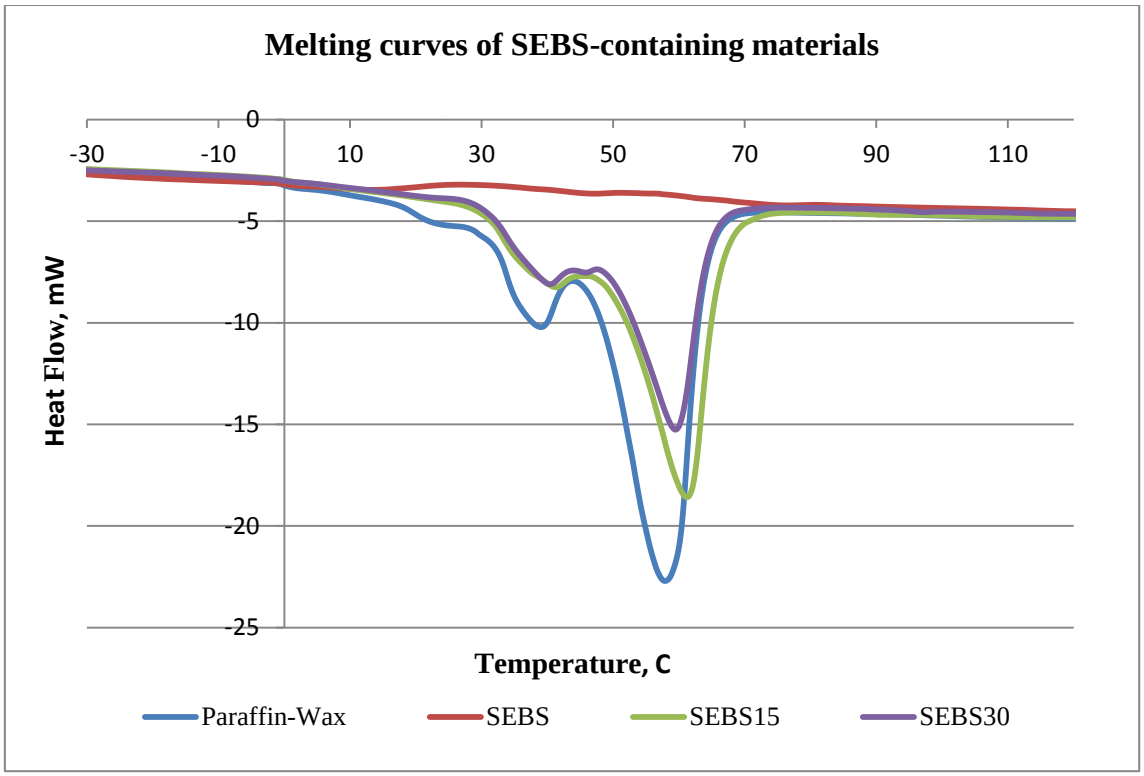

Figure 3–6 DSC melting curves of pure paraffin-wax, pure SEBS, SEBS15 and SEBS30

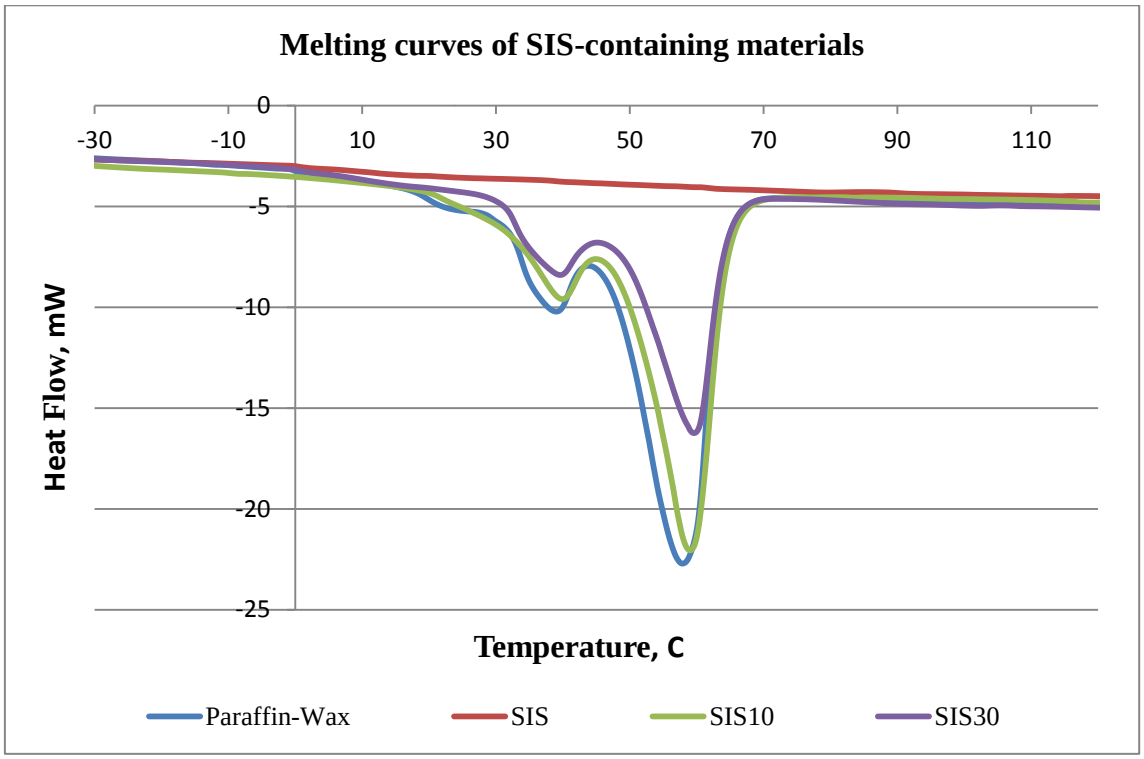

Figure 3–7 DSC melting curves of pure paraffin-wax, pure SIS, SIS10 and SIS30

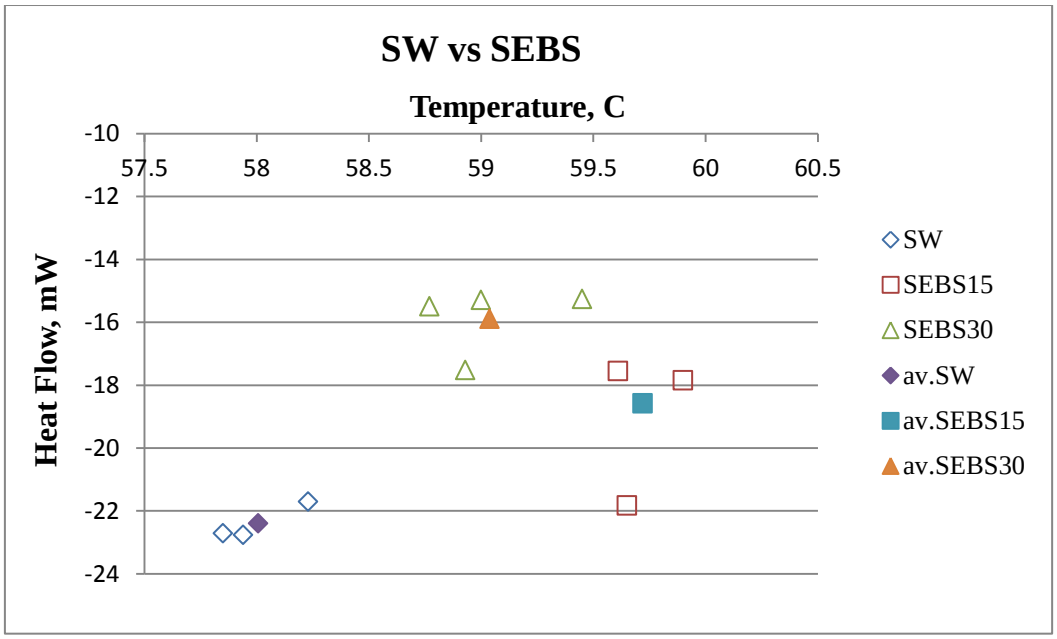

Figure 3–8 Values of Melting point temperature vs. Heat flow. Averaged values are presented

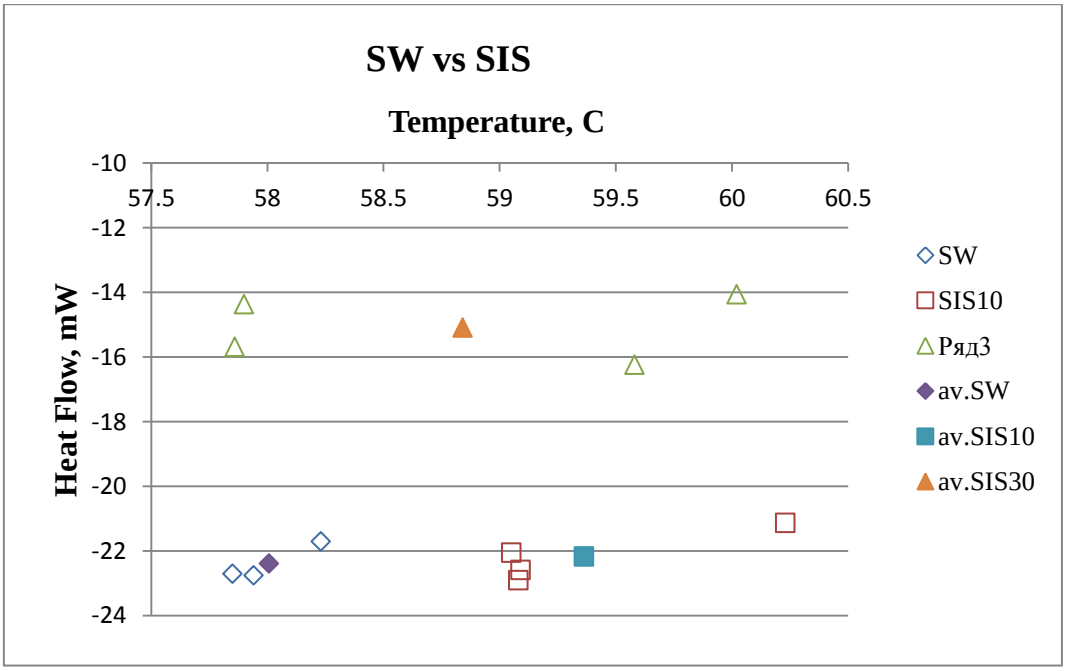

Figure 3–9 Values of Melting point temperature vs. Heat flow. Averaged values are presented.

It can be seen in the Table 3–3 that the change in melting point temperature $T_{melting}$ is not significant, only about 3%.

Table 3–3 Melting point temperatures (averaged value of the performed tests)

Formulation	Melting point temperature $T_{melting}$, °C	Heat flow, mW
Paraffin-wax	58.00	22.5
SEBS15	59.72	18.5
SEBS30	59.04	16
SIS10	59.36	22
SIS30	58.84	15

Conclusions

1. No significant differences in melting point of investigated paraffin based blends have been observed. These is possibly due to the fact that the materials tested, blends of paraffin-wax and thermoplastic polymers, are simply mixtures with no chemical reactions involved into the process of the blends preparation. Thereby, the obtained values of melting temperatures correspond to the paraffin-wax melting, while TPP remains not melted/solid. This can be also proved by the fact that the heat required to reach melted state is less comparing to the pure paraffin-wax (see Table 3–3), because apparently blends contain less paraffin-wax.

3.2.2 Rheological properties

At the most basic level, rheology can be described as the study of how materials flow or, in a broader sense, how materials respond to the application of deformational energy and shear stress. This definition could obviously encompass the entire field of solid and fluid mechanics. In practice, both the field of rheology and the development of rheometric instrumentation have been linked to the study and development of viscoelastic material systems, which may be simply defined as material systems whose properties are time and/or temperature dependent.

Rheometric analyses can therefore be invaluable in characterizing the effects of formulation and processing variables on both the processability and end-use or performance properties of these material systems.

The most basic and widely used form of rheometric instrumentation is the simple steady shear viscometer. A wide variety of existing devices have been developed for the measurement of steady shear viscosity, many of which are specific to a particular industry or material. In principle, however, all of these devices share a common goal: to measure the bulk viscosity of a material as it flows in a steady or continuous fashion. In

fact, the definition of the term “viscosity”, which is the ratio of the applied shear stress to the resulting shear rate, determines the basic design of most of these simple viscometers.

As a comprehensive materials characterization tool, however, the traditional viscometer is of limited use. The most powerful and versatile form of rheometric instrumentation currently in use may be described in general terms as a dynamic shear rheometer or simply a dynamic rheometer. The modern dynamic rheometer shares a basic common concept with the simpler viscometer in that it uses well-defined geometries, such as cone plates, parallel plates or concentric cylinders, to isolate and deform the material in a controlled fashion (see Figure 3–10). A fully functional dynamic rheometer will include steady shear rate capabilities that enable it to be used as a viscometer to measure steady shear or bulk viscosity.

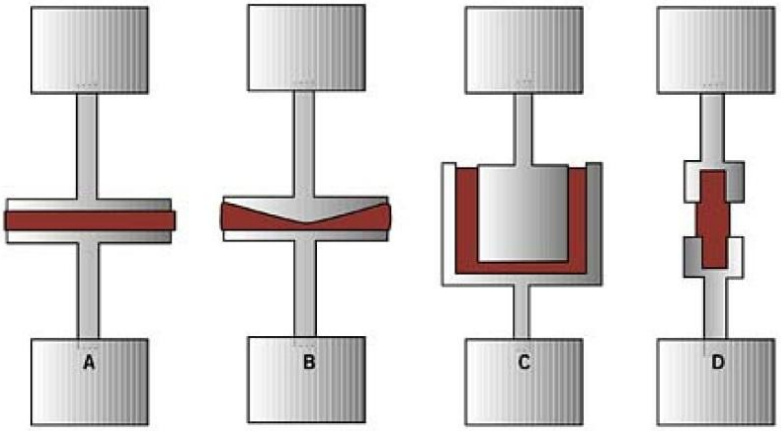

Figure 3–10 Typical sample testing geometries for dynamic rheometers: (A) parallel plates, (B) cone and plate, (C) concentric cylinder (couette), and (D) solid or torsion rectangular. The appropriate geometry is dictated primarily by the properties of sample material, but may also be dictated by the desire to simulate a process or in situ application.

The real power of a dynamic rheometer, however, lies in its unique ability to apply very small amounts of rotation or deformation in a dynamic or oscillatory fashion. It is often useful to visualize this type of dynamic shear testing as if the sample were being “vibrated” between parallel plates or concentric cylinders, as opposed to being sheared in a continuous fashion. The components of a modern dynamic rheometer enable this “vibratory” measurement to be applied to a sample in a controlled fashion while also controlling the sample temperature.

The significance of this dynamic testing method is that the resulting measurement is delivered in terms of discrete components of the material’s viscosity or shear modulus, as opposed to the simple bulk viscosity reported by traditional viscometers. As mentioned previously, viscoelastic materials display time- and temperature-dependent properties. When analyzed using a dynamic rheometer, the

viscosity or shear modulus of a viscoelastic material may be resolved into components parts referred to as the “elastic” and “viscous” components:

$$G_{dyn} = G' + iG'' \tag{3–2}$$

where G_{dyn} is the dynamic shear modulus, G' is the elastic or storage modulus, and G'' is the viscous or loss modulus.

$$G' = \frac{\sigma_0}{\varepsilon_0}\cos(\alpha) \tag{3–3}$$

$$G'' = \frac{\sigma_0}{\varepsilon_0}\sin(\alpha) \tag{3–4}$$

where σ_0 and ε_0 are the amplitudes of stress and strain and α is the phase shift between them.

These component parts of the bulk viscosity or modulus have specific meaning in the context of the bulk properties of the material and are individually very sensitive to specific events occurring in the morphology or microstructure, or even the nanostructure, of the material. These same structural effects or phenomena are typically not captured by traditional, steady-shear viscometry.

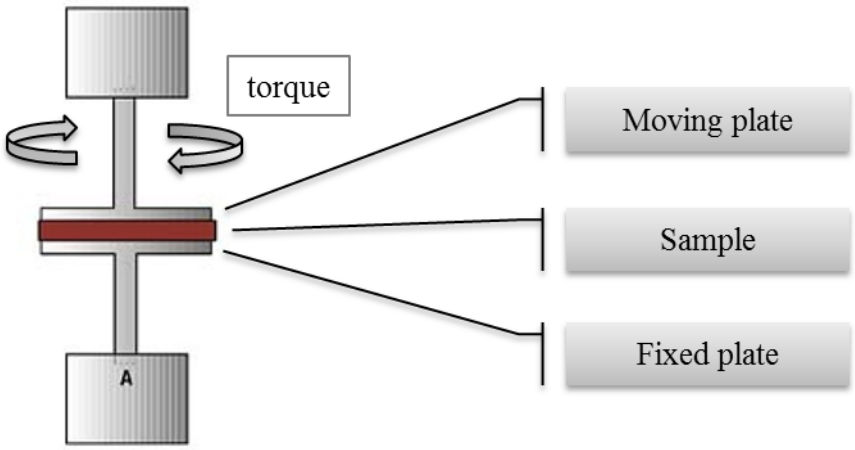

Figure 3–11 Scheme of a parallel-plate rheometer

In order to determine the fuel formulations storage modulus, an investigation was carried out in the oscillatory regime, at small strains, using a parallel-plate rheometer Rheometrics Dynamic Analyzer RDA II TA Instruments (see Figure 3–11) [53]. Applying a sinusoidal deformation, a co-sinusoidal shear rate was obtained, allowing the measurement of viscoelastic properties such as the storage modulus G' and the complex viscosity μ^*. Tests were performed using the TA Instruments apparatus.

Tests conditions

1. Constant strain: 1%;
2. Frequency sweep: (0.5 – 50 Hz);
3. Temperature sweep: (T > 30°C);
4. The sample thickness is 2.5 mm, while the diameter is 25 mm.

Figure 3–12 shows the storage modulus G' measured vs. temperature for the tested formulations strengthened by using SEBS and SIS polymers. The results obtained for pure HTPB and SW are also reported, as reference values.

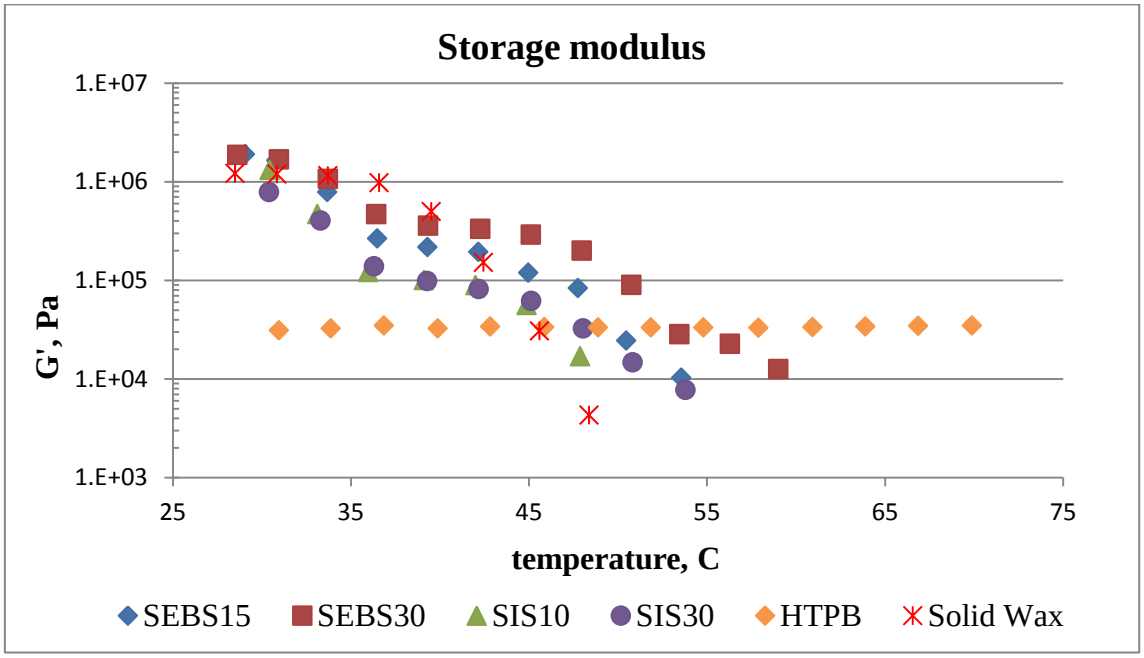

Figure 3–12 Storage modulus vs. temperature in a plate-plate rheometer for tested formulations. Strain=1%. Frequency=1Hz.

Table 3–4 Storage modulus measured for paraffin-based formulations

Fuel Formulation	G', KPa	$T_{melting}$,°C	G' (48°C), KPa
HTPB	30 - 35	-	33
Paraffin-wax	1200 – 4	48	4
SEBS15	1900 – 10	53	85
SEBS30	1900 – 12	59	200
SIS10	1300 – 17	48	17

Conclusions

Several observations can be drawn from the data obtained from rheological investigation (Figure 3–12).

1. An increase of storage modulus value of all formulations is observed compared to pure paraffin-wax. A significant increase of storage modulus is observed for all tested blends comparing to pure paraffin-wax when approaching the melting point temperature (for example, at the temperature 48°C):

   SIS10 shows 4 times increase;

   SIS30 – 7,5 times;

   SEBS15 – 21 times and

   SEBS30 – 50 times.

2. The Initial storage modulus for all investigated paraffinic materials is higher than for HTPB (Table 3–4), which leads to better mechanical properties in standard conditions;
3. The TPP addition effect is the enhanced temperature affect in which the material gives a perceivable rheological response; this means that a TPP prevents paraffin from flowing, up to temperatures higher than the melting temperature of paraffin-wax. For example, data reported on the Figure 3–12 (and Table 3–4) show that the last measurement point for paraffin-wax is obtained at about 48°C, while the last measurement point for SEBS30 is at about 59°C. The temperature up to which the material gives a perceptible rheological response is important because it is linked to the material's tendency to entrainment: the lower the maximum temperature at which a rheological response is obtained, the lower the viscosity, thus the higher the tendency to entrainment and the regression rate. While the melting temperature of HTPB is much higher than 60°C, all tested paraffinic-based materials are expected to show higher regression rate.
4. From the plot (Figure 3–12) it can be observed that the fuel formulation containing 30% of SEBS at every step of measured temperature shows higher values of storage modulus.

3.2.3 The effect of aging on rheological properties

The aging effect was observed during testing paraffin-based fuels for hybrid propulsion systems [7]. Rheological properties of the samples of SEBS15 (fresh) were tested during 24 hours after they were prepared, and were compared to those that were stored at 25°C for three weeks. The experimental investigation was carried out under the same testing conditions (see Chapter 3.2.2).

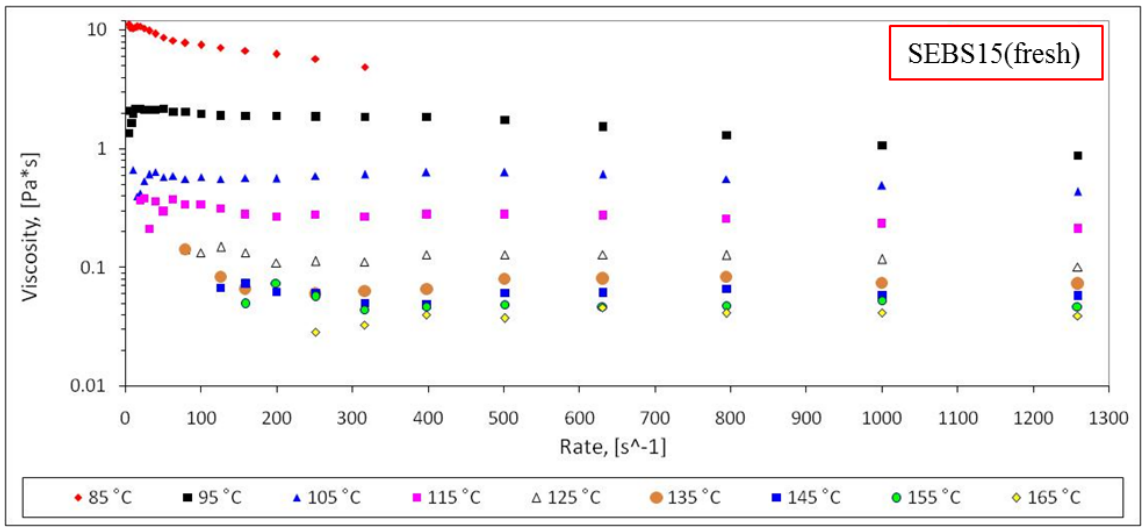

Figure 3–13 Temperature scan of viscosity in the range 85 °C – 165 °C for fresh samples of SEBS15 material (adopted from Boiocchi M. [7]).

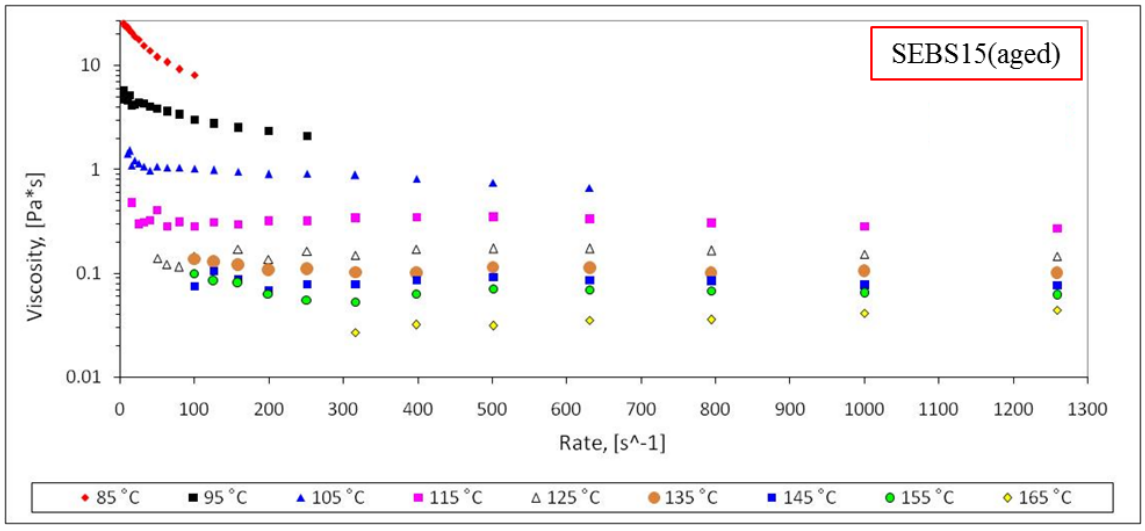

Figure 3–14 Temperature scan of viscosity in the range 85 °C – 165 °C for aged samples of SEBS15 material (adopted from Boiocchi M. [7]).

The viscosity of the aged samples is higher than that of the freshly prepared blends at low temperatures but this difference becomes less clear when the temperature is increasing. Tests of the aged formulations at 85, 95 and 105 °C were stopped when the maximum limit of torque was reached, at values of 100, 250 and 630 s^{-1} respectively.

Table 3–5 Complex viscosity values obtained with Couette rheometer tests at 1000 s-1

Mixture	**Complex viscosity values at 1000 s-1**							
Temperature	**95**	**105**	**115**	**125**	**135**	**145**	**155**	**165**
SEBS15 fresh	1.071	0.491	0.236	0.118	0.074	0.059	0.053	0.042
SEBS15 aged	-	-	0.285	0.153	0.106	0.078	0.064	0.041

Conclusions

1. As can be seen from this experiment, storing paraffin-based fuels doped with a thermoplastic polymer such as SEBS affects their rheological properties. Complex viscosity increases when material is stored for three weeks.

3.2.4 Mechanical Properties

Tensile tests measure the force required to break a plastic sample specimen and the extent to which the specimen stretches or elongates to that breaking point. Tensile tests produce stress-strain diagrams used to determine tensile modulus. The resulting tensile test data can help specify optimal materials, design parts to withstand application forces, and provide key quality control checks for materials.

Tensile tests for plastics provide:

- Tensile Strength (at yield and at break)
- Tensile Modulus
- Tensile Strain
- Elongation and Percent Elongation at yield
- Elongation and Percent Elongation at break

Tensile tests have been conducted using MTS 858 Material Testing System and according to the standard ISO 527 “Plastics — Determination of tensile properties” [54], [55].

Figure 3–15 MTS 858 Material Testing System

The MTS 858 system provides a broad range of test enhancing features, including:

- Force ranges from 5 kN (1.1 kip) to 25 kN (5.5 kip);
- The ability to test lower strength materials ranging from plastics to aluminum;
- Accommodation of subsized to standard specimens;
- The capability to perform tension, compression, bend and fatigue tests; specialized tests for biomedical and biomechanical testing; and durability testing on small components;
- Wide column spacing to accommodate larger fixtures, environmental chambers and furnaces.

The test specimens are dumb-bell-shaped type 1B, as shown on the Figure 3–16 and Table 3.3.1. Due to the brittle nature of the paraffin-wax material the sample's thickness was chosen to be 10 mm.

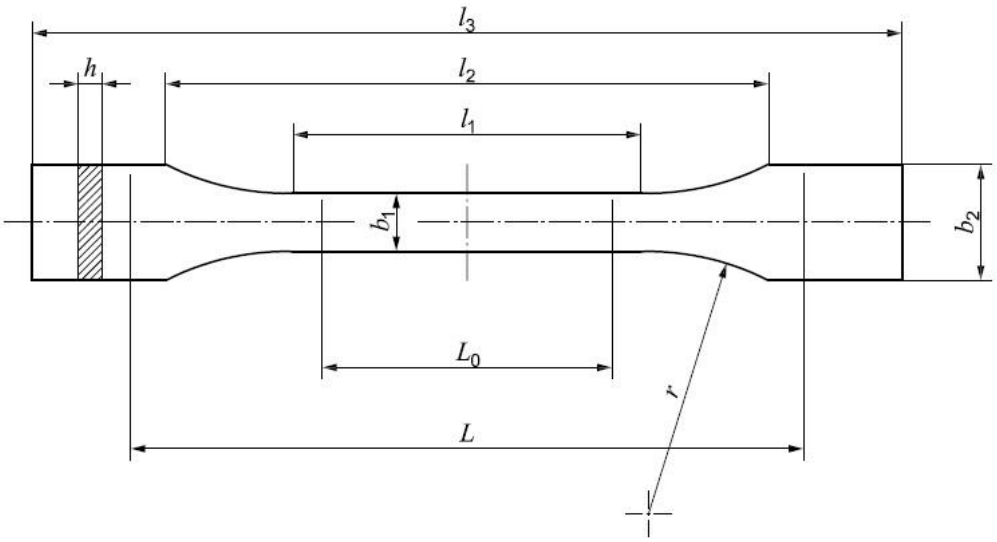

Figure 3–16 Type 1A and 1B test specimen dimensions

Table 3–6 Dimensions of type 1A and 1B test specimens

Dimensions in millimetres

	Specimen type	1A	1B
l_3	Overall length[a]	170	≥150
l_1	Length of narrow parallel-sided portion	80 ± 2	60,0 ± 0,5
r	Radius	24 ± 1	60 ± 0,5
l_2	Distance between broad parallel-sided portions [b]	109,3 ± 3,2	108 ± 1,6
b_2	Width at ends	20,0 ± 0,2	
b_1	Width at narrow portion	10,0 ± 0,2	
h	Preferred thickness	4,0 ± 0,2	
L_0	Gauge length (preferred)	75,0 ± 0,5	50,0 ± 0,5
	Gauge length (acceptable if required for quality control or when specified)	50,0 ± 0,5	
L	Initial distance between grips	115 ± 1	115 ± 1

[a] The recommended overall length of 170 mm of the type 1A is consistent with ISO 294-1 and ISO 10724-1. For some materials, the length of the tabs may need to be extended (e.g. l_3 = 200 mm) to prevent breakage or slippage in the jaws of the testing machine.

[b] $l_2 = l_1 + [4r(b_2 - b_1) - (b_2\text{-}b_1)^2]^{1/2}$, resulting from l_1, r, b_1 and b_2, but within the indicated tolerances.

Test procedure

Specimens are placed in the grips of the machine and pulled until failure. For ISO 527-1 [54] the test speed may be determined by the material specification. The chosen default test speed is 50 mm/min. An extensometer and strain gauge are used to determine elongation and tensile modulus.

Tests conditions

1. Standard ambient conditions: the temperature is 25°C and the ambient pressure is 1 bar;
2. Constant test speed 50 mm/min;
3. The sample dimensions are fitted to the ISO 527-2 standard specimen type 1B, while the sample thickness is 10 mm [55];
4. Tested formulations SEBS15, SEBS30, SIS30;
5. The samples are manufactured by pouring the mixture into the mould.

Postprocessing the tests data [54]

All stress values were calculated using the following equation:

$$\sigma_{mech} = \frac{F}{A} \qquad 3–5$$

where σ_{mech} is the stress value in question, expressed in megapascals (MPa); F is the measured force concerned, expressed in newtons (N); A is the initial cross-sectional area of the specimen, expressed in square millimetres (mm2).

All strain values were calculated using the following equation:

$$\varepsilon_{mech} = \frac{\Delta L_0}{L_0} \qquad 3–6$$

where ε_{mech} is the strain value in question, expressed as a dimensionless ratio, or as a percentage; L_0 is the gauge length of the test specimen, expressed in millimetres (mm) (see Figure 3–16); ΔL_0 is the increase of the specimen length between the gauge marks, expressed in millimeters (mm).

Using calculated values the stress σ_{mech} – strain ε_{mech} plots were built for each test and each material formulation (Figure 3–18, Figure 3–19, Figure 3–20).

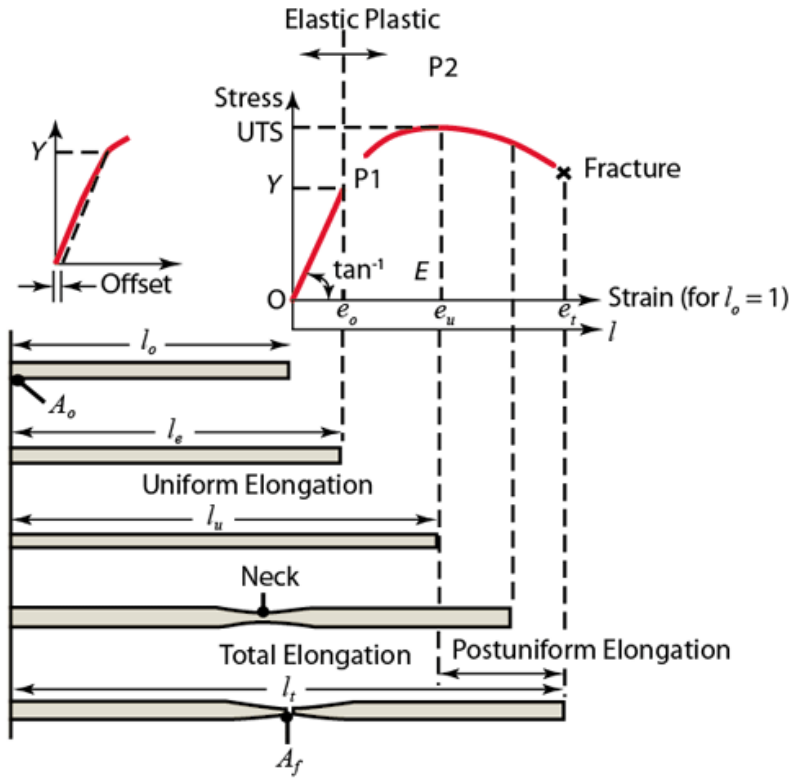

Figure 3–17 Typical stress-strain curve

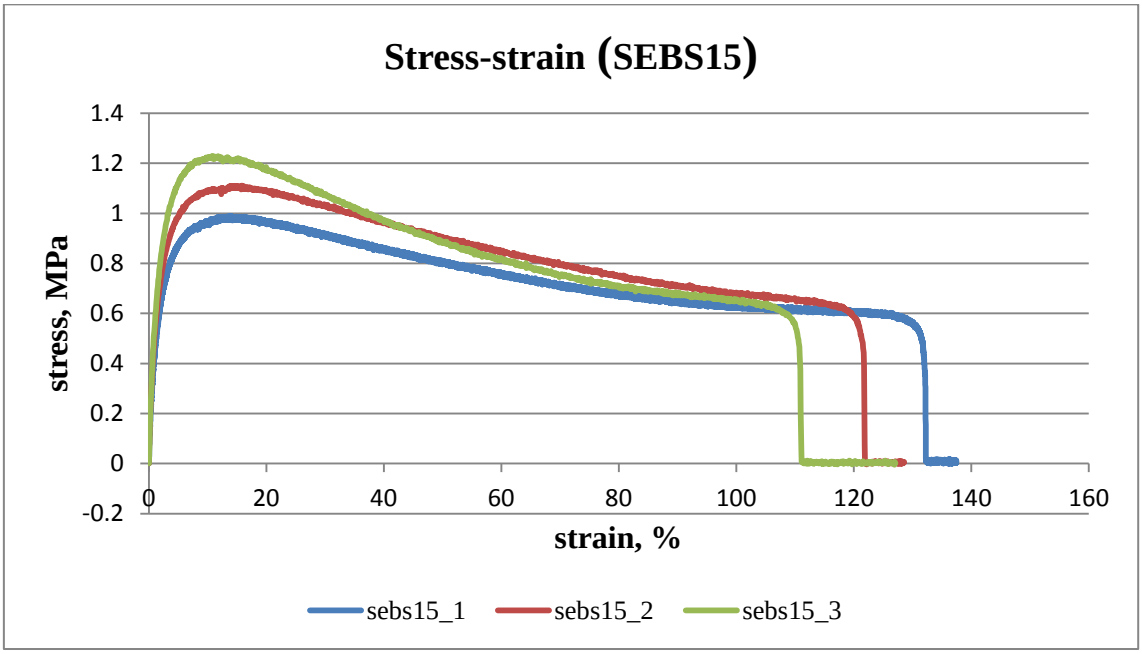

Figure 3–18 Stress-strain curves of SEBS15

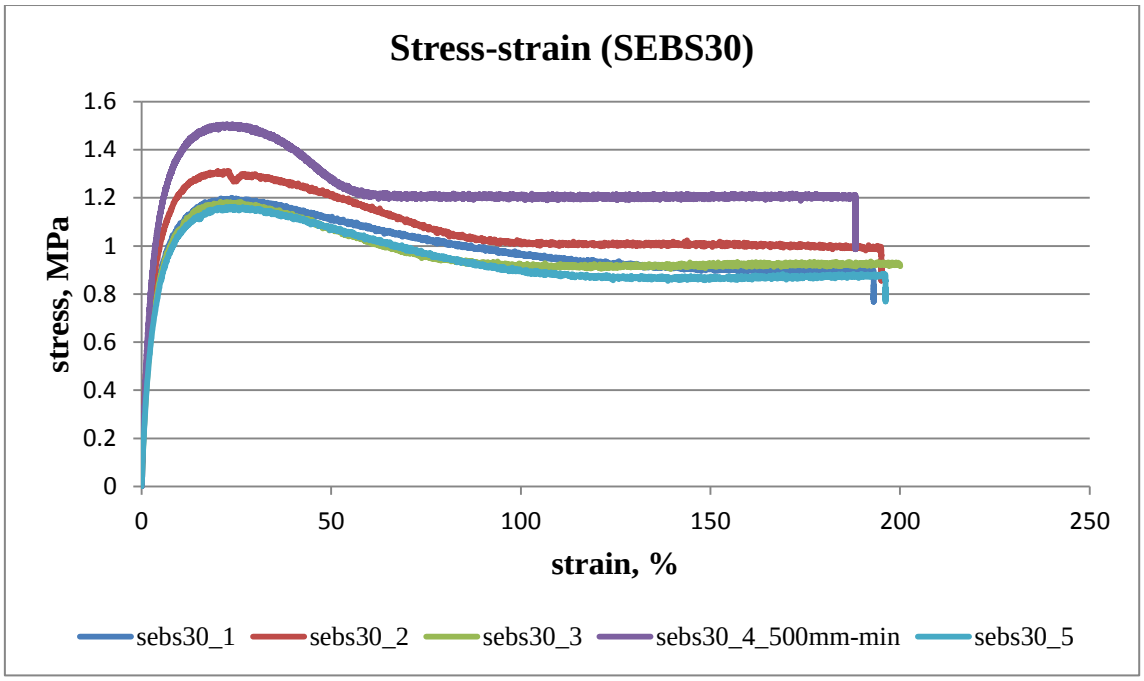

Figure 3–19 Stress-strain curves of SEBS30

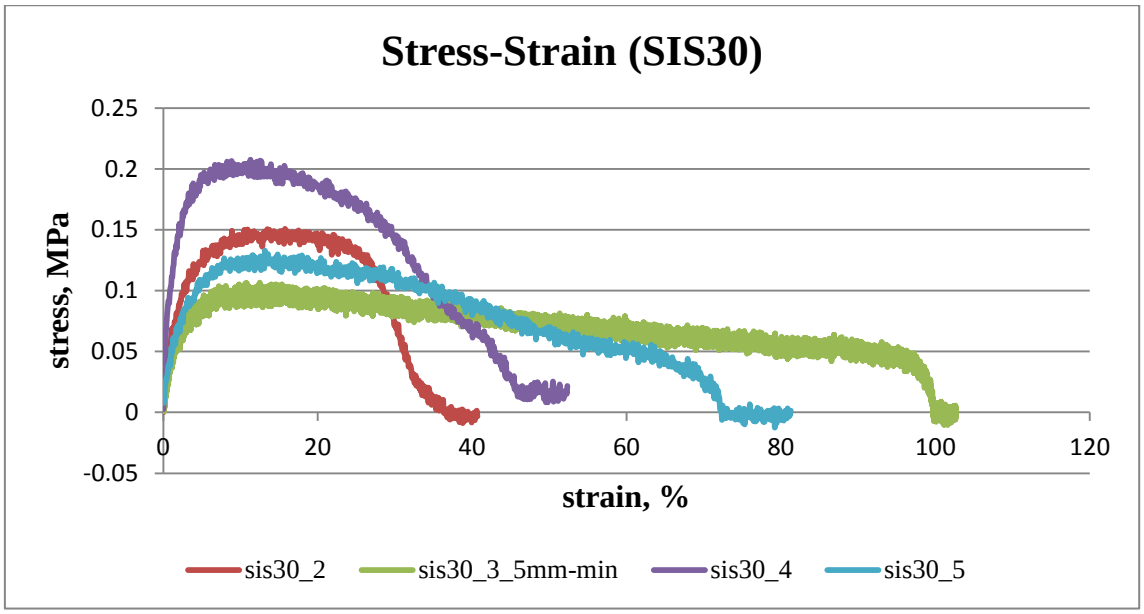

Figure 3–20 Stress-strain curves of SIS30

With computer-aided equipment, the determination of the values of tensile modulus E_t are calculated using a linear regression procedure applied on the part of the curve between two points (Figure 3–21).

$$E_t = \frac{d\sigma_{mech}}{d\varepsilon_{mech}} \qquad 3–7$$

where $\frac{d\sigma_{mech}}{d\varepsilon_{mech}}$ is the slope of a least-squares regression line fit to the part of the stress/strain curve in the strain interval $0{,}0005 \leq \varepsilon_{mech} \leq 0{,}0025$, expressed in megapascals (MPa).

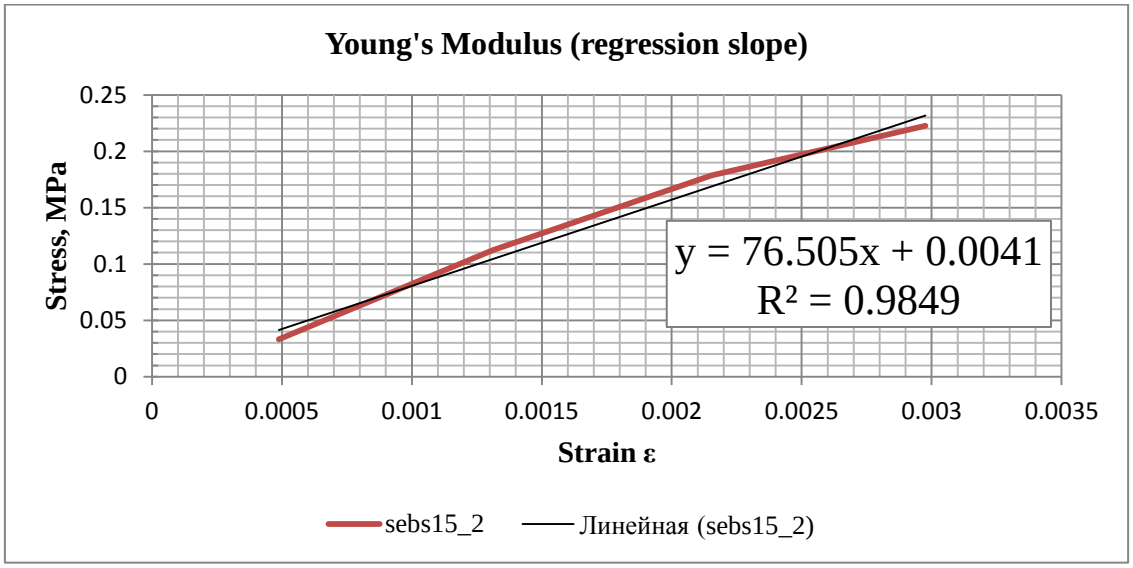

Figure 3–21 Determination of Young Modulus values using regression slope method by means of PC. The formulation is SEBS15, test #2. The obtained Young Modulus is 76.5 MPa

The postprocessed results are compared against the results obtained for SEBS15, SEBS30, SIS30 shown below. There are plots of the maximum tensile strength (Figure 3–22), the maximum strain (at break) (Figure 3–23) and Young Modulus (Figure 3–24).

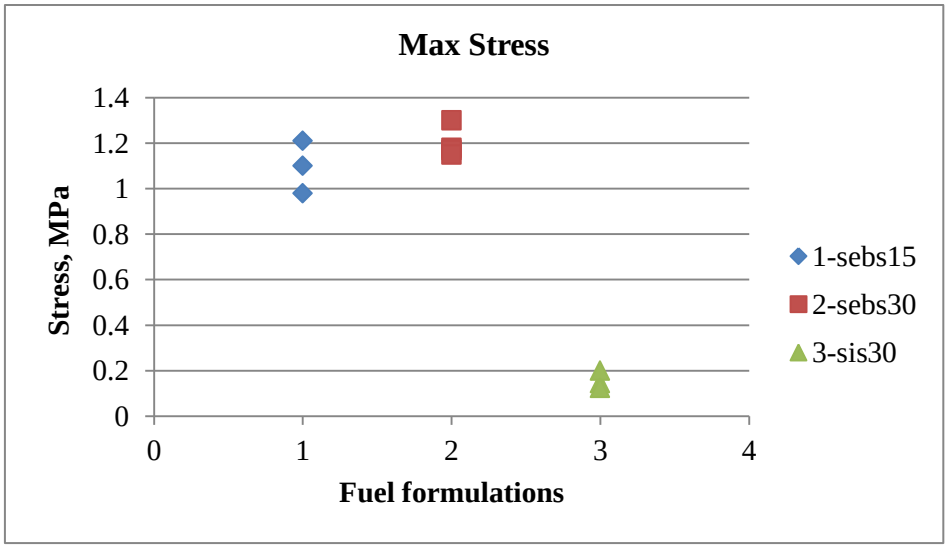

Figure 3–22 Maximum values of tensile strength σ_{mech}

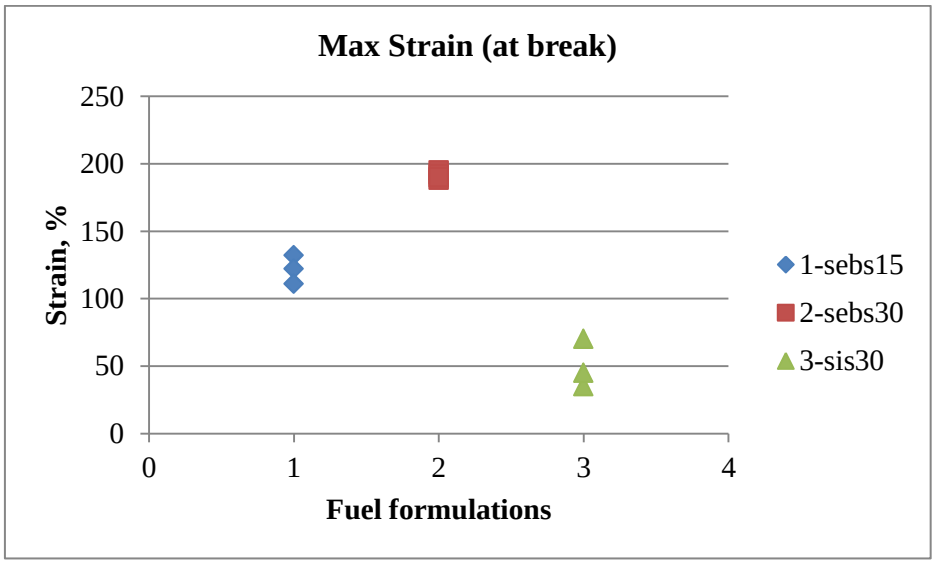

Figure 3–23 Maximum values of strain ε_{mech}

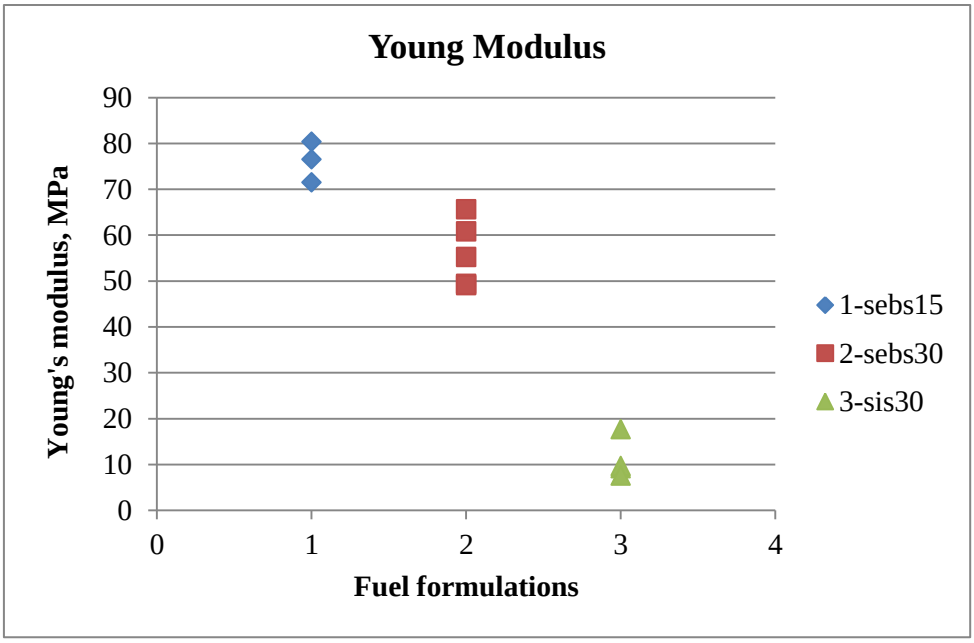

Figure 3–24 Values of Young Modulus E

The values of maximum tensile strength, maximum strain (at break) and calculated Young Modulus values are presented in the table below.

Table 3–7 Values of maximum tensile strength, maximum strain (at break) and calculated Young Modulus of tested materials

Formulation	# test	Max tensile strength, MPa	Max strain, %	Young Modulus, MPa
SEBS15	1	0.98	132	71.495
	2	1.1	122	76.505
	3	1.21	111	80.359
SEBS30	1	1.18	188*	55.281
	2	1.3	195*	60.823
	3	1.17	192*	49.376
	4	1.15	190*	49.098
SIS30	1	0.146	35	9.2053
	2	0.2	45	17.71
	3	0.125	70	7.6073

* values of maximum strain (at break) for the formulation which contains 30% of SEBS as a strengthening additive are not correct due to the fact that all the samples showed good elastic properties and were not broken due to the limited maximum elongation provided by MTS 858 Material Testing System. See Figure 3–26.

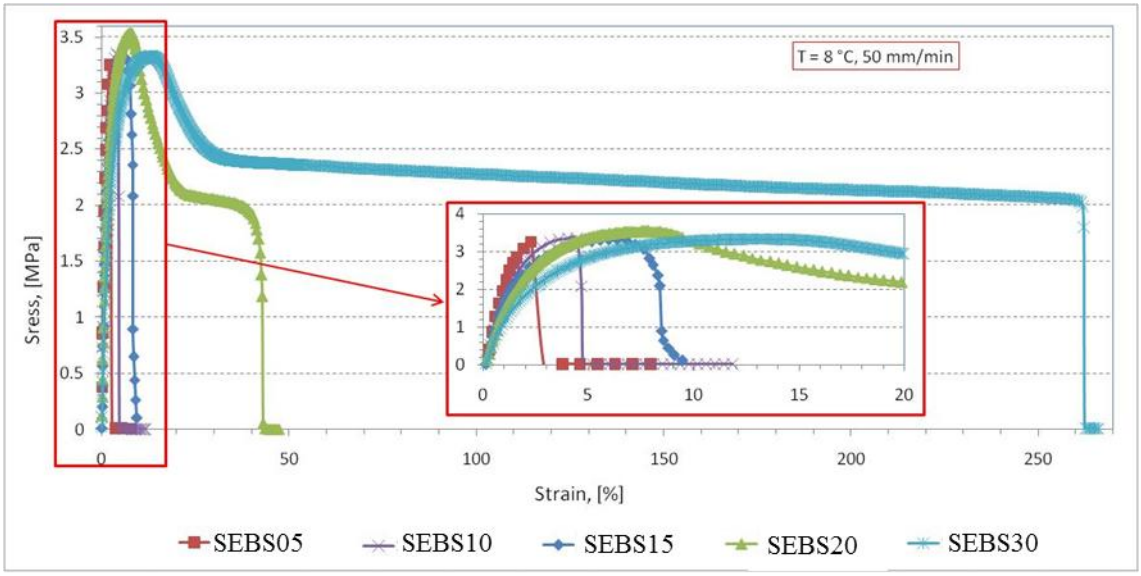

Figure 3–25 Effect of polymer's mass fraction on the elongation at break (adopted from M.Boiocchi [7])

Conclusions

Mechanical properties investigation by tensile tests revealed:

1. The use of SEBS as a strengthening additive gives significantly (nearly an order of magnitude) more strength to the paraffinic mixture compared to SIS;
2. The higher the percentage of SEBS is contained by the mixture the more strength the material possesses;
3. Samples containing SEBS showed higher elasticity than those containing SIS;
4. In spite of the fact that the samples containing 30% of SEBS were not broken due to the limited elongation of the testing machine and the maximum strain values are not the real strain for this material, it can be concluded that the strain at break for SEBS30 is about 2 times higher than that of SEBS15 and more than 4 times higher compare to with SIS30.
5. It can be seen that Young modulus values of SEBS15 are higher than those of SEBS30, which had not been expected. According to the literature a typical Young modulus for a TPP lies in range 10-1GPa, while for pure paraffin it's lower about 200MPa [56]. But it can be explained that in such mixtures of a paraffin-wax and a thermoplastic polymer the properties cannot be simply inherited from the ingredients. Also, the crystallization of paraffin-wax can influence the values of Young modulus.
6. The formulations containing SEBS have significantly higher (5-7 times) Young modulus than formulations containing SIS.

Figure 3–26 Samples of each tested formulation after tensile tests were performed. SIS30, SEBS15, SEBS30 respectively

3.3 Conclusions and Future Developments

Paraffin-based solid fuels for hybrid rockets were characterized by means of multiple experimental approaches in the framework of research aimed at developing a new generation of solid fuels, combining at the same time good ballistic and suitable mechanical properties.

A material strengthening strategy (a thermoplastic polymer addition) was investigated in this work. Two kinds of thermoplastic polymers were considered: SEBS and SIS. Homogeneous fuels are obtained, allowing isotropic mechanical properties. SEBS-containing formulations showed better mechanical properties in terms of tensile strength and maximum strain. The increase is significant with respect to pure paraffin.

Previous investigations [6], [5] showed that a decrease of viscosity increases the regression rate. This trend is connected to the increasing development of entrainment phenomena, which strongly increases the regression rate. The present materials investigation revealed that all blends have no significant difference in melting point values (about 3%) with respect to pure paraffin-wax. Rheological investigation showed a slight increase in storage modulus when approaching the melting point which suggests that the SEBS- and SIS-containing formulations could have similar values of regression rate, and similar to pure paraffin regression rates.

Taking into account the fact of significant improvement of mechanical properties when paraffin-wax doped with a TPP, it can be concluded that such blends are quite promising for the use as hybrid rocket solid fuels.

More formulations containing different percentage of SEBS and SIS must be tested to obtain clear trends of mechanical properties, especially such as Young Modulus.

Combustion tests must be performed to obtain regression rate data of the TPP-containing paraffin-based composites in order to correlate rheological and mechanical properties with ballistic properties of fuels.

4 PARAFFIN-BASED FUELS: NUMERICAL MODEL DEVELOPMENT

The modeling of multi-phase non-premixed turbulent combustion is described generally in this chapter. The equations governing the transport of momentum, species, heat, and turbulence are described as well as the assumptions and equations used for modeling chemical reactions and the interaction between the condensed and gaseous phases.

Model has been developed during the trainee at NUMECA International, Brussels.

4.1 RANS equations

To model the quasi-steady-state turbulent flow in the combustor, the Reynolds-averaged Navier Stokes (RANS) methodology is used whereby the effects of the turbulent eddies are treated according to the Boussinesq hypothesis, meaning that they can be modeled as an additional diffusion of the mean velocity field, via the eddy viscosity, μ_T, in the steady-state momentum transport equation shown below where u_i is the i^{th} component of the gas velocity vector and ρ is the gas density. Coupling the continuity equation with the momentum equation leads to a set of four equations in three dimensions to give a solution for the three velocity components and the scalar pressure field. These equations are incomplete however until a method for accounting for the eddy viscosity is defined [57].

$$\frac{\partial}{\partial x_j}\left(\rho u_i u_j\right) + \frac{\partial P}{\partial x_i} = \frac{\partial}{\partial x_j}\left[\left(\mu + \mu_T\right)\frac{\partial u}{\partial x_j}\right] \qquad 4\text{–}1$$

$$\frac{\partial}{\partial x_i}\left(\rho u_i\right) = 0 \qquad 4\text{–}2$$

Methods for closing the eddy-viscosity term have been the subject of decades of research and have produced a wide array of turbulence models ranging from very simple algebraic models to approaches that solve several extra coupled transport equations and even resolve individual components of the turbulent shear stress tensor [58].

The most widely-used turbulence models, however, fall into the family of so-called two-equation models that solve two additional transport equations for the

turbulent kinetic energy, k, and its dissipation rate, usually represented as ϵ. In the k-equation shown below, turbulent kinetic energy is destroyed by the dissipation rate and also by self-diffusion but is generated by gradients in the velocity field, represented as the source term S_k. The dissipation rate equation, also shown below, has several source and sink terms that account for the several modes of generation and destruction of the dissipation rate; ε is generated proportional to the generation of turbulence, S_k, but is also self-destroying proportion the square of itself in the final source term [59].

$$\frac{\partial}{\partial x_j}(u_i \rho k) = \frac{\partial}{\partial x_j}\left[(\mu + \mu_T)\frac{\partial k}{\partial x_j}\right] - \rho\epsilon + S_k \qquad 4\text{–}3$$

$$\frac{\partial}{\partial x_j}(u_i \rho \epsilon) = \frac{\partial}{\partial x_j}\left[\left(\mu + \frac{\mu_T}{1.3}\right)\frac{\partial \epsilon}{\partial x_j}\right] + 1.44 S_k \frac{\epsilon}{k} - 1.92\,\rho\frac{\epsilon^2}{k} \qquad 4\text{–}4$$

Finally, the eddy viscosity, μ_T, is defined in the equation below as the ratio of k^2 to ε, with the constant of proportionality, C_μ, is usually taken to be 0.09. These equations together give a consistent closure for the eddy-viscosity μ_T, required in the momentum equation. This particular closure has been applied to many different flow scenarios and it has also been extended to include additional physical phenomena that affect the turbulence such as entrained particles and chemical reactions among others.

$$\mu_T = C_\mu \rho \frac{k^2}{\epsilon} \qquad 4\text{–}5$$

For non-isothermal simulations, the energy equation must also be solved, typically as a variant of the transport equation that is shown below, where h, Pr, Pr_T, and T represent enthalpy, Prandtl number, turbulent Prandtl number, and temperature respectively. $S_{reaction,}$ in this equation, is the energy source term resulting from the sensible heat released by chemical reactions.

$$\frac{\partial}{\partial x_j}(\rho u_i h) = \frac{\partial}{\partial x_j}\left[c_p\left(\frac{\mu}{Pr} + \frac{\mu_T}{Pr_T}\right)\frac{\partial T}{\partial x_j}\right] + S_{reaction} \qquad 4\text{–}6$$

4.2 Multiphase reacting flow. Mathematical model

With the basis described above, further assumptions must be made and additional equations must be solved on order to extend the models' abilities to be able to account for the effects of species transport and chemical reactions. This is described in two sections, the first of which deals with the treatment of these physics in the continuous phase, and second, the treatment of small condensed-phase fuel droplets and particles with a Lagrangian approach.

4.2.1 Eulerian. Mixture fraction approach. Flamelet model

For reacting flows the continuous-phase species concentrations can be accounted for in an Eulerian framework by solving additional transport equations such as the one shown below which represents the steady-state transport of the concentration Y of species k below where Sc and Sc_T are the molecular and eddy Schmidt numbers respectively. The source term $\dot{Y}_k$ represents the net production or destruction rate of the species by chemical reactions.

$$\frac{\partial}{\partial x_j}(\rho u_i Y_k) = \frac{\partial}{\partial x_j}\left[\left(\frac{\mu}{Sc} + \frac{\mu_T}{Sc_T}\right)\frac{\partial Y_k}{\partial x_j}\right] + \dot{Y}_k \qquad 4\text{–}7$$

For a simulation were N species are to be considered, typically N-1 species transport equations are solved and the constraint that $\sum Y_k = 1$ is imposed by assuming that the concentration of the Nth species is assumed inert and non-participating and simply calculated as the remainder from the balance of the N-1 species for which transport equations are solved. This adds stability to the numerical scheme which can be critical especially where species concentrations affected by stiff Arrhenius rate reaction equations for example.

In some non-premixed reacting flows, the species transport of all fuel-derived species can be simplified to a single transport equation for a single, representative species, the so-called mixture fraction *f*. If the chemistry of the reactions is sufficiently fast, the reactions can be seen as mixing-limited and the combustion problem reduced to a mixing problem and the chemical composition of the flow and its local physical and thermodynamic properties can be uniquely determined by the characteristics of the turbulent mixing between the fuel and non-fuel streams [60].

$$\frac{\partial}{\partial x_j}(\rho u_i f) = \frac{\partial}{\partial x_j}\left[\left(\frac{\mu}{Sc} + \frac{\mu_T}{Sc_T}\right)\frac{\partial f}{\partial x_j}\right] \qquad 4\text{–}8$$

To account for the first moment of the temporal distribution of the various species, the mixture fraction approach can be extended by solving an additional transport equation to solve for the mixture fraction variance f'^2, as shown below [61], [62]. The mixture fraction variance equation is essentially the same in its convection and diffusion terms as the equation for *f*, but adds a source term for the production of the variance proportional to the square of the mixture fraction gradient and a since term for the destruction rate of mixture fraction variance in the presence of turbulent dissipation. In practice the value of f'^2 is usually capped at 0.25 to prevent the variance from spanning an unrealistically large segment of its available space from 0 to 1.

$$\frac{\partial}{\partial x_j}(\rho u_i f'^2) = \frac{\partial}{\partial x_j}\left[\left(\frac{\mu}{Sc} + \frac{\mu_T}{Sc_T}\right)\frac{\partial f'^2}{\partial x_j}\right] + 2.85(\nabla f)^2 - 2\rho\frac{\epsilon}{k}f'^2 \qquad 4\text{–}9$$

The detailed physical and thermodynamic properties of the flow are then assumed under the mixture fraction approach to be functions of only *f* and f'^2 and since the values of these variable are tightly bounded, lookup tables can be constructed a priori to eliminate the need of calculating these values in situ thus offering an enormous speed advantage over solving the individual species' transport equations separately and allowing for any number of pretabulated chemistry treatments, such as equilibrium or flamelet models, to be used without significantly changing the governing equations.

Modeling the flame with a flamelet approach attempts to improve the realism of the turbulent chemistry by incorporating strain rate effects. To do this, the non-premixed turbulent flame is assumed to be composed of myriad idealized contra-flow diffusion flames with varying stoichiometries and strain rates. A one-dimensional detailed chemistry solver is used to simulate these contra-flow flames given the compositions of the fuel and oxidizer streams. Such one-dimensional flames are simulated at many conditions across the full spectrum of the expected mixture fraction and strain rate envelopes. The flames are sampled and compiled into lookup tables for all of the necessary thermodynamic properties of the flow like density, temperature, enthalpy, product composition, etc. as functions of mixture fraction, mixture fraction variance, and strain rate, a, as given below [61]

$$\rho, T, h, Y = lookup\ table(f, f'^2, a) \qquad 4\text{–}10$$

4.2.2 Lagrangian

When entrained particles and droplets of fuel are important to the combustion process, their small size typically prohibits their treatment within the Eulerian framework of the transport equations described previously. The motion and temperature of these particles in the domain of simulation can be simulated by solving the Lagrangian-frame equations of motion for immersed, drag-force affected solid spheres as shown below where the subscripts f and p represent the fluid and particle properties respectively.

$$\frac{d\vec{u}_p}{dt} = C_D \frac{3\rho_f}{4\rho_p D_p} |\vec{u}_f - \vec{u}_p| (\vec{u}_f - \vec{u}_p) \qquad 4\text{–}11$$

$$m_p c_p \frac{dT_p}{dt} = hA_p (T_f - T_p) + \varepsilon_p A_p \sigma (T_f^4 - T_p^4) \qquad 4\text{–}12$$

These ordinary differential equations for the particle trajectories can then be integrated through the domain volume using Runge-Kutta techniques to take into account the variations in the fluid velocity and temperature along each particle's path. While the mean velocity components may be sufficient, the effect of turbulent dispersion of the particles can be simulated by adding random fluctuations in the fluid velocity according to the local turbulence characteristics as estimated from the local values of k and ε. The dispersed particle "cloud" can then be simulated in a Monte-Carlo fashion by simulating a large number of particle tracks and tracking the resulting distribution [44].

4.2.3 Spray combustion. Coupling of Eulerian and Lagrangian

If the mass of the particles is very small, the interaction between the gas and condensed phases can be safely neglected, however in combustion simulation where a significant fraction of the fuel or oxidizer mass is contained in the condensed phase, the effect of the fluid and the particles described previously is still valid however the revers effect where the reaction of the cumulative drag forces on all of the particles affects the balance of the momentum equation. In this case the negative of the cumulative drag on the particles in each computation cell in the Eulerian simulation can be included as a source term on a cell by cell basis which is shown in the equations below.

$$\frac{\partial}{\partial x_j}\left(\rho u_i u_j\right) + \frac{\partial P}{\partial x_i} = \frac{\partial}{\partial x_j}\left[\left(\mu + \mu_T\right)\frac{\partial u}{\partial x_j}\right] + S_{Drag} \qquad 4\text{–}13$$

$$S_{Drag} = -\frac{1}{V_{cell}}\sum \frac{d\left(m_p \vec{u}_p\right)}{dt} \qquad 4\text{–}14$$

Likewise for the mixture fraction equation for example, the evaporating mass of the fuel droplets can be added as a source term with the conservation of mass being maintained since the mass gained cell is equal to the mass lost by the particles.

$$\frac{\partial}{\partial x_j}\left(\rho u_i f\right) = \frac{\partial}{\partial x_j}\left[\left(D_f + \frac{\mu_T}{Sc_T}\right)\frac{\partial f}{\partial x_j}\right] + S_{evap} \qquad 4\text{–}15$$

$$S_{evap} = \frac{1}{V_{cell}}\sum \dot{m}_{evap} \qquad 4\text{–}16$$

As a result of using this methodology, the user effectively has two separate simulations in progress, one for the eulerian variables and one for the lagrangian particles. Since each simulation affects the other, care must be taken to ensure proper convergence. For the Eulerian simulation this usually means that a large number of Lagrangian particles are used so that the resulting source terms are smoothly distributed throughout the domain. For the Lagrangian simulation the particle trajectories must be recalculated sufficiently often within the Eulerian simulation convergence process that the Eulerian simulation converges at roughly the same rate as the Lagrangian, but not so often that the Eulerian solution becomes unstable due to the rapidly changing source terms. Properly under-relaxing the source terms can enhance the convergence behavior of these coupled simulations dramatically.

4.2.4 Inlet diffusion

Inlet diffusion is a phenomenon in numerical simulations of species transport where steep gradients in species concentrations adjacent to the inlet boundaries change the net flux of species through these boundaries. In the case of the simulations presented here, where the oxidizer flows across the fuel inlet, the low-mixture fraction concentration in the freestream, along with the high turbulence intensity leads to the existence of a steep mixture fraction gradient immediately adjacent to the fuel boundary. Since the mixture fraction equation uses a Dirichlet boundary condition at this boundary, and since the fuel inlet has relatively low velocity and momentum, additional mixture fraction is diffused into the flow. This significantly affects the

balance in the global mixture fraction, and drastically affects flame structure (see Figure 4–1).

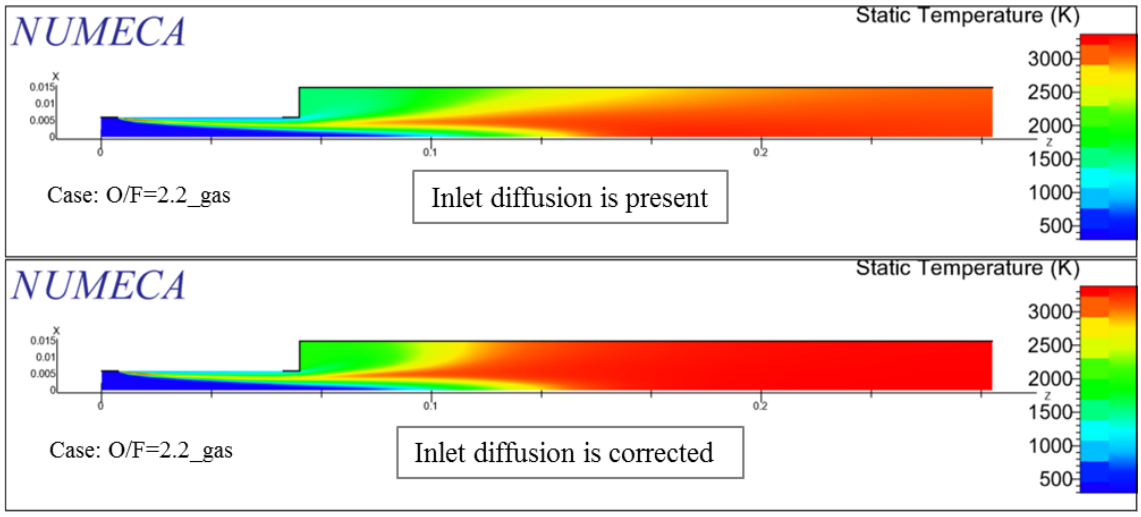

Figure 4–1 Demonstration of Inlet Diffusion phenomenon through its effect on temperature field.

For example, in the simulation below, the O/F ratio defined by the user is nominally 2.2. In this situation the downstream mixture fraction should be 0.313.

$$f = \frac{1}{1 + O/F} \qquad 4\text{–}17$$

$$f = \frac{1}{1 + 2.2} = 0.313$$

Due to the additional mixture fraction diffused through the fuel inlet, the global mixture fraction is higher at 0.384.

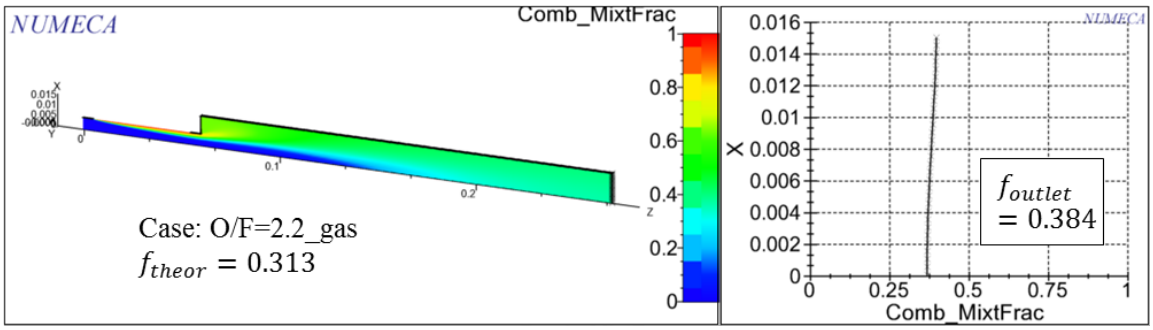

Figure 4–2 Uncorrected inlet diffusion in a simulation with mass and oxidizer flows that have been specified to be equal. The global mixture fraction in this case should be 0.313, however, due to the additional diffusion of mixture fraction from the fuel inlet, the downstream mixture fraction is 0.384. Case: O/F=2.2_gas.

Several attempts were made to solve the inlet diffusion problem, which are described, along with a more thorough description of the inlet diffusion problem, in B Appendix. Inlet Diffusion Problem. Finally however, the solution to the problem as implemented in all of the simulations in this thesis, consisted of using the FINE/Open extension package OpenLabs, to hard code the diffusion coefficient $\left(\frac{\mu}{Sc} + \frac{\mu_T}{Sc_T}\right)$ of the mixture fraction and mixture fraction variance equations (see Eq. 4–8 and 4–9) to zero for the cells closest to the fuel inlet boundary as illustrated in the figure below. The code used in OpenLabs in order to correct the diffusion coefficient is presented in A Appendix. FINE™/Open with OpenLabs. Solver Settings.

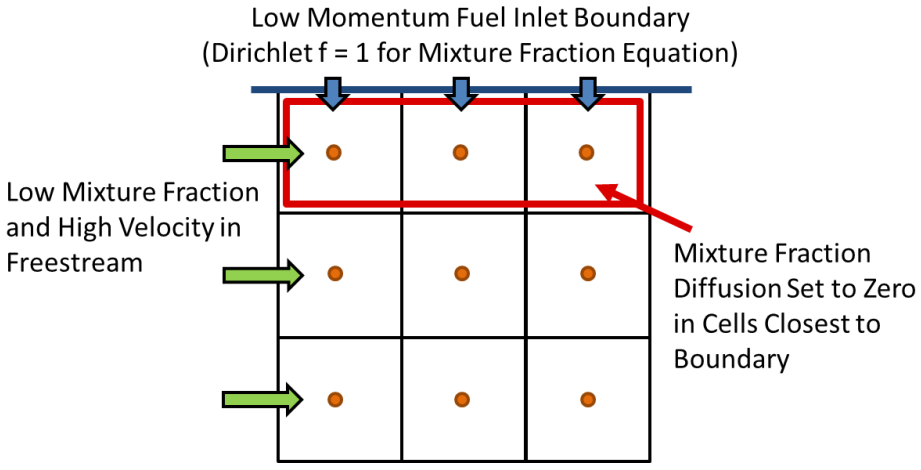

Figure 4–3 Illustration of the method used to correct the inlet diffusion whereby the OpenLabs package in FINE/Open is used to set the mixture fraction diffusion coefficient equal to zero in the cells closest to the fuel inlet boundary

The result allowed the author to prevent the spurious effects of inlet diffusion from affecting the stoichiometry of the combustion simulations. As shown in the Figure 4–4, the global O/F ratio precisely matches that specified by the user.

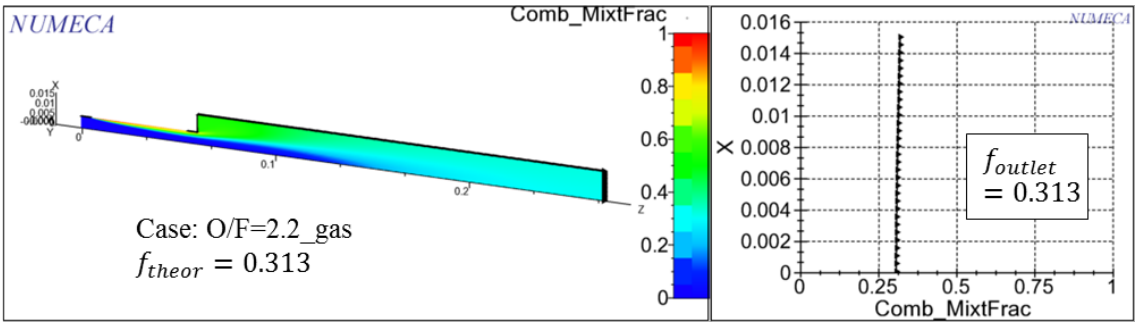

Figure 4–4 Corrected version of the simulation shown in Figure 4–2, with the correct downstream mixture fraction (f=0.313). Case: O/F=2.2_gas.

4.2.5 Chemical kinetics scheme

Chemical kinetics is the study of speed of chemical reactions, and how the rates are influenced by different experimental conditions such as the physical state of the reactants, the concentrations of the reactants, the temperature at which the reaction occurs, and whether or not any catalysts are present in the reaction.

The importance of detailed chemical kinetic mechanisms was emphasized by several research groups [63] [64] [65]. Flame propagation problem has been studied thoroughly over last decades and reliable detailed kinetic mechanisms were developed. For example, there are detailed mechanisms available for alkanes with the carbon number up to C16 developed by C. K. Westbrook el. [66] [67], but no detailed chemical kinetics has been proposed in the literature for high carbon number alkanes, such as $C_{28}H_{58}$.

It should be highlighted that the complexity of the detailed mechanism increases for higher carbon number alkanes. For instance, the oxidation of Hexadecane $C_{16}H_{34}$ is described by 8130 reactions and 2116 species (see Table 4–1) [68]. Therefore, there is a continuing need for reliable models for fuel oxidation which are very simple and yet still reproduce experimental flame propagation phenomena over extended ranges of operating conditions [69] [70].

Table 4–1 Sizes of some of the fuel mechanisms without NOx and soot submodels

	$C_{16}H_{34}$	$C_{14}H_{30}$	$C_{12}H_{26}$
Reactions	8130	6449	5030
Species	2116	1668	1282

Westbrook and Dryer [69] studied one-step and two-steps global oxidation mechanisms for hydrocarbon fuels.

They investigated main combustion products, and reaction rates through an experimental study. The study showed that **TWO-STEPS GLOBAL OXIDATION MECHANISM** predicts more closely the adiabatic flame temperature and CO concentration.

$$C_nH_m + \left(\frac{n}{2} + \frac{m}{4}\right) O_2 = nCO + \frac{m}{2} H_2O$$
$$CO + \frac{1}{2} O_2 = CO_2 \qquad 4–18$$

As the result of the conducted study Westbrook and Dryer determined values of activation energies E_a, pre-exponential coefficients A_K, and concentration exponents for the fuels with carbon number up to C_{10} .

$$K_1 = A_{K1} e^{\frac{-E_{a1}}{RT}} [C_nH_m]^{0.25} [O_2]^{1.5}$$
$$K_2 = A_{K2} e^{\frac{-E_{a2}}{RT}} [CO]^1 [H_2O]^{0.5} [O_2]^{0.25} \qquad 4–19$$

This study cannot be directly applied to the paraffin-wax oxidation problem because it was, first of all, conducted using laminar flames, while hybrid rocket combustion is turbulent. Second, the range of investigated fuels did not include alkanes higher than carbon number C_{10}.

As can be noticed, investigations on the oxidation problem of hydrocarbons are limited to n-alkanes with quite low carbon number, those that remain in gaseous or liquid state at room temperature. The literature review on the use of high carbon number paraffin-waxes revealed that usually such alkanes undergo cracking process in order to obtain more useful alkanes and alkenes. "Cracking" is simply a process of any type of

splitting of molecules under the influence of pressure, heat, and catalysts, such as in process of pyrolysis.

One of the kinds of the thermal cracking operates under conditions of high pressure of about 7 MPa and high temperatures – around 1000-1200K, which is also called pyrolysis. Despite the mild-temperature cracking process (ca. 750K) the high-temperature cracking results in production of mostly ethylene due to the free-radical chain mechanism [71], [72], [73].

Free-radical chain mechanism was first suggested by Rice et al. [74] proposing that pyrolysis occurs through free-radical. Later, Kossiakoff and Rice [75] extended the mechanism (KR theory), which has been widely accepted by many researchers. KR theory has been employed for the product distribution and the reaction rate of hydrocarbons pyrolysis [76], [77], as well as for obtaining both detailed chemical kinetic schemes [78] and reduced schemes [79].

Free-radical chain mechanism reaction consists of three main steps [73]:

1. Initiation reactions: the initial breakage of the molecule into two alkyls due to the fact that C-C bond is weaker than the C-H bond.
2. Propagation reactions: a free radical generates another radical through sequence of recombination reactions. There are three steps of a propagation reaction:
    - Isomerization: an odd electron transfer in an alkyl radical;
    - β-scission: an alkyl radical decomposition and 1-alkenes formation;
    - H abstraction: an odd electron transfer between n-alkane and an alkyl radical;
3. Termination reactions: free radicals finally react in a way that they are removed from the system.

Under conditions of high temperatures (T > 1100K) the decomposition reaction is much faster than the bimolecular reaction, thus β-scission will predominate over the hydrogen abstraction, which means that an alkyl radical would continue to expel C_2H_4 and break down all the way to $C_2H_5\bullet$, $CH_3\bullet$ or $H\bullet$ radicals [71], [80] (Figure 4–5).

High temperature conditions fit the conditions of combustion in a hybrid rocket motor, which makes the free-radical mechanism, described above, be applicable for paraffin-based hybrid rockets.

Modeling assumptions:

1. The main product of pyrolysis – ethylene C_2H_4;
2. Detailed chemical kinetic mechanism is available (GRI-Mech 3.0) [81];
3. The pyrolysis time required for C_2H_4 to be expelled and to be available for combustion is negligible.

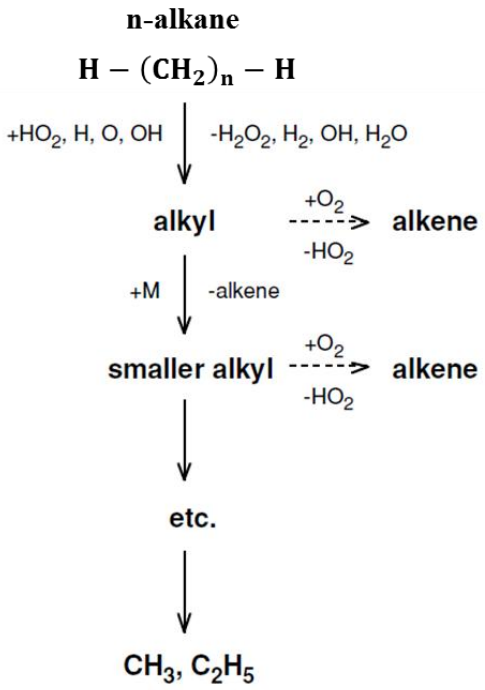

Figure 4–5 Scheme of free-radical chain mechanism suggested for n-alkanes

Table 4–2 Summary of the modeling approaches of $C_{28}H_{58}$ oxidation

Chemical kinetics model	Advantages	Shortcomings
Detailed chemistry	➢ The most precise simulation of the flame propagation and combustion products	➢ Not available ➢ The mechanism would be too complex and would require a lot of computational time
Two-steps global mechanism	➢ Simple and fast	➢ Not available ➢ Available reaction rates could not be applied directly, only by means of extrapolation
Pyrolysis (C_2H_4 as the main product of pyrolysis)	➢ Free-radical mechanism has been proven by many research groups ➢ Detailed chemical kinetics of the oxidation of C_2H_4 are available ➢ Reliable and relatively fast	➢ Does not take into account time required on the thermal decomposition

4.2.6 Spray: Droplet size distribution

Particle or droplet size distributions can be classified as discrete or continuous. The continuous size distribution derives from the discrete distribution as the sampling interval approaches zero [82].

Mugele and Evans [83] formulated the upper-limit equation for droplet size distribution. The upper-limit distribution was obtained from the "normal distribution" function through a correction by an upper-limit. A maximum drop diameter d_{max} was introduced to cut off extremely large drops that have extremely low frequencies.

Volume distribution equation is defined by the system:

$$\frac{d\vartheta}{dy} = \frac{\delta}{\sqrt{\pi}} e^{-\delta^2 y^2} \qquad 4\text{–}20$$

$$y = \ln \frac{ad}{d_{max} - d} \qquad 4\text{–}21$$

where y is dimensionless function of droplet diameter; δ is size distribution parameter; and a is a constant in upper-limit equation.

Studies of droplet sizes have been performed by many researchers [84], [85], [86], [87], [88]. There are two correlations that may find application to the hybrid rocket combustion process: obtained by Tatterson et al. [86] and Kataoka, Ishii, and Mishima [88].

Kuo and Houim [89] analyzed those two correlations, and suggested mechanistic model developed by Kataoka, Ishii, and Mishima [88] as the most fitting for hybrid rocket propulsion. Their model was based on the potential flow assumption employed in the standard Weber number criterion was eliminated in developing the mechanistic model. By collaborating the mechanistic model with experimental data, Kataoka, Ishii, and Mishima derived a correlation for the volume median diameter in the form where $We_{d_{vm}}$ is the characteristic Weber number. Their correlation is:

$$We_{d_{vm}} = 0.028 Re_l^{-\frac{1}{6}} Re_g^{\frac{2}{3}} \left(\frac{\rho_g}{\rho_l}\right)^{-\frac{1}{3}} \left(\frac{\mu_g}{\mu_l}\right)^{\frac{2}{3}} \qquad 4\text{–}22$$

where the gas and liquid Reynolds number and the characteristic Weber number are defined respectively by

$$Re_g = \frac{\rho_g j_g \, d_h}{\mu_g} \tag{4–23}$$

$$Re_l = \frac{\rho_l j_l \, d_h}{\mu_l} \tag{4–24}$$

$$We_{d_{vm}} = \frac{\rho_g j_g^2 d_{vm}}{\sigma_l} \tag{4–25}$$

where j_g is the superficial velocity of the gaseous component of the spray system, j_l is the superficial velocity of the total liquid (in case of hybrid fuel grain, the superficial velocity consider both the liquid film above the solid fuel surface and the liquid fuel droplet in the gas core), d_h is hydraulic diameter of the fuel port for the mixture of gas and particles to flow through, and σ_l is surface tension between gaseous and liquid components.

Tatterson et al. [86] employed a log normal function to simulate the droplet size distribution for a thin film flow. The correlation was based largely on the Kelvin-Helmholtz instability at the top of a liquid film and ligament in an inviscid flow. They presented a correlation in the form

$$We_{d_{vm}} = 0.106 Re_g^{1.1} \left(\frac{\mu_g^2}{d_h \sigma_l \rho_g} \right)^{\frac{1}{2}} \tag{4–26}$$

where the gas Reynolds number and the characteristic Weber number are defined respectively by Eq. 4–23 and 4–25.

Based on experimental results, Kuo [89] suggested that values of δ and a were found to be $\delta = 0.884$ and $a = 2.13$ whereas using the upper limit log-normal distribution, the maximum diameter was related to the volume median diameter by:

$$d_{max} = 3.13 d_{vm} \tag{4–27}$$

Thereby, from the above expressions 4–20, 4–21 the droplet size distribution can be correlated using the following equations:

$$\frac{d\vartheta}{dy} = \frac{0.884}{\sqrt{\pi}} e^{-0.781y^2} \qquad 4\text{–}28$$

$$y = \ln \frac{2.13d}{3.13d_{vm} - d} \qquad 4\text{–}29$$

Once the volume median diameter is known (Eq. 4–25, 4–26), combining with the expressions of upper-limit log normal distribution, the spray can be uniquely determined by the above expressions 4–28, 4–29.

Volume median diameter derived by Tetterson et al. has been chosen for this research thesis. The reasons are:

1) The two models (Kataoka, Ishii, and Mishima, and Tatterson et al.) have been never tested on a material such as molten paraffin. They've been tested on gas-liquid systems like air-water using a constant velocity of the liquid phase supply, and never for a melting material [90], [91]. Thus, it's hard to be confident that either of them would give precise value of the volume median diameter.
2) Another issue is that it's not clear how to specify superficial liquid velocity j_l (see Eq. 4–24, 4–22) present in Kataoka, Ishii, and Mishima model. The initial liquid velocity is extremely low, or even equal to 0 m/s. From this prospective the correlation developed by Tatterson seems to be more feasible to be applied for liquefying hybrid rocket fuel.
3) The theory developed by Tatterson et al. is based largely on the KH instability, which fits the explanation of entrainment process in liquefying hybrid fuels, when the fuel mass burning rates under high cross-flow conditions are dominated by the KH instabilities behavior [92].

4.3 Main models and solver settings

To summarize, the simulation was built inside the FINE/Open v.4.1 software with some modifications to the diffusion of the mixture fraction through the OpenLabs package. The simulation consists of a steady-state turbulent flow field with combustion. The combustion physics were treated with a non-premixed flamelet model with lagrangian particle transport coupled via source terms to the eulerian transport

equations. The chemical kinetics used for calculating the flamelet tables assumed specific mechanisms of pyrolysis and gas-phase reactions.

Table 4–3 Summary of main models used for numerical parametric study

Flow Solver	FINE/Open v.4.1 with OpenLabs
Gaseous reacting flow (combustion)	Steady RANS + Mixture fraction approach
Turbulence model	k-epsilon (Standard)
Turbulent Chemistry	Flamelet
Chemical kinetics	Pyrolysis + detailed chemistry
Dispersed liquid phase	Lagrangian
Droplet size distribution of the liquid phase	Upper-limit log normal distribution

From the models described in the preceding sections, we have a system of 9 coupled partial differential equations (4–30) – (4–36), shown below which govern the behavior of the combustion simulation in the lagrangian framework. These equations must be solved simultaneously while also taking into account their interactions with the Lagrangian particles. The initial solution and boundary conditions for the system of equations (4–30) – (4–36) are described in details in Chapter 5.2 “Initial solution, and Boundary conditions”.

$$\frac{\partial}{\partial x_i}(\rho u_i) = S_{evap} \qquad 4\text{–}30$$

$$\frac{\partial}{\partial x_j}\left(\rho u_i u_j\right) + \frac{\partial P}{\partial x_i} = \frac{\partial}{\partial x_j}\left[(\mu + \mu_T)\frac{\partial u}{\partial x_j}\right] + S_{Drag} \qquad 4\text{–}31$$

$$\frac{\partial}{\partial x_j}(\rho u_i h) = \frac{\partial}{\partial x_j}\left[(k + k_T)\frac{\partial T}{\partial x_j}\right] + S_{reaction} \qquad 4\text{–}32$$

$$\frac{\partial}{\partial x_j}(u_i \rho k) = \frac{\partial}{\partial x_j}\left[\left(\mu + \frac{\mu_T}{Pr_T}\right)\frac{\partial k}{\partial x_j}\right] - \rho\epsilon + S_k \qquad 4\text{–}33$$

$$\frac{\partial}{\partial x_j}(u_i \rho \epsilon) = \frac{\partial}{\partial x_j}\left[\left(\mu + \frac{\mu_T}{Pr_T}\right)\frac{\partial \epsilon}{\partial x_j}\right] + 1.44 S_k \frac{\epsilon}{k} - 1.92\,\rho\frac{\epsilon^2}{k} \qquad 4\text{–}34$$

$$\frac{\partial}{\partial x_j}(\rho u_i f) = \frac{\partial}{\partial x_j}\left[\left(D_f + \frac{\mu_T}{Sc_T}\right)\frac{\partial f}{\partial x_j}\right] + S_{evap} \qquad 4\text{–}35$$

$$\frac{\partial}{\partial x_j}(\rho u_i f'^2) = \frac{\partial}{\partial x_j}\left[\left(D_f + \frac{\mu_T}{Sc_T}\right)\frac{\partial f'^2}{\partial x_j}\right] + 2.85(\nabla f)^2 - 2\rho\frac{\varepsilon}{k} f'^2 \qquad 4\text{–}36$$

5 COMPUTATIONAL INVESTIGATION: RESULTS AND DISCUSSION

The preliminary design problem typically posed is to determine the approximate size of a hybrid rocket motor, given numerous system requirements and design assumptions. One of the key characteristics is characteristic velocity, c*, that is commonly used for combustion chamber performance evaluation and comparison between different fuel/oxidizer couples. Theoretical c* values are typically degraded to account for combustion inefficiency due to incomplete oxidizer/fuel mixing. For example, the combustion efficiency for conventional HTPB-based fuels is assumed to be around 95% of the theoretical value [93].

In hybrid rocket motors utilizing paraffin-based fuels due to the melting of paraffin, and entrainment effect (see Chapter 2.1.2), the internal physics are described as multiphase flow combustion for which the effect on c* and combustion efficiency is not well characterized for use in preliminary design studies.

The combustion of a liquid fuel spray is either a simultaneous or sequential complex process involving fluid dynamics of liquid and gas, heat and mass transfer, and chemical reactions [94]. The detailed flame zone structure of a fuel spray during combustion may be studied by numerical simulation, which is based on the analysis of liquid mass transfer and drop evaporation.

The numerical investigation was performed by means of the CFD software "FINE/Open v.4.1 with OpenLabs" developed by NUMECA Int., Brussels.

The simulation consists of a steady-state turbulent flow field with turbulent combustion and evaporating Lagrangian particles which are simulated on a two-dimensional axi-symmetric computational domain (see Chapter 5.1 "Computational domain and Mesh"). The combustion physics were treated with a non-premixed flamelet model with lagrangian particle transport coupled via source terms to the eulerian transport equations. The chemical kinetics used for calculating the flamelet tables assumes specific mechanisms of pyrolysis and gas-phase reactions (see Chapter 4.2.5 "Chemical kinetics scheme"). For details on the numerical model development see Chapter 4 "Paraffin-based Fuels: Numerical Model Development". For detailed solver settings see A Appendix. FINE^{TM}/Open with OpenLabs. Solver Settings.

Efficiency of spray combustion, and evaporation are investigated by means of computational simulations. Combustion chamber performance is estimated using characteristic velocity parameter c*. The simulated cases are compared to each other in terms of mixture ratio O/F, and characteristic velocity. Also, the characteristic velocities c* of the simulated spray combustion cases obtained by CFD are confronted to the theoretical values of c* obtained by NASA "Chemical Equilibrium with Applications" software (NASA CEA) [95], [96], [97].

5.1 Computational domain and Mesh

The computational domain used for all of the simulations shown here is a cylindrical geometry. The combustion chamber of the experimental rig at SPLab was used as a prototype for the domain dimensions. Fuel length and diameter (50mm and ∅12mm) correspond to tested fuel samples, where the diameter is an average between initial (∅8mm) and final (∅16mm) diameters during a burning test. The length of the aft-combustion chamber (240mm) was chosen in order to satisfy the computational requirements of a fully developed turbulent flow (entrance length). The entry length in turbulent flows is much shorter as compared to laminar one, and is considered to be enough when [98]:

$$L_{h,turbulent} = 1.359D(Re)^{1/4} \qquad 5\text{–}1$$

In most of the practical engineering applications, this entrance effect becomes insignificant beyond a pipe length of 10 times the diameter and hence it is approximated to be:

$$L_{h,turbulent} \approx 10D \qquad 5\text{–}2$$

Thus, considering bigger diameter of the domain, ∅30mm, the length is (see Figure 5–1).

$$L_{h,turbulent} \approx 10 * 30 = 300mm \qquad 5\text{–}3$$

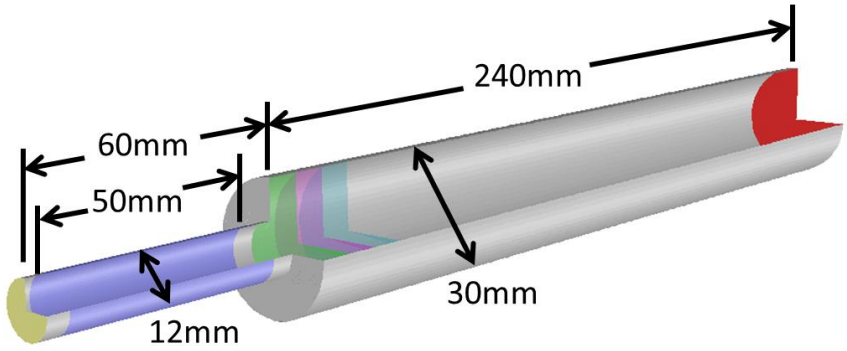

Figure 5–1 Computational domain dimensions

The oxidizer enters the domain axially through the inlet. The fuel inlet is represented by the cylinder surface, and the fuel flows radially (see Figure 5–2). Since for a number of simulations the fuel is a mixture of gaseous and liquid phase, both phases are injected through the fuel inlet.

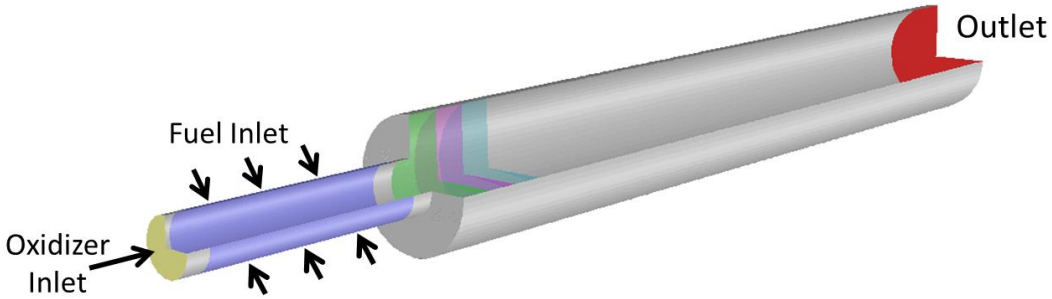

Figure 5–2 Inlets and outlets location

In order to save computational time, the cylindrical domain is represented as a two-dimensional axisymmetric segment of 5°deg (1 cell), and periodic boundary condition is used for the side walls, Full Non Matching connections (FNMB). The mesh consists of 21500 cells, and has two refinement boxes, one of which covers the region of flame, and the finer box is attached to the fuel inlet. The refinement on the inlet of fuel was motivated by the Inlet diffusion problem and applied solution to the problem described in the Chapter 4.2.4 (for details see also B Appendix. Inlet Diffusion Problem) in order to minimize the region of the domain in which the treatment was applied.

Y+ max is 6.33, which is still within the laminar sublayer and, since the vast majority of the wall surface has Y+ substantially lower than the maximum value, less than 1 in most cases, the turbulence model's wall resolution requirements are considered adequately met by this level of mesh resolution.

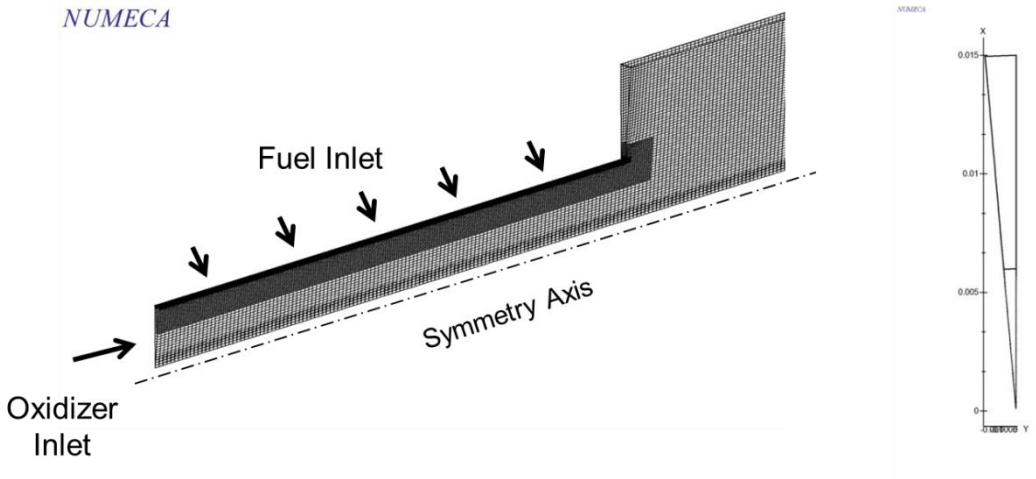

Figure 5–3 Mesh of the simulated geometry

5.2 Initial solution, and Boundary conditions

The solver works in an iterative manner. Therefore before the very first iteration, a value must exist for every quantity in every grid cell. All simulations use the same set of values for initialization, and they are summarized in the Table 5–1.

Table 5–1 Initial conditions

Pressure	4 bar
Axial velocity (oxidizer), Vz	1 m/s
k	0.275 m2/s2
Epsilon	28.64 m2/s3
Mixture fraction	0

While the set of differential equations is the same for all computational cases, what make each case be unique are boundary conditions. The boundary conditions dictate the particular solutions to be obtained from the governing equations. The boundary conditions common for all simulations are shown in the Table 5–2.

The following **assumptions** were made:

a) The fuel stream is laminar on the inlet. In reality the fuel surface pyrolyzes, and the gaseous fuel enters the combustion chamber with a very low speed;
b) Gaseous fuel temperature assumed to be the temperature at which paraffin starts pyrolyzing;
c) It's not clear when exactly the entrainment of melted paraffin happens. Thus, liquid droplet temperature is calculated as average between the melting temperature and the temperature of pyrolysis. Melting temperature was obtained experimentally (see Chapter 3.2.1);

$$T_{liquid} = T_{melting} + \frac{T_{boiling} - T_{melting}}{2} = 330 + \frac{700 - 330}{2} = 515°K \qquad 5–4$$

d) The heat transfer to the walls is not taken into consideration, so the walls are treated as adiabatic.

Table 5–2 Boundary conditions

	Turbulence intensity	**Temperature, [K]**	**Mixture fraction**
Inlet Oxidizer	5%	298	0
Inlet Fuel (gas)	No turbulence	700	1
Liquid Fuel	No turbulence	515	1
Outlet	-	-	-
Walls	-	adiabatic	-

The current computational study was carried out considering two main effects on the combustion

- operating conditions in terms of oxidizer to fuel ratio (O/F),
- and fraction of liquid phase of fuel.

Four values of the mixture ratio (O/F) - 1.5, 2.2, 3.42, and 4.5 - represent operating conditions of a hybrid rocket motor. The overall mixture ratio during the burn displays a time variation due to the increase on the port size. The increase in port cross section increases the fuel burning surface area but decreases the fuel regression rate. These two effects are in general not balanced, leading to a change (usually a decrease) in the overall fuel production rate [51]. Thereby O/F range represents the shift of the mixture ratio, from rich to lean reacting mixtures. O/F=2.2 corresponds to the highest

vacuum specific impulse Isp and characteristic velocity c* for propellant combination "paraffin+LOx", and O/F=3.42, instead, is a stoichiometric mixture (equivalence ratio = 1) according to thermodynamic calculations by means of NASA CEA software [99].

The choice of liquid fuel fraction (0-30-60%) of the total fuel mass flow, that represents entrained paraffin, was motivated, by the liquid layer theory developed by Karabeyoglu on combustion of liquefying hybrid propellants [5]. The model shows clear dependency of entrainment regression rate on the total propellant mass flux G_{tot}. On the one hand, as the Figure 5–4 shows, the fraction of liquid phase of the fuel (entrained) is decreasing when the total mass flux is decreasing. On the other hand, it's well known that over the burning time the total mass flux in hybrid rocket motors decreases due to the increase in port cross section that results in the fuel regression rate decrease, and thus the total mass flux decrease [100].

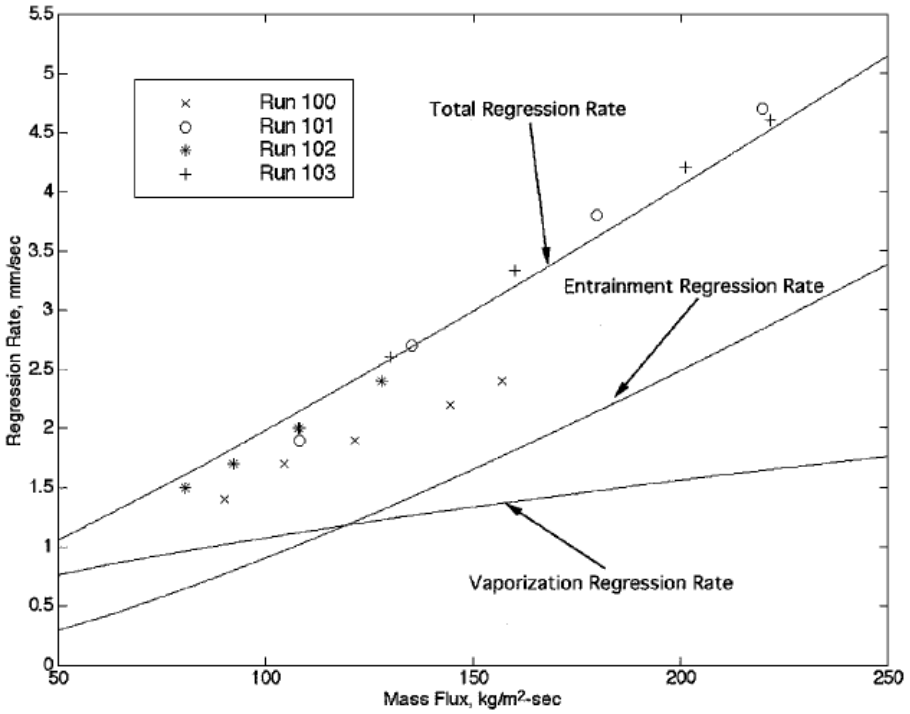

Figure 5–4 Liquid layer theory predictions for the vaporization, entrainment, total regression rates, and corresponding mass fluxes for four different pentane tests (Karabeyoglu).

So, O/F 1.5-2.2-3.42-4.5 and 60-30-0% of liquid fraction represent the propellant mixture in a hybrid rocket motor over the burning time.

The oxidizer mass flow was fixed

$$\dot{m}_{oxidizer} = 0.005456\ kg/s$$

The Table 5–3 shows inputs of mass flow rates according to O/F and liquid fuel fraction.

Table 5–3 Fuel mass flow rate inputs

# simulation	O/F	% spray	$\dot{m}_{fuel}$ [kg/s]	$\dot{m}_{gas}$ [kg/s]	$\dot{m}_{liquid}$ [kg/s]
1	1.5	0	0.003637	0.003637	0.0
2		30	0.003637	0.002546	0.001091
3		60	0.003637	0.001455	0.002182
4	2.2	0	0.002480	0.002480	0.0
5		30	0.002480	0.001736	0.000744
6		60	0.002480	0.000992	0.001488
7	3.42	0	0.001595	0.001595	0.0
8		30	0.001595	0.001117	0.000479
9		60	0.001595	0.000638	0.000957
10	4.5	0	0.001212	0.001212	0.0
11		30	0.001212	0.000849	0.000364
12		60	0.001212	0.000485	0.000727

In order to describe entrained liquid paraffin a spray of 6 classes of droplets was employed (see Chapter 4.2.6). The main assumption is that the median diameter of spray is a function of *initial* shear gas flow (oxidizer) velocity (see Eq. 4–26). Based on the boundaries described before, the geometry and the oxidizer mass flow are fixed, which means that the 6 class diameters are independent on liquid mass flow, and so remain the same for each simulation. The probability density function (PDF) and cumulative distribution function (CDF) are shown in Figure 5–5 and Figure 5–6 respectively. The values of 6 class diameters and corresponding mass flow fractions are shown in the Table 5.2–4. Each simulation uses unique set of mass flow values for spray definition (see Table 5–5).

$$O/F = \frac{\dot{m}_{oxidizer}}{\dot{m}_{fuel}} \qquad 5–5$$

$$\dot{m}_{oxidizer} = const$$

$$\dot{m}_{fuel} = \dot{m}_{gas} + \dot{m}_{liquid} \qquad 5–6$$

$$\dot{m}_{liquid} = \sum \left(\dot{m}_{spray\_class}\right)_i \qquad 5\text{–}7$$

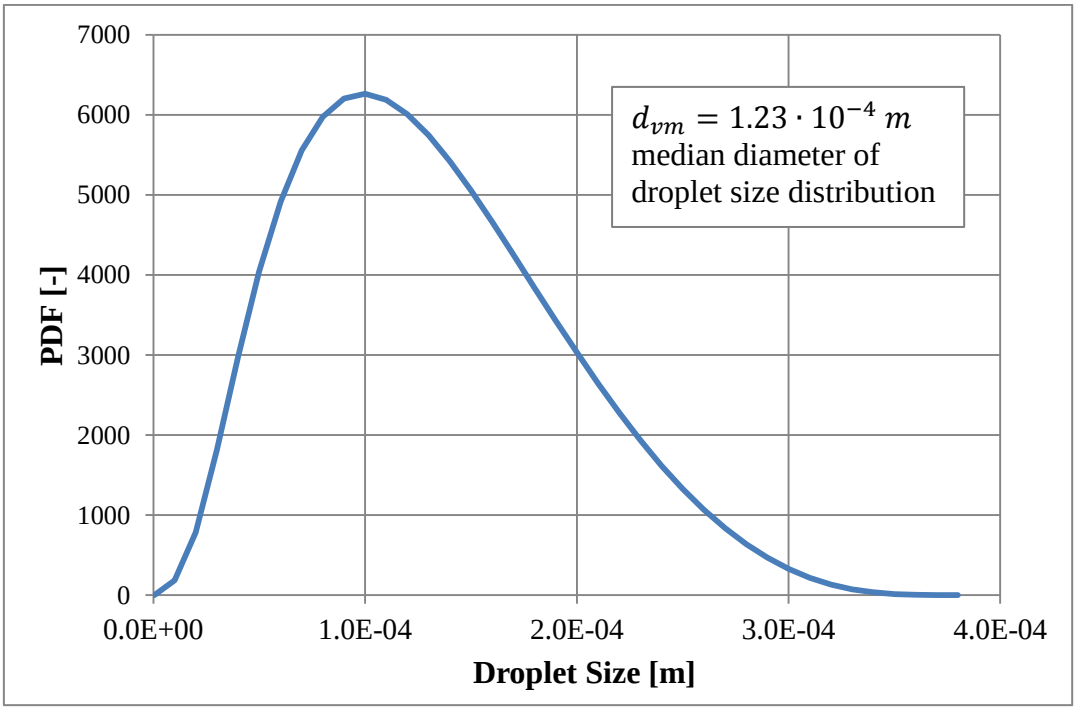

Figure 5–5 Probability density function (PDF)

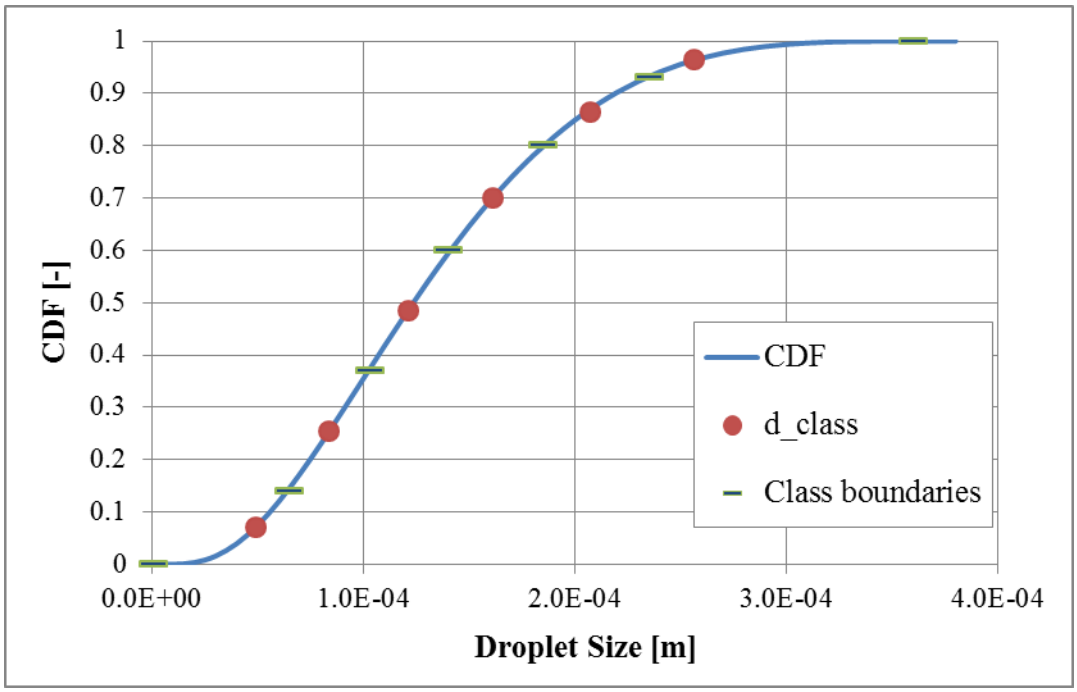

Figure 5–6 Cumulative distribution function (CDF). The boundaries of six classes used for spray definition and average diameters of each class are plotted as well.

Table 5–4 Liquid phase boundary conditions. Mass flow fraction and diameter.

# class	Mass flow fraction	Diameter, [m]
1	0.14	3.744e-5
2	0.23	7.551e-5
3	0.23	1.203e-4
4	0.2	1.709e-4
5	0.13	2.263e-4
6	0.07	2.866e-4

Table 5–5 Mass flow inputs (Liquid phase) per each class for each simulation.

# simulation	O/F	% spray	$\dot{m}_{liquid}$ [kg/s]					
			Class #1	Class #2	Class #3	Class #4	Class #5	Class #6
1	1.5	0	0.0	0.0	0.0	0.0	0.0	0.0
2		30	1.528e-4	2.51e-4	2.51e-4	2.182e-4	1.419e-4	7.638e-5
3		60	3.055e-4	5.02e-4	5.02e-4	4.365e-4	2.837e-4	1.528e-4
4	2.2	0	0.0	0.0	0.0	0.0	0.0	0.0
5		30	1.042e-4	1.711e-4	1.711e-4	1.488e-4	9.672e-5	5.208e-5
6		60	2.083e-4	3.422e-4	3.422e-4	2.976e-4	1.934e-4	1.042e-4
7	3.42	0	0.0	0.0	0.0	0.0	0.0	0.0
8		30	6.7e-5	1.101e-4	1.101e-4	9.572e-5	6.222e-5	3.35e-5
9		60	1.34e-4	2.202e-4	2.202e-4	1.914e-4	1.244e-4	6.7e-5
10	4.5	0	0.0	0.0	0.0	0.0	0.0	0.0
11		30	5.092e-5	8.366e-5	8.366e-5	7.275e-5	4.729e-5	2.546e-5
12		60	1.018e-4	1.673e-4	1.673e-4	1.455e-4	9.457e-5	5.092e-5

Liquid droplet temperature is assumed to an arithmetic average between the melting temperature and the temperature of pyrolysis. Melting temperature was obtained experimentally (see Chapter 3.2.1). Other liquid phase properties required by the solver are listed in the Table 5–6.

$$T_{liquid} = T_{melting} + \frac{T_{boiling} - T_{melting}}{2} = 330 + \frac{700 - 330}{2} = 515°K \qquad 5–4$$

Table 5–6 Liquid paraffin thermophysical properties.

Melting temperature, $T_{melting}$	330 K
Boiling temperature, $T_{boiling}$ [101] [102]	700 K
Critical temperature, $T_{critical}$	780 K
Molecular weight, M_w [101]	0.4 kg/mol
Latent heat of evaporation, ΔH_{evap}	150 kJ/kg
Specific heat – liquid phase, C_p	2900 J/kg-K
Density – liquid phase, ρ_l	700 kg/m3
Viscosity – liquid phase μ_l [5]	$6.5 \cdot 10^{-4}$ Pa·s
Surface tension σ_l [5]	$7.1 \cdot 10^{-3}$ N/m

Due to the fact that the fuel inlet is 50mm long (see Figure 5–1, Figure 5–2), and initial velocity of the droplets is very small (0.1 m/s), some percentage of liquid mass flow is lost through the fuel inlet. For this reason correction of the input liquid mass flows was done, which means the liquid mass flows describing 6 classes of spray are higher than the calculated ones, because the losses were taken in to account. Please note that all the values of liquid mass flows that are reported in this chapter do not consider liquid lost through the fuel inlet. For the correction procedure and values actually used as the boundary conditions, please, refer to C Appendix. Correction of the Liquid Fuel Mass Flow Losses.

5.3 Solution Convergence

Care was taken to ensure that the solution was sufficiently converged to ensure that the solutions to the discretized governing equations had been reached and that the changes in the solutions from one iteration to the next were sufficiently small that no further iterations were necessary. There are no universal metrics for judging convergence. Residual definitions that are useful for one class of problem are sometimes misleading for other classes of problems. In most cases it's sufficient to reach the decrease in residuals to 10^{-3} for all equations except the energy and P-1 equations, for which the criterion is 10^{-6}. Although, it is possible that if the initial guess is very bad, the initial residuals are so large that a three-order drop in residual does not guarantee convergence. This is specially true for k and epsilon equations where good initial guesses are difficult [103], [61].

The multigrid method was used to accelerate the convergence. The multigrid process starts on a coarse grid, carries out a number of cycles, and then transfers the solution to a finer grid, where the multigrid cycles are performed again. The procedure is successfully repeated until the finest grid is reached [104]. Four grids were used with 1000 cycles per grid level, and the convergence criteria "-5.5"; 8000 cycles for the

finest grid, and the convergence criteria "-6". A personal laptop was used for the simulations with the following performance characteristics:

- 6 Gb RAM
- Intel® Core ™ i3-2330M CPU @ 2.2GHz

The time required to reach 11000 iterations of gaseous solution of the simulation was around 10 hours (in serial mode). About the same time (10-11 hours) was taking multiphase coupled simulation (22 Lagrangian cycles and 6600 Eulerian iterations), which means 20-22 hours for a full spray combustion simulation. (see A Appendix. FINE^{TM}/Open with OpenLabs. Solver Settings).

The Figure 5–7 shows a typical residuals history during a simulation. As can be seen there are four grids. According to the settings first three grids last for 1000 cycles, and the finest grid – 8000 cycles, thus the simulation overall reaches good convergence in 11000 cycles. All residuals are steadily decreasing. The density residual (rms_d b1) drops down to "-5.58", although it undergoes some instabilities, which are acceptable for a reacting flow simulation.

The Figure 5–8 shows typical mixture fraction convergence. Mixture fraction is one of the most important characteristics of a combustion simulation, and has to be monitored.

Another way to evaluate the flow field convergence is mass flow error between inlet and outlet. As shown on the Figure 5–9 the error is very low (0,006%), which can be treated as a very good convergence.

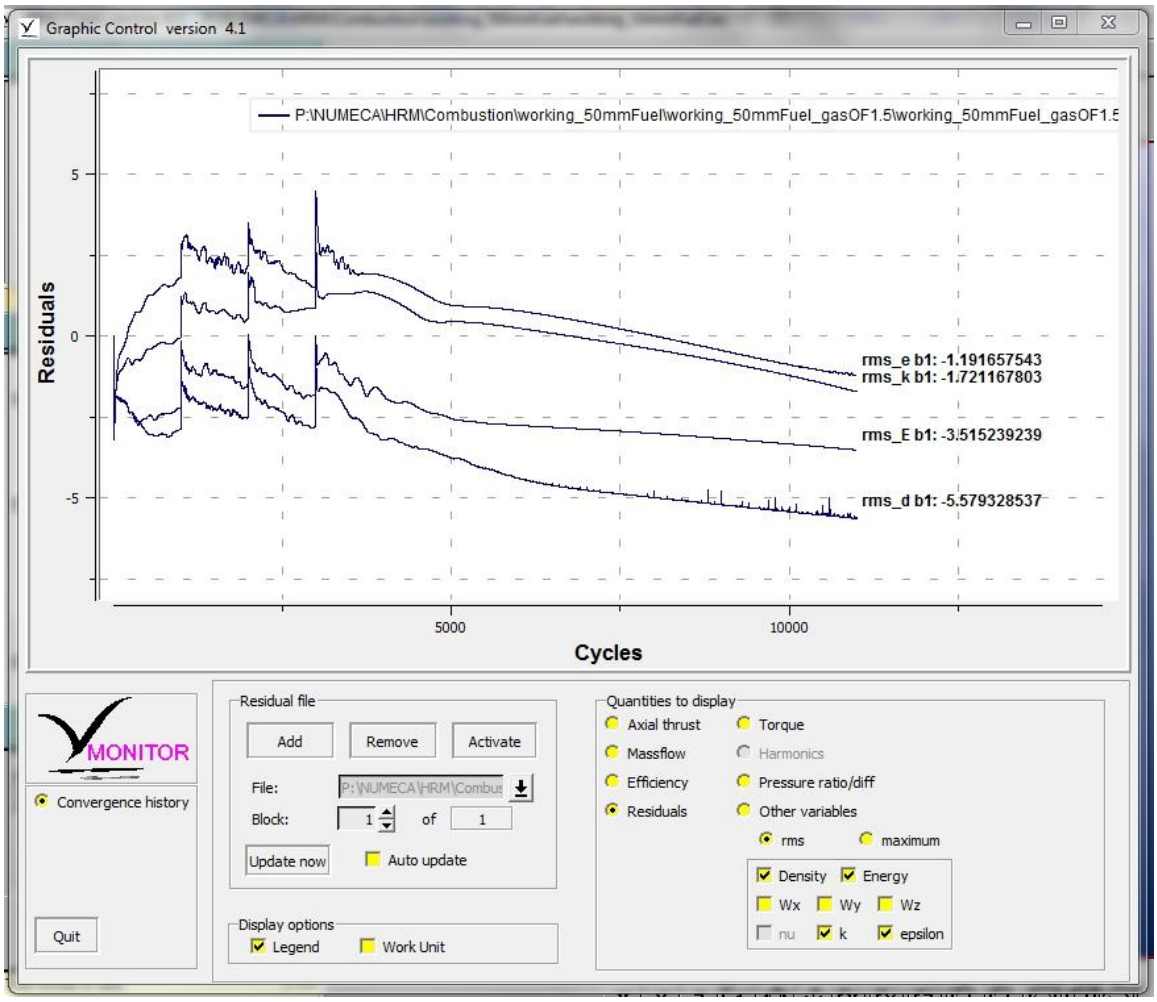

Figure 5–7 Typical convergence of gaseous combustion: epsilon (rms_e b1), k (rms_k b1), energy (rms_E b1), and density (rms_d b1). Case: O/F1.5+spray0%

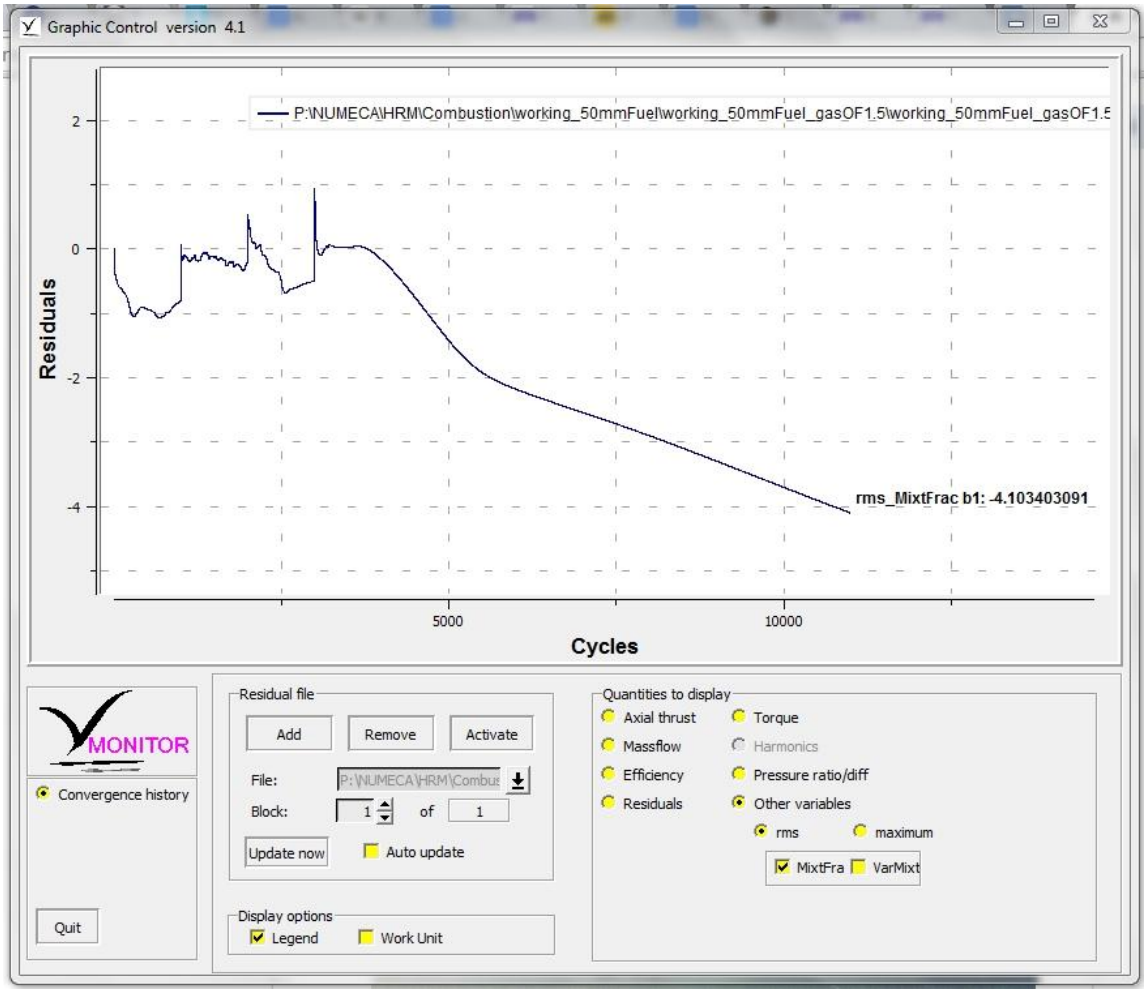

Figure 5–8 Typical convergence of gaseous combustion: Mixture fraction residual track. Case: O/F1.5+spray0%

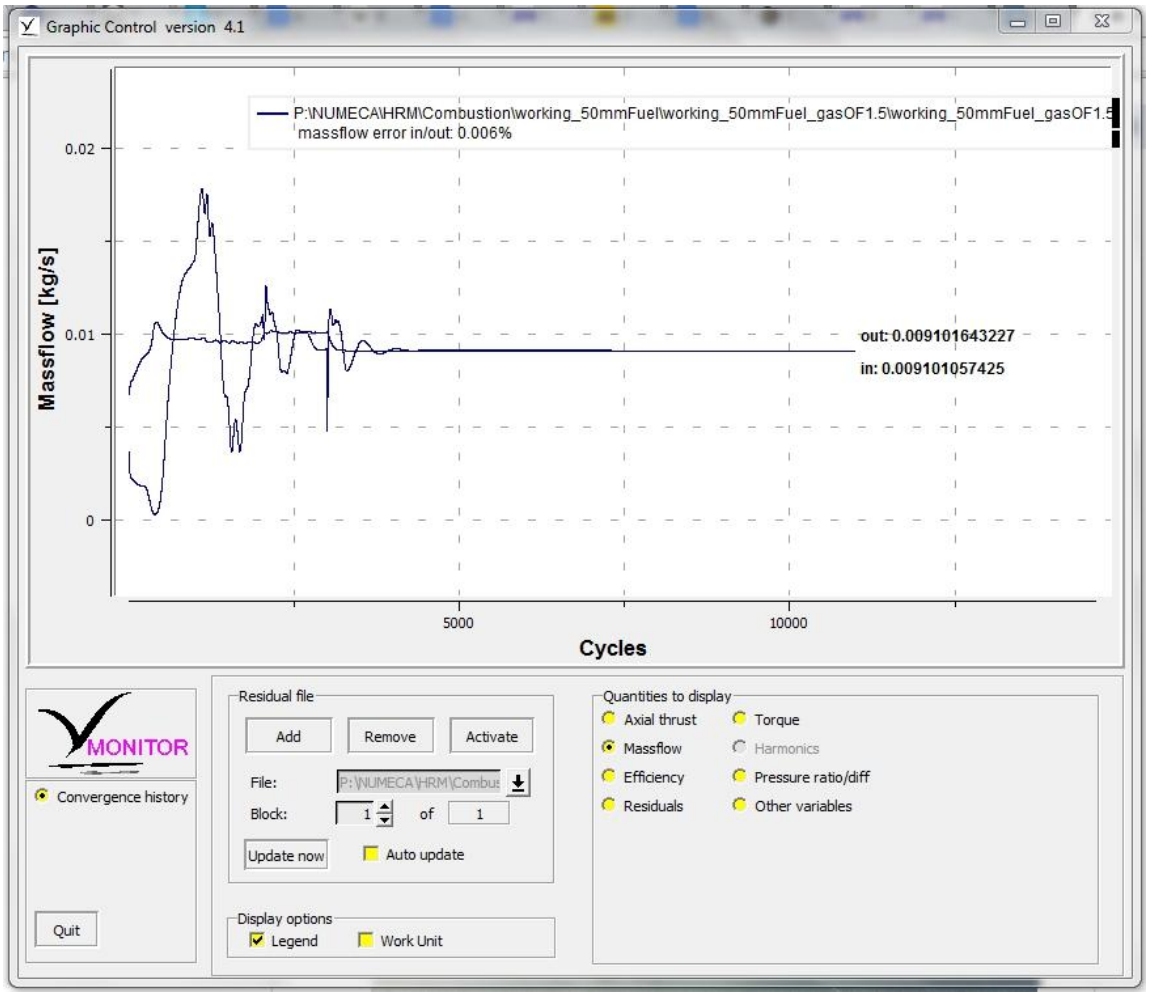

Figure 5–9 Typical convergence of gaseous combustion: Mass flow error inlet/outlet. Case: O/F1.5+spray0%

As it was described at Chapter 4.2.3 “Spray combustion. Coupling of Eulerian and Lagrangian”, a spray combustion solution (when two-ways coupling is used) is obtained in iterative process (cycles) when Eulerian solver receives new sources terms after Lagrangian simulation converged. Unfortunately, no clear convergence criterion exists for dispersed two-phase flows, as it does for the continuous phase. Nevertheless, in order to estimate the quality of Lagrangian simulations the following conditions were satisfied for all performed simulations:

- The stop criterion: all particles left domain;
- Mass influx and mass outflux correspond to each other with very low error;
- Evaporation rate stabilization (see Figure 5–10).

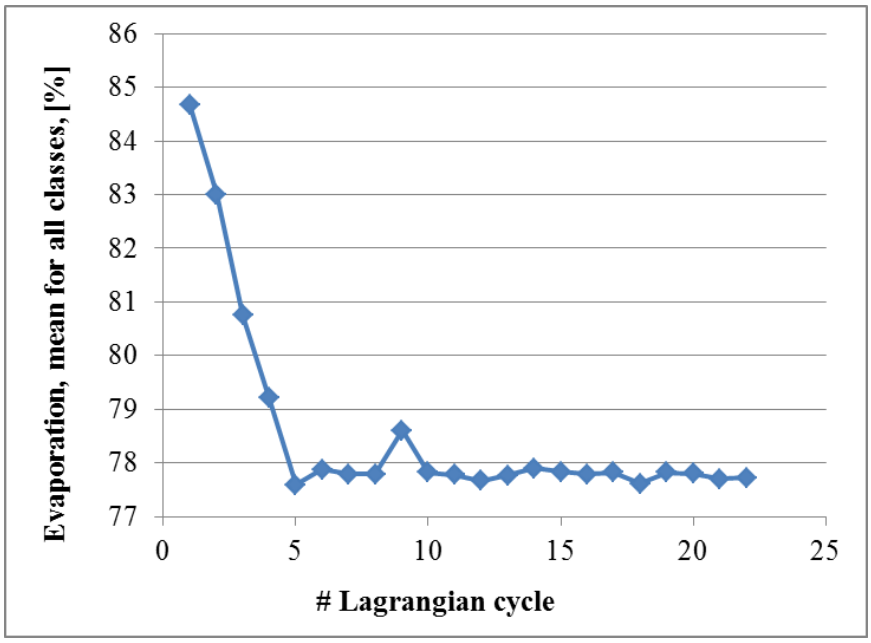

Figure 5–10 Lagrangian solver convergence in terms of evaporation rate. Case: O/F2.2+spray60%

For all spray combustion simulations 22 cycles of Eulerian+Lagrangian were used with 300 iterations for each Eulerian step, so each spray combustion simulation took 6600 Eulerian cycles in total.

On the Figure 5–11 the start of Eulerian solver after each Lagrangian cycle can be clearly seen as jumps in residuals because of new source terms created by evaporated liquid phase. As evaporation rate stabilizes the jumps become more regular in pattern. The residuals of each Eulerian part are decreasing and are reaching "-4.31" for density, and "-1.75" for mixture fraction (see Figure 5–12). The mass flow through the outlet converges to a constant value different from the inlet mass flow, and well corresponds to the evaporated mass flow (see Figure 5–13).

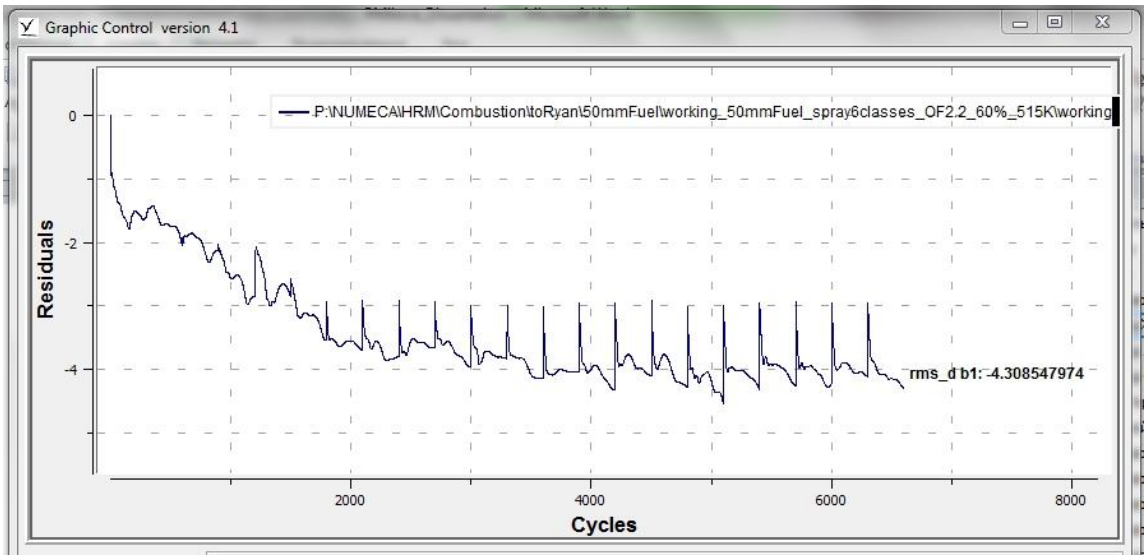

Figure 5–11 Eulerian solver convergence of a spray combustion simulation: Density residuals. Case: O/F2.2+spray60%

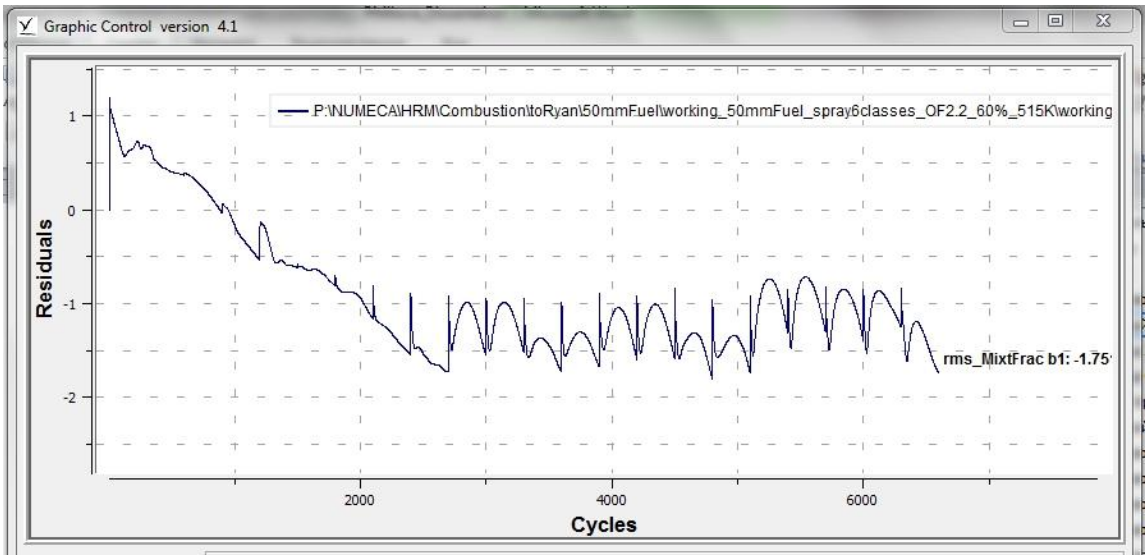

Figure 5–12 Eulerian solver convergence of a spray combustion simulation: Mixture fraction residuals. Case: O/F2.2+spray60%

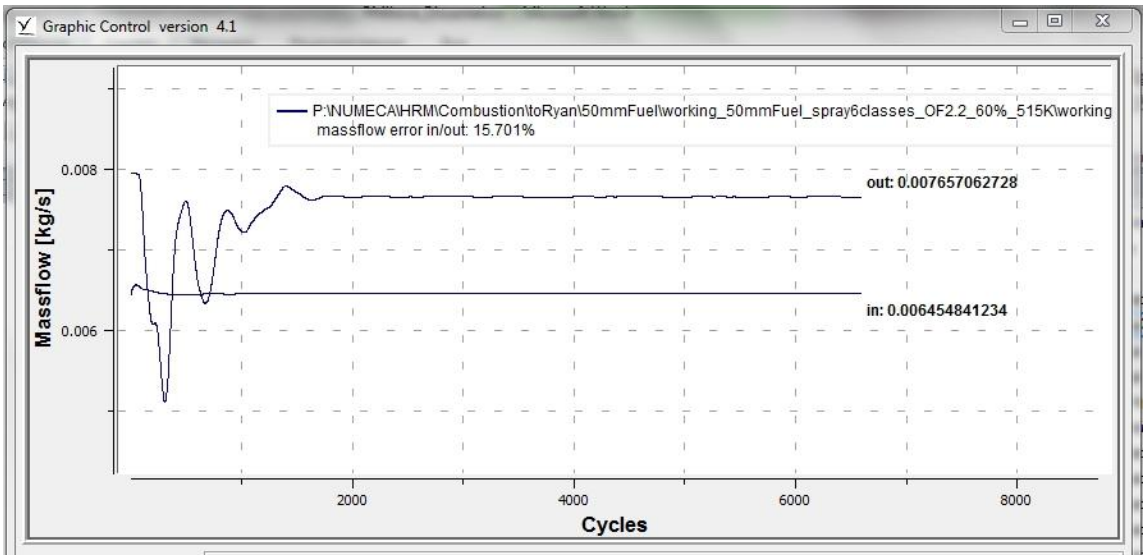

Figure 5–13 Eulerian solver convergence of a spray combustion simulation: Mass flow error inlet/outlet. Case: O/F2.2+spray60%

5.4 Results and Discussion

5.4.1 Spray combustion study

Spray combustion efficiency is characterized by completeness of evaporation and by the trajectories of the droplets which governs where the evaporated fuel mass first mixes with the gas-phase oxidizer. Both of these effects are strongly dependent on the size distributions of the fuel droplets.

On Figure 5–14 the evaporation is represented by color maps of Sauter mean diameter evolution over the length of the domain: from the smallest class of droplets to bigger ones. The initial diameter of class droplets significantly affects evaporation rate. Bigger diameter droplets require more energy and time to be evaporated.

As can be seen on Figure 5–15 the higher velocities increase residence length of droplets. Liquid mass is transported further along the domain which means that evaporation happens further downstream rather than within combustion or post combustion chamber. Note that for higher flow field velocity (Figure 5–15, on the left) particles of the smallest class #1 are transported almost till 0.133 m of the domain, while when the velocity is 10 m/s lower (on the right), the particles reach 0.117 m only.

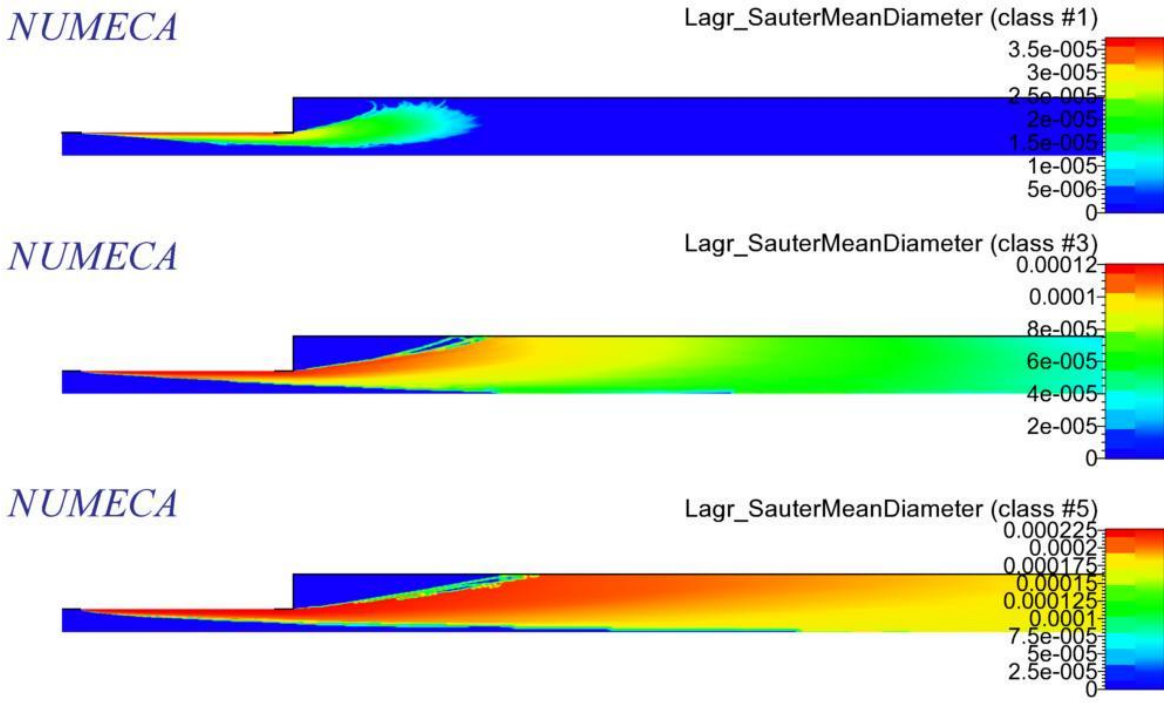

Figure 5–14 Evaporation in action. Sauter mean diameter evolution over the domain length. Case: O/F3.42+spray30%.

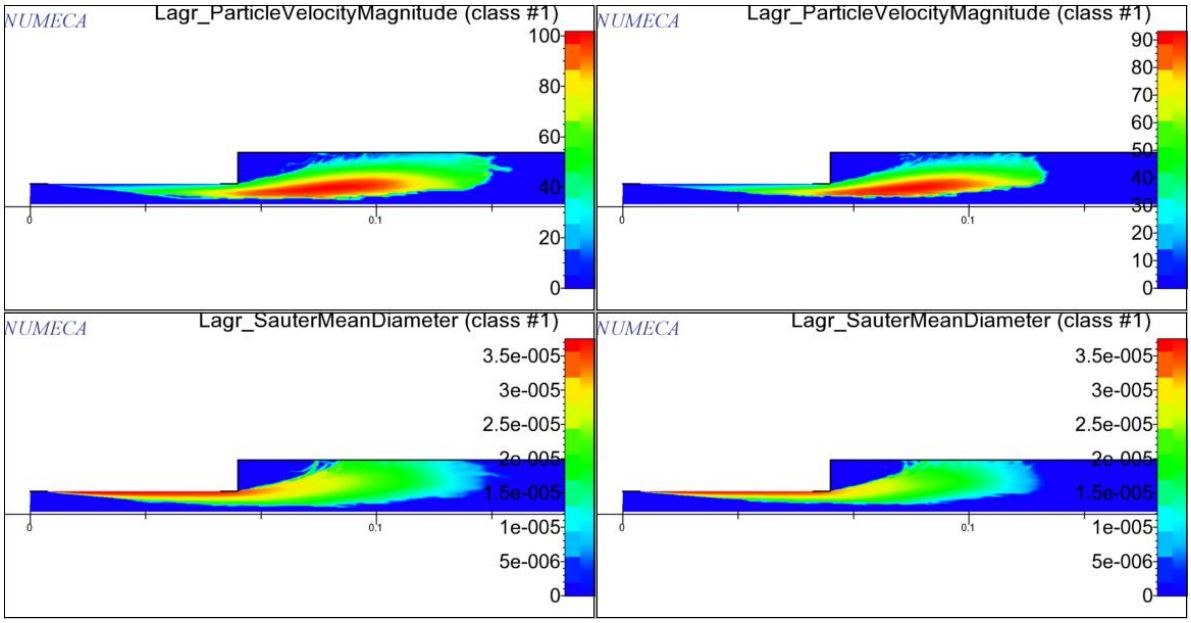

Figure 5–15 Evaporation in action. Particle velocity magnitude and corresponding sauter mean diameter, class #1. Case: O/F1.5+spray30% (on the left), and O/F1.5+spray60% (on the right).

In order to apply the study to a practical application three cross sections of the computational domain, that represent hypothetical "end" of the post combustion chamber, were considered. According to standard recommendations [100] the length of post-chamber L_{pc} lies in the range (0.5-1.0) of chamber diameter D_{cc}, therefore the three considered cross section are: $L_{pc}/D_{cc} = 0.5; 1.0; 1.5$ (see Figure 5–16 and Figure 5–17).

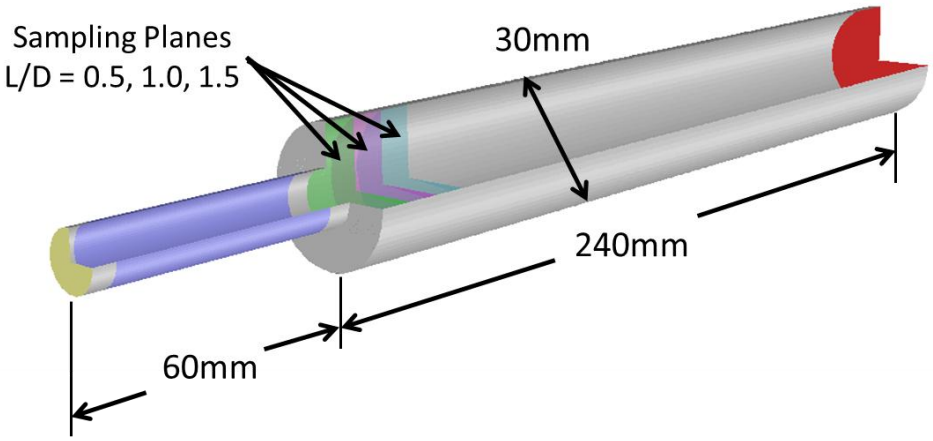

Figure 5–16 Location of sampling planes within the computational domain. 3D view

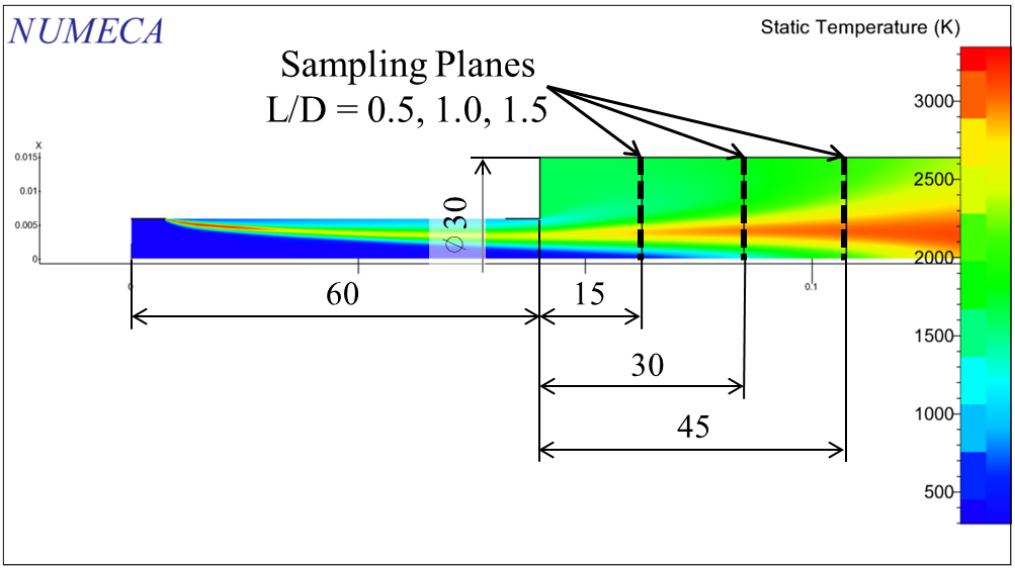

Figure 5–17 Location of sampling planes. XZ view.

The highest performance of a chemical rocket engine/motor's combustion chamber is primarily achieved by satisfying certain mixture ratio of the components O/F, so that the characteristic velocity c* reaches its maximum value.

In order to have a more complete idea on what is happening during combustion in paraffin-based hybrid rocket motors, let's investigate mixture ratios O/F in the three cross sections described above.

The Table 5–7 shows fuel mass flows and actual mixture ratios at chosen cross sections. The fuel mass flows reported in the table are taken from CFD simulations and are sums of gaseous fuel injected through the fuel inlet and evaporated liquid fuel, such as

$$\dot{m}_{gas+evap} = \dot{m}_{gas.inlet} + \dot{m}_{evap} \qquad 5–8$$

$$\dot{m}_{gas+evap} = \dot{m}_{fuel.inlet} - \dot{m}_{liquid.losses} \qquad 5–9$$

Due to incomplete evaporation of liquid phase the amount of gaseous fuel that is actually used in combustion ($\dot{m}_{gas+evap}$, see Eq. 5–8) is lower than it's expected theoretically; compare gaseous fuel mass flows in the Table 5–7 with the BCs fuel mass flows in the Table 5–3. Thereby actual mixture ratios were calculated as

$$O/F = \frac{\dot{m}_{oxidizer}}{\dot{m}_{gas+evap}} \qquad 5–10$$

and are shown in the table below. As can be seen in all the cases the mixture ratio is shifting to higher values, which means that the mixture becomes leaner (more oxidizer rich). Thus, instead of, for example, stoichiometric combustion (O/F=3.42) at the end of post combustion chamber one would get much leaner mixture.

The Figure 5–18 shows how much in percentage O/F changes when spray formation is considered with regards to the "gaseous" baseline in three L/D sections. Apparently the higher liquid fraction is, the more losses there are. The O/F is different from expected (1.5 and 3.42 in case of the current example) more than 15%, even if it's recovering over the length of the domain

Table 5–7 Mass flows of gaseous fuel and mixture ratios at three cross sections L/D=0.5, 1.0, 1.5.

			Fuel Mass Flow (gaseous+evaporated)			O/F_{actual}		
# simul	O/F_{theor}	% spray	L/D=0.5	L/D=1	L/D=1.5	L/D=0.5	L/D=1	L/D=1.5
1	1.5	0	0.00368	0.00368	0.00360	1.5	1.5	1.5
2		30	0.00288	0.00297	0.00298	1.89	1.84	1.83
3		60	0.00218	0.00236	0.00244	2.50	2.31	2.24
4	2.2	0	0.00249	0.00250	0.00246	2.2	2.2	2.2
5		30	0.00199	0.00206	0.00207	2.74	2.65	2.64
6		60	0.00155	0.00168	0.00174	3.51	3.24	3.13
7	3.42	0	0.00158	0.00160	0.00158	3.42	3.42	3.42
8		30	0.00129	0.00135	0.00136	4.23	4.05	4.00
9		60	0.00104	0.00113	0.00118	5.23	4.82	4.64
10	4.5	0	0.00119	0.00122	0.00120	4.5	4.5	4.5
11		30	0.00099	0.00104	0.00105	5.53	5.24	5.21
12		60	0.00082	0.00089	0.00091	6.63	6.16	5.98

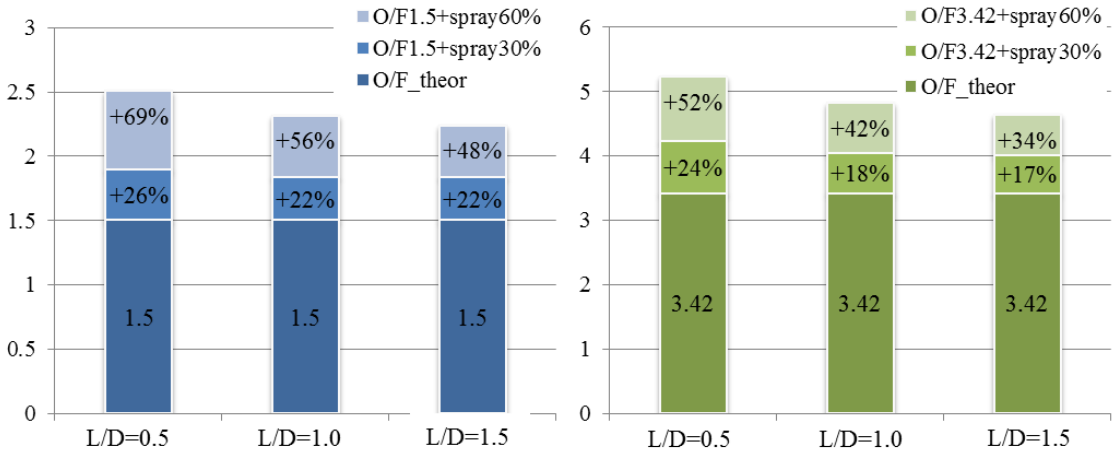

Figure 5–18 Shift of O/F ratios represented by percentage increase with regards to the gaseous baseline for O/F=1.5 (blue) and O/F=3.42 (green) at three cross-section of the domain L/D=0.5,1.0,1.5.

Another representation of the shift discussed above is mixture fraction (see Figure 5–19). The diffusion flame and the delay of full mixing can be seen in terms of mixture fraction. The specific configuration of hybrid rocket engines (see Figure 2–6), when shearing flow of oxidizer has velocity one order of magnitude higher than fuel

velocity, favour mass transport, and components mixing delay. It can be seen that the mixture fraction at the outlet f_{outlet} does not correspond to the theoretical value f_{theor}. It's interesting to note that for the case spray60% the fixture fraction taken at the very outlet is not uniform (see Figure 5–19, Cartesian plot, bottom right), which means that the fuel and oxidizer are not well-mixed.

Delay of evaporation of the liquid fuel is shown as the percentage of evaporated fuel $\dot{m}_{evap}$ with regards to the total amount of liquid fuel $\dot{m}_{liquid}$ (see Figure 5–20). It can be seen that even at the outlet the liquid fuel is not fully evaporated.

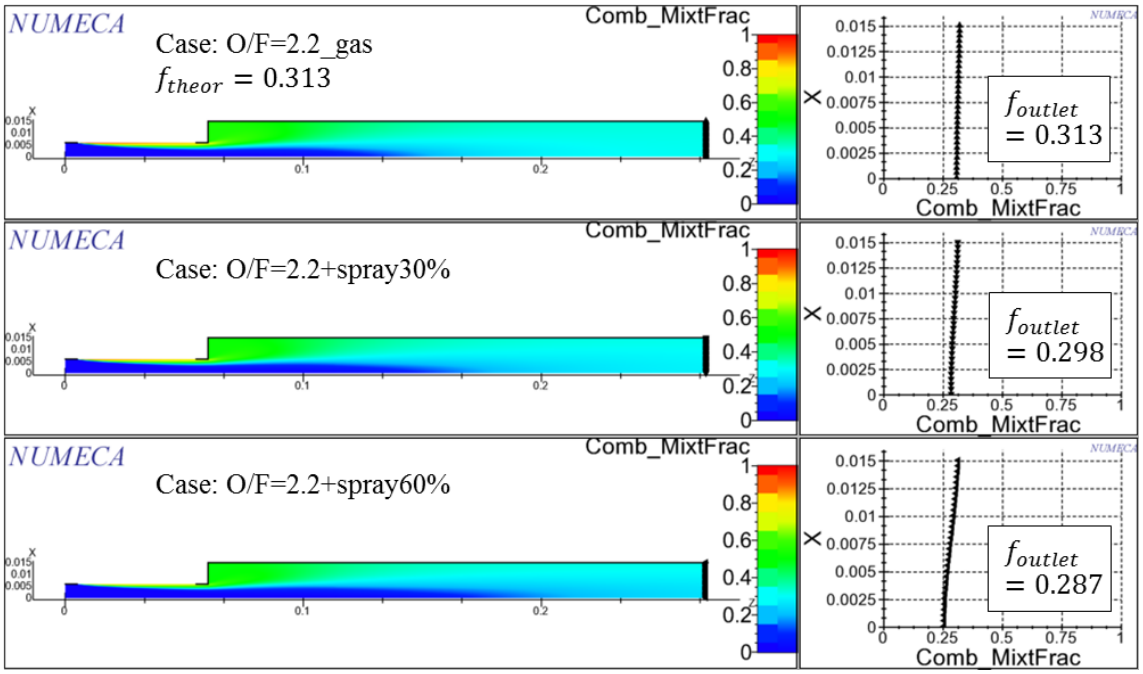

Figure 5–19 Mixture fraction. CFD results. Comparison between gaseous and two spray combustion cases.

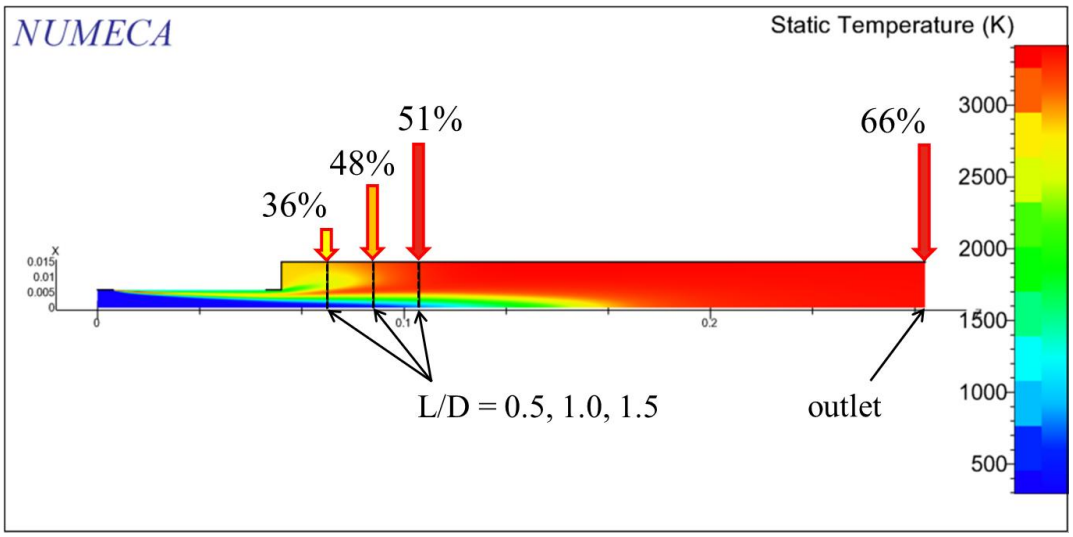

Figure 5–20 Evaporation rate through the domain. Case: O/F=3.42+spray30%

Table 5–8 Evaporation rate at different sections of the computational domain

			Evaporation rate, %			
# simul	**OF**	**% spray**	**L/D=0.5**	**L/D=1**	**L/D=1.5**	**OUTLET**
1		0	-	-	-	-
2		30	31%	39%	40%	61%
3	1.5	60	33%	41%	45%	70%
4		0	-	-	-	-
5		30	34%	44%	45%	65%
6	2.2	60	38%	46%	50%	75%
7		0	-	-	-	-
8		30	36%	48%	51%	66%
9	3.42	60	42%	52%	56%	78%
10		0	-	-	-	-
11		30	38%	53%	55%	65%
12	4.5	60	46%	55%	59%	78%

The evaporation rate is increasing (see Table 5–1) when O/F ratio is increasing for the same spray fraction (30% or 60%), because the velocity of the gaseous flow field, and thus the droplets carrier, is decreasing. For the same reason the evaporation rate is increasing when the spray fraction is higher, 60% instead of 30%.

5.4.2 Combustion chamber efficiency evaluation

Characteristic velocity c* is commonly used for combustion chamber performance evaluation and comparison between different fuel/oxidizer couples. Typical values of $c*$ for thermal engines in general fall in the interval 1500 to 3000 m/s. The quantity $c*$ is considered a parameter of merit for the engine combustion chamber: a large value indicates a good efficiency of the thermochemical energy conversion in the combustion chamber [8].

NASA “Chemical Equilibrium with Applications” software is the most common tool for engineers for a preliminary estimation of a rocket engine/motor’s characteristics. It calculates chemical equilibrium product concentrations from any set of reactants and determines thermodynamic and transport properties for the product mixture; theoretical rocket performance application is included in the range of problems available in NASA CEA.

The calculation of theoretical rocket performance (CEA) involves a number of assumptions. These assumptions are [95]:

- One-dimensional form of the continuity, energy, and momentum equations;
- Zero velocity at the combustion chamber inlet;
- Complete combustion;
- Adiabatic combustion;
- Isentropic expansion in the nozzle;
- Homogeneous mixing;
- Ideal gas law;
- Zero temperature lags and zero velocity lags between condensed and gaseous species.

Once theoretical performance is known, then for design calculations the parameters such as characteristic velocity, and specific impulse are corrected according to the expected losses in the real rocket engine/motor. For conventional HTPB-based fuels theoretical c* values are typically degraded by around 95% [93]. For paraffin-based hybrid rocket motors, as discussed above (see Chapter 5.4.1), spray combustion efficiency plays crucial role, thus the decrease of characteristic velocity is expected to be significant. In order to investigate this problem, and to have approximate values of characteristic velocity that one could expect in a real motor, CFD simulation tool was employed.

While software like CEA assumes homogeneous mixing and uniformity of the mixture and its properties, in reality in hybrid rocket motors due to their specific configuration the characteristics of the reacting flow rather consists of streams of fuel and oxidizer. The mixing zone, and the boundary between fuel and oxidizer can be seen on the Figure 5–21 in terms of gamma γ and molecular weight M_w. As can be seen, the values are not uniform, but lie in a range.

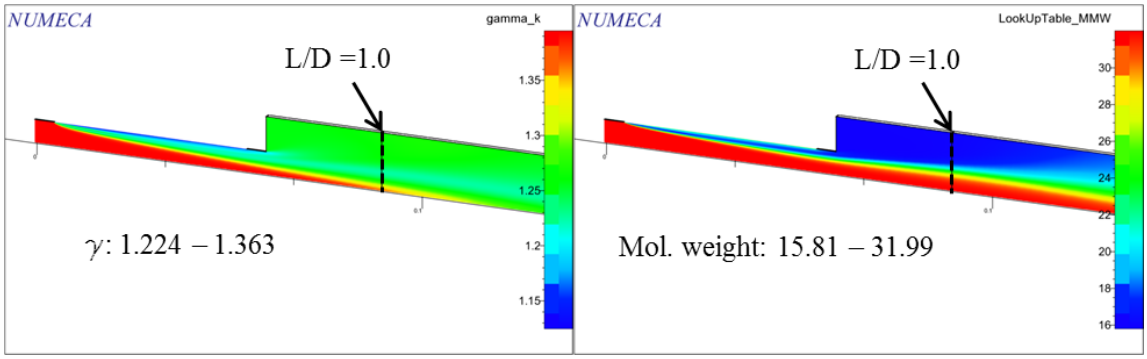

Figure 5–21 Gamma γ and molecular weight M_w profiles. Ranges of values are taken at the cross section L/D=1.0. Case: O/F2.2+spray60%

The figure below is another example of non-uniformity of the flow field in hybrid rocket motors. As can be seen at the section L/D=1.0, where there should be the end of the post combustion chamber, the temperature of the flow is in a big range: 510-3386°K. It's worth noticing that the homogeneous temperature field is reached much further downstream at L/D=4.6. In case the post combustion chamber is extended till that area then it would be a very unpractical solution for a real rocket motor.

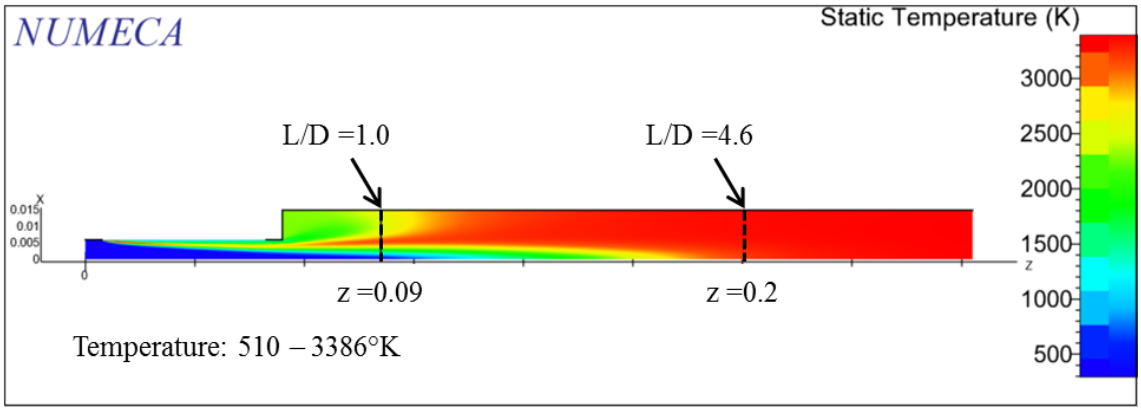

Figure 5–22 Temperature color map. The range of values that correspond to the cross section L/D=1.0 is reported as well. Case: O/F2.2+spray60%

Considering a realistically long post combustion chamber (L/D=1.0), characteristic velocity c* was calculated using the equation below

$$c^* = \sqrt{\frac{\frac{R'}{M_w} * T_0}{\gamma \left(\frac{2}{\gamma+1}\right)^{\frac{\gamma+1}{\gamma-1}}}} \qquad 5\text{–}11$$

where γ is gamma, M_w – molecular weight [g/mol], and T – temperature [K] were taken at that section of the computational domain using weighted average.

A weighted average can be both discrete and continuous, and is calculated by dividing the weighted total value of a fraction by the total of the weighting function:

$$\frac{\int_a^b f(x)w(x)dx}{\int_a^b w(x)dx} \qquad 5\text{–}12$$

Multiplying by w(x) makes some values of f(x) contribute more to the total than other values, depending on the value of x and w(x) (only the *relative* weights are relevant).

Characteristic velocity c* values calculated using numerical analysis (Eq. 5–11) are reported in the Table 5–9. The percentage of losses is shown as well. It's interesting to note that even for spray0% the losses are significant. The losses are reducing when mixture ration is increasing due to lower flow velocity. For a fixed geometry velocity will be higher for a higher total mass flow rate. As O/F=4.5 means the lowest total mass flow rate among simulated cases (see Table 5–3), that means that the velocity of the flow field is lower too, thereby there is more time for liquid fuel to be evaporated, and so evaporation rate is higher, which contributes to the combustion efficiency (see Figure 5–15 and Table 5–8).

Table 5–9 Characteristic velocity calculated using CFD data, and compared to the theoretical value obtained using CEA

OF	% spray	Temp, K	M, g/mol	γ	c*, m/s CFD	c*, m/s CEA	c*, losses
1.5	0	2281.9	20.45	1.233	1471.0	1896.6	22.4%
1.5	30	2264.5	21.44	1.243	1426.8	1873.0	23.8%
1.5	60	2263.2	22.57	1.251	1387.3	1841.5	24.7%
2.2	0	2471.9	21.90	1.245	1473.9	1876.9	21.5%
2.2	30	2429.6	22.94	1.252	1425.2	1813.6	21.4%
2.2	60	2352.2	24.02	1.258	1367.8	1733.7	21.1%
3.42	0	2551.6	24.11	1.253	1424.2	1733.7	17.9%
3.42	30	2465.8	25.01	1.258	1372.7	1673.5	18.0%
3.42	60	2356.0	25.87	1.263	1317.3	1607.3	18.0%
4.5	0	2500.0	25.54	1.257	1368.1	1649.1	17.0%
4.5	30	2396.3	26.32	1.262	1317.8	1590.3	17.1%
4.5	60	2277.3	27.05	1.267	1265.5	1536.2	17.6%

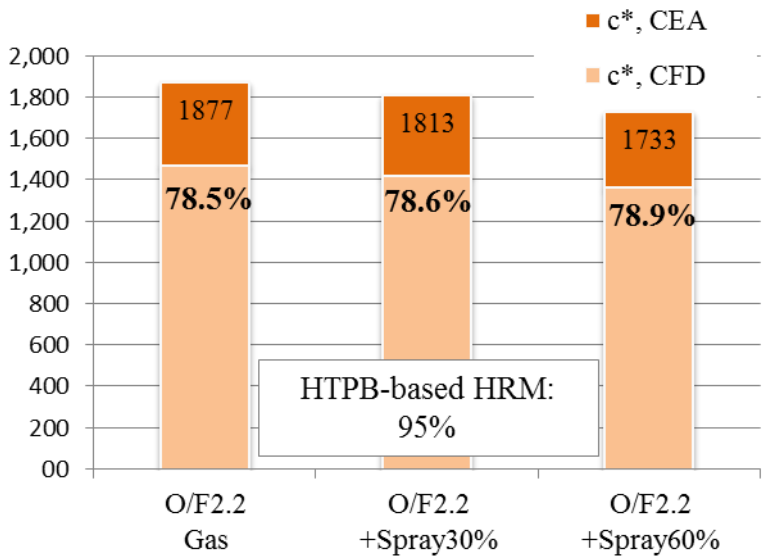

Figure 5–23 Characteristic velocity reduction due to inhomogeneity of the mixture and incomplete combustion.

While for HTPB-based hybrid rocket motors suggested drop of combustion efficiency is 95% [93], it's apparent that for paraffin-based HRMs the drop is more significant. For the investigated cases the c* reduction is in the range 75-83%, but it has to be evaluated in each particular case, because it will depend on the flow field velocity, mixture ratio O/F, droplet diameters and droplet initial temperature.

6 CONCLUSIONS AND FUTURE DEVELOPMENTS

Experimental investigation of paraffin-based fuel properties

Comparing two different strengthening materials, it's obvious that each of them has a different effect on the blend properties, while the content is equal. For instance, SEBS 30% adds twice more plasticity (strain at break) comparing to SIS 30%. TPP SEBS significantly increased the mechanical properties. It had 5-7 times higher values of Young Modulus when compared to SIS. Rheological properties investigation showed that strengthened materials can sustain higher temperature before they are melted. For SEBS15 the temperature increased in 5℃ comparing the pure paraffin baseline, and for SEBS30 – in 11℃ (from 48℃ to 59℃). SIS10 formulation did not show significant increase in rheological, mechanical properties.

So it's believed that blends of paraffin with SEBS, 15-30%, are promising paraffin-based fuels for hybrid rocket application, and will be investigated further.

Numerical simulations

The results of the numerical simulations showed several interesting effects of the entrained spray particles on the rocket motor's combustion and propulsion characteristics.

The first effect of the multiphase flow was to shift the oxidizer to fuel ratio. As a result of the entrained fuel droplets not being completely evaporated, the balance of fuel and oxidizer mixture became leaner as the entrainment increased. While the presence of the fuel droplets did add an additional fuel transport mechanism in addition to the turbulent diffusion of fuel mass through the boundary layer, which did affect the shape and character of the flame to some extent, the effect of the combustion chamber becoming leaner, was more significant in terms of its impact on how the rocket design process would be affected. Thus, instead of, for example, stoichiometric combustion (O/F=3.42) at the end of the post combustion chamber (L/D=1.0) one would instead experience a leaner mixture, O/F=4.05 for spray30% and O/F=4.82 for spray60% respectively. It's not possible to give recommendations on what exact value of mixture ratio would be, because the effects of the configuration of the motor, mass fluxes, and particle size distribution are unknown without the use of the CFD model to account for.

The result of this changing mixture ratio has a significant effect on the motor performance as well. The rocket's characteristic velocity, c*, is significantly affected by amount of fuel entrained as particles rather than gaseous fuel. Even with zero entrained particles, the motor experience significant losses in c* compared to the ideal case from CEA simply due to incomplete mixing of fuel and oxidizer in the turbulent boundary layer, for example for O/F=1.5 CEA predicts c*=1896.6 m/s whereas the CFD simulation with zero entrainment predicts c*=1471 m/s since the fuel and oxidizer

streams are not completely mixed and the combustion is therefore incomplete. However, the addition losses incurred due to incomplete evaporation of the entrained fuel when 30% of the fuel mass is entrained, decreases the characteristic velocity to c*=1426.8 m/s, which results from only 40% of the entrained mass being evaporated by the time it reaches L/D=1 from the combustion chamber.

The effect of the entrainment percentage on the evaporation percentage is a complicated and somewhat self-compensating process. When additional fuel mass is entrained and remains longer in the liquid phase, it reduces the velocity of the gas phase which allows for the fuel droplets to have longer residence time the combustion chamber. So on a percentage basis the amount of entrained fuel that is evaporated will actually increase slightly although the absolute amount of mass lost due inadequate evaporation will increase. For example in the O/F=1.5 case mentioned above, for 30% entrainment, 40% of the fuel evaporated giving c*=1426.8 m/s, but for 60% entrainment, the percentage of entrained fuel evaporated increased to 45% which, while still representing an increase in the net loss of fuel, mitigated the effect and the loss in characteristic velocity such that it decreased to c*=1387.3 m/s.

In conclusion, the efficiency of spray combustion is hard to predict by a simple correlation. Each case is unique in terms of spray description (droplet size distribution), flow field velocity, stoichiometry etc. So for each case the combustion efficiency should be studied individually and care should be taken when extrapolating the results presented here to other conditions. To illustrate this point a basic conceptual design, similar to the one described in Appendix D, suggests that the preliminary design process for a hybrid rocket motor utilizing paraffin-based fuel could substitute a liquid system, and satisfy mission requirements. That design approach in fact should be corrected for paraffin-based HRMs. Such a correction could use the data presented in this work to guide such a conceptual design.

Future development

Experimental

1. Thermal, rheological and mechanical properties investigation on various possible strengthening materials should be continued to build a data base of additives that each of them could be tailor to specific desirable properties of the fuel;
2. Visualization tests of the entrainment phenomena could significantly contribute to a better understanding of viscosity-entrainment correlation;
3. Further, those experiments ideally should be coupled with ballistic tests and regression rate data;

Numerical

4. In order to reach higher level of accuracy of paraffin-based HRM simulations more studies on spray formation in paraffin-based hybrids are needed such as fraction of the total fuel entrained as liquid phase, droplet size distribution, and liquid phase initial temperature. Those properties are essential as they significantly affect the evaporation and consequently the efficiency of combustion chamber;
5. Reliable chemical kinetic scheme is required;
6. In order to have a reliable chemistry model and for the droplet size distribution data a laser diagnostic experimental investigation could be employed;

There are several different possible laser-based measurement techniques that could help validate the CFD modeling approach and shed light on how it could be refined or enhanced. The first method would consist of using the pattern of light scattered by the droplets according to recover the particle size distribution from mie-scattering theory [105]. A second method for focusing on the gas-phase combustion processes themselves would be to use tunable diode lasers for absorption-based measurements of the gas temperature but also of the concentrations of the primary species of interest such as CO, CO2, and H2O [106]. Since such absorption-based measurements have also been extended to high-frequency sampling rates, they could also be used to detect and quantify any unsteadiness in the combustor which could indicate the need for time-resolved CFD modeling methods like URANS (Unsteady Reynolds Averaged Navier Stokes) or LES (Large Eddy Simulation) rather than RANS (Reynolds-Averaged Navier Stokes). One final method would be to make detailed concentration measurements of a variety of different species using coherent anti-Stokes Raman scattering [107], which could give information on how to improve the chemical kinetics used in the CFD model.

7. Ultimately, regression rate prediction model is a desirable tool to have in hand.

7 BIBLIOGRAPHY

[1] B. J. Cantwell, "Wax Fuel Gives Hybrid Rockets More Oomph," 5 November 2014. [Online]. Available: http://spectrum.ieee.org/aerospace/space-flight/wax-fuel-gives-hybrid-rockets-more-oomph.

[2] M. Boiocchi, L. Merotto and L. Galfetti, "Paraffin-Based Fuels Filled with Lithium-Based Additives Characterization," in *63rd International Astronautical Congress (IAC)*, Naples, Italy, 2012.

[3] M. A. Karabeyoglu, "Transient Combustion in Hybrid Rockets," Ph.D. Dissertation, Department of Aeronautics and Astronautics, Stanford Univ., CA, Aug. 1998.

[4] M. A. Karabeyoglu, B. J. Cantwell and D. Altman, "Development and Testing of Paraffin-based Hybrid Rocket Fuels," in *37th AIAA/ASME/SAE/ASEE Joint Propulsion Conference and Exhibit*, Salt Lake City, Utah, 2001.

[5] M. A. Karabeyoglu, D. Altman and B. J. Cantwell, "Combustion of Liquefying Hybrid Propellants: Part 1, General Theory," *Journal of Propulsion and Power*, vol. 18, pp. 610-620, 2002.

[6] M. Boiocchi, L. Merotto, F. Maggi, L. Di Landro and L. Galfetti, "Rheological and Mechanical Characterization of Hybrid Rocket Solid Fuels," in *EUCASS Conference*, Saint Petersburg, Russia, 2011.

[7] M. Boiocchi, P. Milova, L. Galfetti, L. Di Landro and A. K. Golovko, "A wide characterization of paraffin-based fuels mixed with styrene-based thermoplastic polymers for hybrid propulsion," in *5th EUCASS Conference*, Munich, Germany, 2013.

[8] L. T. DeLuca, *Energetic Problems in Aerospace Propulsion*, Milan, MI: Politecnico Di Milano, 2000.

[9] D. Altman and Holzman A., "Overview and History of Hybrid Rocket Propulsion," in *Fundamentals of Hybrid Rocket Combustion and Propulsion*, vol. 218, M. J. Chiaverini and K. Kuo, Eds., Reston, Virginia, American Institute in Aeronautics and Astronautics, Inc., 2007, pp. 1-36.

[10] D. Altman, "Hybrid Rocket Development History," in *27th AIAA/SAE/ASME/ASEE Joint Propulsion Conference*, Sacramento, CA, June 1991.

[11] "Hybrid Rockets History," Space Propulsion Group, Inc., 2012. [Online]. Available: http://www.spg-corp.com/News_12.php. [Accessed April 2015].

[12] "Scaled Composites," [Online]. Available: http://www.scaled.com/.

[13] "Virgin Galactic," [Online]. Available: http://www.virgingalactic.com/.

[14] G. A. Marxman, C. E. Wooldridge and R. J. Muzzy, "Fundamentals of Hybrid Boundary Layer Combustion," in *Heterogeneous combustion conference*, Palm Beach, FL, 1963.

[15] G. A. Marxman, "Combustion in the Turbulent Boundary Layer on a Vaporizing Surface," *10th Symposium (International) on Combustion*, pp. 1337-1349, The Combustion Intitute, 1965.

[16] G. A. Marxman, "Boundary Layer Combustion in Propulsion," in *Proceedings of the 11th Symposium (International) on Combustion, The Combustion Institute*, pp. 269-289. Pittsburgh, Pennsylvania, 1967.

[17] G. A. Risha, G. C. Harting, K. K. Kuo, A. Peretz, D. E. Koch, H. Stephen Jones and J. P. Arves, "Pyrolysis and Combustion of Solid Fuels in Various Oxidizing Eenvironments," in *34th AIAA/ASME/SAE/ASEE Joint Propulsion Conference and Exhibit*, Cleveland,OH, 1998.

[18] P. George, S. Krishnan, P. M. Varkey, M. Ravindran and L. Ramachandran, "Fuel Regression Rate Enhancement Studies in HTPB/GOX Hybrid Rocket Motors," in *34th AIAA/ASME/SAE/ASEE Joint Propulsion Conference and Exhibit*, Cleveland,OH, 1998.

[19] L. D. Smoot and C. F. Price, "Regression Rates of Nonmetalized Hybrid Fuel Systems," *AIAA Journal*, vol. 3, no. 8, pp. 1408-1413, 1965.

[20] W. K. Knuth, M. J. Chiaverini and D. J. Gramer, "Solid-Fuel Regression Rate Behavior of Vortex Hybrid Rocket Engines," *Journal of Propulsion and Power*, vol. 18, no. 3, pp. 600-609.

[21] W. H. Knuth, M. J. Chiaverini, D. J. Gramer and J. A. Sauer, "Numercal Simulation of Vortex-Driven Hybrid Rocket Engines," AIAA Paper 98-3351, July 1998.

[22] S. Yuasa, K. Yamamoto, H. Hachiya, K. Kitagawa and Y. Oowada, "Development of a Small Sounding Hybrid Rocket with a Swirling-Oxidizer-Type Engine," AIAA Paper 2001-3537, 2001.

[23] C. Lee, Y. Na and G. Lee, "The Enhancement of Regression Rate of Hybrid Rocket Fuel by Helical Grain Configuration and Swirl Flow," AIAA Paper

2005-3906, 2005.

[24] E. E. Rice , D. J. Gramer, C. P. Clair and M. J. Chiaverini, "Mars ISRU CO/O2 Rocket Engine Development and Testing," in *7th NASA International Microgravity Combustion Symposium*, 2003.

[25] G. Haag, M. Sweeting and G. Richardson, "An Alternative Geometry Hybrid Rocket for Spacecraft Orbit Transfer Manoeuvers," in *51st International Astronautical Congress*, Oct. 2000.

[26] J. R. Caravella, S. D. Heister and E. J. Wernimont, "Characterization of Fuel Regression in a Radial Flow Hybrid Rocket," *Journal of Propulsion and Power*, vol. 14, no. 1, 1998.

[27] G. Haag, *Alternative Geometry Hybrid Rockets for Spacecraft Orbit Transfer*, Surrey, UK: Ph.D. dissertation. Surrey Space Centre. University of Surrey., 2001.

[28] M. Miho, I. Tatsuya, Y. Saburo, S. Takashi, S. Noriko and S. Toru, "Visualization of Flames in Combustion Chamber of Swirling-Oxidizer-Flow-Type Hybrid Rocket Engines," in *46th AIAA/ASME/SAE/ASEE Joint Propulsion Conference & Exhibit*, Paper AIAA 2010-6546. Nashville, TN, 2010.

[29] N. Bellomo, M. Lazzarin, F. Barato and M. Grosse, "Numerical Investigation of the Effect of a Diaphragm on the Performance of a Hybrid Rocket Motor," in *46th AIAA/ASME/SAE/ASEE Joint Propulsion Conference & Exhibit*, Paper AIAA 2010-7033. Nashville, TN, 2010.

[30] L. Galfetti, L. T. DeLuca, C. Paravan, L. Merotto and M. Boiocchi, "Regression Rate and CCPs Measurement of Metallized Solid Fuels," in *8th ISICP (International Symposium on Chemical Propulsion)*, Cape Town, South Africa, 2009.

[31] L. T. DeLuca, L. Galfetti, F. Maggi, G. Colombo, A. Reina, S. Dossi, D. Consonni and M. Brambilla, "Innovative Metallized Formulations for Solid or Hybrid Rocket Propulsion," *HANNENG CAILIAO (ISSN: 1006-9941)*, vol. 20, no. 4, pp. 465 - 474, 2012.

[32] S. Dossi, A. Reina, F. Maggi and L. T. De Luca, "Innovative Metal Fuels for Solid Rocket Propulsion," *International Journal of Energetic Materials And Chemical Propulsion (ISSN: 2150-766X)*, vol. 11, no. 4, pp. 299 - 322, 2012.

[33] A. Chandler, E. T. Jens, B. J. Cantwell and G. S. Hubbard, "Visualization of the Liquid Layer Combustion of Paraffin Fuel at Elevated Pressures," in *63rd International Astronautical Congress*, Naples, Italy, 2012.

[34] "OpenFOAM. The open source CFD toolbox," [Online]. Available: http://www.openfoam.com/.

[35] G. Gariani, F. Maggi and L. Galfetti, "Simulation Code for Hybrid Rocket Combustion," in *46th AIAA/ASME/SAE/ASEE Joint Propulsion Conference & Exhibit*, Nashville, TN, 2010.

[36] M. J. Chiaverini, K. K. Kuo, A. Petrez and G. C. Harting, "Heat Flux and Internal Ballistic Characterizationof a Hybrid Rocket Motor Analog," in *33th AIAA/ASME/SAE/ASEE Joint Propulsion Conference and*, AIAA-97-3080, Seattle, 1997.

[37] A. Coronetti and W. A. Sirignano, "Numerical Analysis of Hybrid Rocket Combustion," *Journal of Propulsion and Power*, vol. 29, no. 2, pp. 371-384, 2013.

[38] F. M. Favarò, W. A. Sirignano, M. Manzoni and L. T. DeLuca, "Solid Fuel Regression Rate Modeling for Hybrid Rockets," *Journal of Propulsion and Power*, vol. 29, no. 1, pp. 205-215, 2013.

[39] V. Sankaran and C. L. Merkle, "Size Scale-Up in Hybrid Rocket Motors," in *34th Aerospace Sciences Meeting and Exhibit*, AIAA Paper 96-0637, Reno, NV, 1996.

[40] N. S. Cohen, R. W. Fleming and R. L. Derr, "Role of Binders in Solid Propellant Combustion," *AIAA Journal*, vol. 12, no. 2, pp. 212-218, 1974.

[41] H. Arisawa and T. B. Brill, "Flash Pyrolysis of Hydroxyl Terminated Poly-Butadiene (HTPB). I: Implications of Kinetics to Combusiton of Organic Polymers," *Combusiton and Flame*, vol. 106, no. 1-2, 1996.

[42] H. Arisawa and T. B. Brill, "Flash Pyrolysis of Hydroxyl Terminated Poly-Butadiene (HTPB). II: Analysis and Implications of the Gaseous Products," *Combustion and Flame*, vol. 106, no. 1-2, 1996.

[43] G. C. Cheng, R. C. Farmer, H. S. Jones and J. S. McFarlane, "Numerical Simulations of the Internal Ballistics of a Hybrid Rocket Motor," in *32nd Aerospace Sciences Meeting and Exhibit*, AIAA Paper 94-0554, Reno, NV, 1994.

[44] A. Li and G. Ahmadi, "Dispersion and Deposition of Spherical Particles from Point Sources in a Turbulent Channel Flow," *Aerosol Science and Technology*, vol. 16, pp. 209-226, 1992.

[45] J. Y. Lestrade, J. Anthoin and G. Lavergne, "Liquefying Fuel in Hybrid Propulsion: First Step Towards a 1D Model," in *4th European Conference for*

Aeronautics and Space Sciences (EUCASS), 2011.

[46] J. Y. Lestrade, J. Anthoine and G. Lavergne, "Modeling of Liquefying Fuel Regression Rates in Hybrid Propulsion," in *5th European Conference for Aeronautics and Space Sciences (EUCASS)*, Munich, Germany, 2013.

[47] [Online]. Available: http://igiwax.com/reference/wax-tests.html.

[48] H. Bennett, Industrial Waxes, vol. 2 (Compounded Waxes and Technology), New York: Chemical Publishing Company, Inc., 1975, p. 110.

[49] H. Bennett, Industrial Waxes, vol. 2 (Compounded Waxes and Technology), New York: Chemical Publishing Company, inc., 1975, pp. 254-255.

[50] [Online]. Available: http://www.sigmaaldrich.com.

[51] M. J. Chiaverini, "Review of Solid-Fuel Regression Rate Behavior in Classical and Nonclassical Hybrid Rocket Motors," in *Fundamentals of Hybrid Rocket Combustion and Propulsion*, vol. 218, M. J. Chiaverini and K. K. Kuo, Eds., Reston, Virginia, American Institute of Aeronautics and Astronautics, Inc., 2007, pp. 37-126.

[52] C. Paravan, M. Viscardi, L. T. DeLuca and A. Kazakov, "Regression Rates and Anisotropy Effects in Hybrid Rockets Microburner," in *3rd EUCASS (European Conference for Aerospace Sciences) Conference*, Versailles, France, 04–07 July 2009.

[53] *TA Instruments. AR 500/1000 Rheometers. Hardware Manual*, New Castle, DE, 2000.

[54] *ISO 527-1:2012 "Plastics – Determination of tensile properties. Part 1: General principles"*.

[55] *ISO 527-2:2012 "Plastics — Determination of tensile properties. Part 2: Test conditions for moulding and extrusion plastics"*.

[56] J. D. DeSain, B. B. Brady, K. M. Metxler, T. J. Curtiss and T. V. Albright, "Tensile Tests of Paraffin Wax for Hybrid Rocket Fuel Grains," in *AIAA 2009-5115, Joint Propulsion Conference & Exhibit*, Denver, Colorado, 2 – 5 August 2009.

[57] Computer Methods in Applied Mechanics and Engineering, Amsterdam: North-Holland, 1972.

[58] D. C. Wilcox, Turbulence Modeling for CFD, DCW Industries, Inc., 1993.

[59] B. E. Launder and D. B. Spalding, Lectures in Mathematical Models of Turbulence, London, England: Academic Press, 1972.

[60] Y. R. Sivathanu and G. M. Faeth, "Generalized State Relationships for Scalar Properties in Non-Premixed Hydrocarbon Flames," *Combustion and Flame,* vol. 82, pp. 211-230, 1990.

[61] "Theoretical Manual. FINE/Open v3.1," Numeca International, Brussels, Belgium, 2013.

[62] "Users Manual. ANSYS Fluent. Mixture Fraction Theory," Fluent Inc., 2006.

[63] L. D. Smoot, W. C. Hecker and G. A. Williams, "Prediction of propagating methane-air flames," *Combustion and Flame,* vol. 26, p. 323, 1976.

[64] G. Tsatsaronis, "Prediction of propagating laminar flames in methane, oxygen. nitrogen mixtures," *Combustion and Flame,* vol. 33, p. 217, 1978.

[65] C. K. Westbrook and F. L. Dryer, "Prediction of laminar flame properties of methanol-air mixtures," *Combustion and Flame,* vol. 37, p. 171, 1980.

[66] "Physical and Life Sciences Organization," [Online]. Available: https://www-pls.llnl.gov/?url=science_and_technology-chemistry-combustion-c8c16_n_alkanes.

[67] . C. K. Westbrook, W. J. Pitz, O. Herbinet, H. J. Curran and E. J. Silke, "A Detailed Chemical Kinetic Reaction Mechanism for n-Alkane Hydrocarbons from n-Octane to n-Hexadecane," *Combust. Flame,* vol. 156, no. 1, pp. 181-199, 2009.

[68] C. K. Westbrook, W. J. Pitz, O. Herbinet, H. J. Curran and E. J. Silke, "A comprehensive detailed chemical kinetic reaction mechanism for combustion of n-alkane hydrocarbons from n-octane to n-hexadecane," *Combustion and Flame,* vol. 156, pp. 181-199, 2009.

[69] C. K. Westbrook and K. Charles, "Simplified Reaction Mechanisms for the Oxidation of Hydrocarbon Fuels in Flames," *Combustion Science and Technology,* vol. 27, pp. 31-43, 1981.

[70] A. Zizin, *"Development of a Reduced Chemical-Kinetic Combustion Model for Practical Fuels",* Ph.D. dissertation. Institute of Combustion Technology for Aerospace Engineering. University of Stuttgart, 2013.

[71] J. Warnatz, U. Maas and R. Dibble, Combustion. Physical and Chemical Fundamentals, Modeling and Simulations, Experiments, Pollutant Formation, 3rd ed., Heidelberg: Springer, 2006, pp. 115-117.

[72] C. H. Bamford and C. F. H. Tipper, Eds., "Liquid-phase oxidation," in *Comprehensive Chemical Kinetics*, vol. 16, Amsterdam, The Netherlands, Elsevier Scientific Publishing Company, 1980.

[73] C. H. Bamford and C. F. H. Tipper, Eds., "Decomposition and isomerization of organic compounds," in *Comprehensive chemical kinetics*, vol. 5, Amsterdam, The Netherlands, Elsevier Scientific Publishing Company, 1972.

[74] F. O. Rice and K. F. Herzefeld, "The Thermal Decomposition of Organic Compounds from the Standpoint of Free Radicals. VI.The Mechanism of Some Chain Reactions," *J. Amer. Chem. Soc.,* vol. 56, p. 284, 1934.

[75] A. Kossiakoff and F. O. Rice, "Thermal Decomposition of Hydrocarbons, Resonance Stabilization and Isomerization of Free Radicals," *Journal of the American Chemical Society,* vol. 65, no. 4, p. 590–595, 1943.

[76] M. Watanabe, M. Tsukagoshi, H. Hirakoso, T. Adschiri and K. Arai, "Kinetics and Product Distribution of n-Hexadecane Pyrolysis," *AIChE Journal,* vol. 46, no. 4, pp. 843-856, 2000.

[77] F. Behar and M. Vandenbroucke, "Experimental Determination of the Rate Constants of the n-C25 Thermal Cracking at 120, 400, and 800 bar: Implications for High-Pressure/High-Temperature Prospects," *Energy & Fuels,* vol. 10, pp. 932-940, 1996.

[78] J. M. Simmie, "Detailed chemical kinetic models for the combustion of hydrocarbon fuels," *Progress in Energy and Combustion Science,* vol. 29, pp. 599-634, 2003.

[79] J. F. Griffiths, "Reduced kinetic models and their application to practical combustion systems," *Prog. Energy Combust, Sci,* vol. 21, pp. 25-107, 1995.

[80] M. L. Poutsma, "Fundamental reactions of free radicals relevant to pyrolysis reactions," *Journal of Analytical and Applied Pyrolysis,* vol. 54, pp. 5-35, 2000.

[81] "The Combustion Laboratory at the University of California, Berkeley," [Online]. Available: http://combustion.berkeley.edu/gri-mech/version30/text30.html.

[82] C. T. Crowe and E. E. Michaelides, "Basic Concepts and Definitions," in *Multiphase Flow Handbook*, C. T. Crowe, Ed., Boca Raton, FL, CRC Press of Taylor & Francis Group, 2006.

[83] R. A. Mugele and H. D. Evans, "Droplet Size Distribution in Sprays," *Ind Eng. Chem.,* vol. 43, p. 1317, 1951.

[84] M. Wicks and A. E. Dukler, "In Situ Measurements of Drop Size Distribution in Two-Phase Flow," in *Int. Heat Transfer Conf.*, Chicago, 1966.

[85] L. B. Cousins and G. F. Hewitt, "Liquid Phase Mass Transfer in Annular Two-Phase Flow: Droplet Deposition and Liuquid Entrainment," UK AEA Report AERER5657, 1968.

[86] D. F. Tatterson, I. C. Dallman and T. J. Hanratty, "Drop Size in Annular Gas-Liquid Flow," *AIChE J.*, vol. 23, p. 68, 1977.

[87] R. D. Lindsted, D. L. Evans, J. Gass and R. V. Smith, "Droplet and Flow Pattern Data for Vertical Two-Phase Air-Water Flow Using Axial Photography," Technical Report, Wichita State University, Department of Mechanical, 1978.

[88] I. Kataoka, M. Ishii and K. Mishima, "Generation and Size Distribution of Droplet in Annular Two-Phase Flow," *J. Fluid Engineering*, vol. 105, p. 230, 1983.

[89] K. K. Kuo and R. W. Houim, "Theoretical Modeling and Numerical Simulation Challenges of Combustion Processes of Hybrid Rockets," in *47th AIAA/ASME/SAE/ASEE Joint Propulsion Conference & Exhibit*, San Diego, CA, 2011.

[90] P. Sawant, M. Ishii and M. Mori, "Prediction of amount of entrained droplets in vertical annular two-phase flow," *Int. J. of Heat and Fluid Flow*, vol. 30, pp. 715-728, 2009.

[91] P. Sawant, M. Ishii and M. Mori, "Droplet entrainment correlation in vertical upward co-current annular two-phase flow," *Nuclear Engineering and Design*, vol. 238, pp. 1342-1352, 2008.

[92] W. T. Kelvin, "Hydrokinetic solutions and observations," *Philosophical Magazine*, vol. 42, pp. 362-377, 1871.

[93] G. P. Sutton and O. Biblarz, Rocket Propulsion Elements, 7th ed., John Wiley & Sons, Inc., 2001, pp. 593-599.

[94] F. Mashayek, "Multiphase Interactions. Combustion," in *Multiphase Flow Handbook*, Boca Raton, FL, Taylor and Francis group, 2006, pp. 12-98 - 12-134.

[95] S. Gordon and B. J. McBride, "Computer Program for Calculation of Complex Chemical Equilibrium Compositions and Applications I. Analysis," NASA Lewis Research Center, Cleveland, Ohio, 1994.

[96] B. J. McBride and S. Gordon, "Computer Program for Calculation of Complex Chemical Equilibrium Compositions and Applications II. User's Manual and Program Description," NASA Lewis Research Center, Cleveland, Ohio, 1996.

[97] "Chemical Equilibrium with Applications," [Online]. Available: http://www.grc.nasa.gov/WWW/CEAWeb/ceaHome.htm.

[98] Y. A. Cengel and J. M. Cimbala, Fluid mechanics: fundamentals and applications (1st ed.), Boston: McGraw-Hill Higher Education, 2006, pp. 321-329.

[99] B. J. McBride and S. Gordon, *Computer program for calculation of complex chemical equilibrium compositions and applications,* NASA reference publication 1311, 1996.

[100] D. Altman and R. Humble, "Hybrid Rocket Propulsion Systems," in *Space Propulsion Analysis and Design*, R. W. Humble, G. N. Henry and W. J. Larson, Eds., New York, The McGraw-Hill Companies, Inc., Primis Custom Publishing, 1995, pp. 403-441.

[101] "Chapter 1. General Data," in *Technical data book*, University Park, PA, American Petroleum Institute, 1997, pp. 1-58, 1-59.

[102] S. Himran and A. Suwono, "Characterization of Alkanes and Paraffin Waxes for Application as Phase Change Energy Storage Medium," *Energy Sources,* vol. 16, pp. 117-128, 1994.

[103] "Users Manual. ANSYS Fluent. Judging Convergence.," Fluent Inc., 2006.

[104] J. Blazek, Computational Fluid Dynamics: Principles and Applications, Oxford, UK: ELSEVIER Science Ltd., 2001, pp. 47-48.

[105] D. L. Black, M. Q. McQuay and M. P. Bonin, "Laser-based techniques for particle-size measurement: a review of sizing methods and their industrial applications.," *Progress in Energy and Combusiton Science,* vol. 22, no. 3, pp. 267-306, 1996.

[106] M. E. Webber, J. Wang, S. T. Sanders, D. S. Baer and R. K. Hanson, "In situ combustion measurements of CO, CO2, H2O and temperature using diode laser absorption sensors," *Proceedings of the Combusiton Institute,* vol. 28, no. 1, pp. 407-413, 2000.

[107] A. C. Eckbreth, Laser diagnostics for combustion temperature and species, CRC Press, 1996.

[108] "User Manual. FINE™/Open v3.1 (Including OpenLabs)," NUMECA

International, Brussels, Belgium, 2013.

[109] *VEGA User's Manual,* Arianspace, Issue 3, March 2006.

[110] "European Launch Vehicle," [Online]. Available: http://www.elv.it/en/.

[111] F. A. Williams, Combustion Theory, 2nd ed., Menlo Park, CA: The Benjamin/Cummings Publishing Company, 1985.

[112] R. T. Holzmann, Chemical Rockets, New York, NY: Marcel Dekker, 1969.

[113] B. Cantwell, A. Karabeyoglu and D. Altman, "Recent Advances in Hybrid Propulsion," *International Journal of Energetic Materials and Chemical Propulsion,* vol. 9, no. 4, pp. 305-326, 2010.

[114] K. K. Kuo and F. B. Cheung, "Droplet Entrainment and Breakup by Shear Flows," *JANNAF Combustion Subcommittee Meeting,* vol. I, pp. 59-72, November 1993.

[115] M. Ishii and K. Mishima, "Droplet Entrainment Correlation in Annular Two Phase Flow," *Int. J. Heat Mass Transfer,* vol. 32, no. 10, p. 1835, 1989.

[116] T. E. Dauber and R. T. Danner, Physical and Thermodynamic Properties of Pure Chemicals, Data Compilation, Washington, DC: Taylor and Francis, 1997.

[117] E. S. Domalski, W. H. Evans and E. D. Hearing, "Heat capacities and Entropies of Organic Compounds in the Condesed Phase," *Journal of Physical and Chemical Reference Data,* vol. 13, 1984.

[118] M. Freund, R. Csikos, S. Keszthelyi and G. Mozes, Paraffin products. Properties, technologies, applications, Amsterdam, The Netherlands: Elsevier Scientific Publishing Company, 1982.

[119] M. J. Chiaverini, "Review of Solid Fuel Regression Rate Behavior in Classical and Nonclassical Hybrid Rocket Motors," in *Fundamentals of Hybrid Rocket Combustion and Propulsion,* vol. 218, M. J. Chiaverini and K. K. Kuo, Eds., Reston, Virginia, AIAA Progress in Astronautics and Aeronautics, 2007, pp. 37-125.

[120] H. R. Linden and R. E. Peck, "Gaseous Product Distribution in Hydrocarbon Pyrolysis," *Industrial and Engineering Chemistry,* vol. 47, no. 12, pp. 2470-2474.

[121] J. Warnatz, "Hydrocarbon oxidation high-temperature chemistry," *Pure Appl. Chem.,* vol. 72, no. 11, p. 2101–2110, 2000.

[122] S. Maruyama, T. Ishiguro, K. Shinohara and I. Nakagawa, "Study on Mechanical Characteristic of Paraffin-Based Fuel," in *47th AIAA/ASME/SAE/ASEE Joint Propulsion Conference & Exhibit*, San Diego, CA, 2011.

[123] Y. S. Chen , P. Liaw, H.-M. Shang and C. P. Chen, "Numerical Analysis of Complex Internal and External Viscous Flows with a Second-Order Pressure-Based Method," in *24th Fluid Dynamics Conference*, AIAA Paper 93-2966, Orlando, FL, 1993.

A APPENDIX. FINE™/OPEN WITH OPENLABS. SOLVER SETTINGS

"FINE™/Open with OpenLabs" developed by NUMECA Int. was used for numerical simulations of combustion and spray combustion. All the main settings used for the simulations are summarized in the Table below. Some screenshots of the software interface are also presented.

A personal laptop was used for the simulations with the following performance characteristics:

- 6 Gb RAM
- Intel® Core ™ i3-2330M CPU @ 2.2GHz

The time required to reach 11000 iterations of gaseous solution of the simulation was around 10 hours (in serial mode). About the same time (10-11 hours) was taking multiphase coupled simulation (22 Lagrangian cycles and 6600 Eulerian iterations), which means 20-22 hours for a full spray combustion simulation.

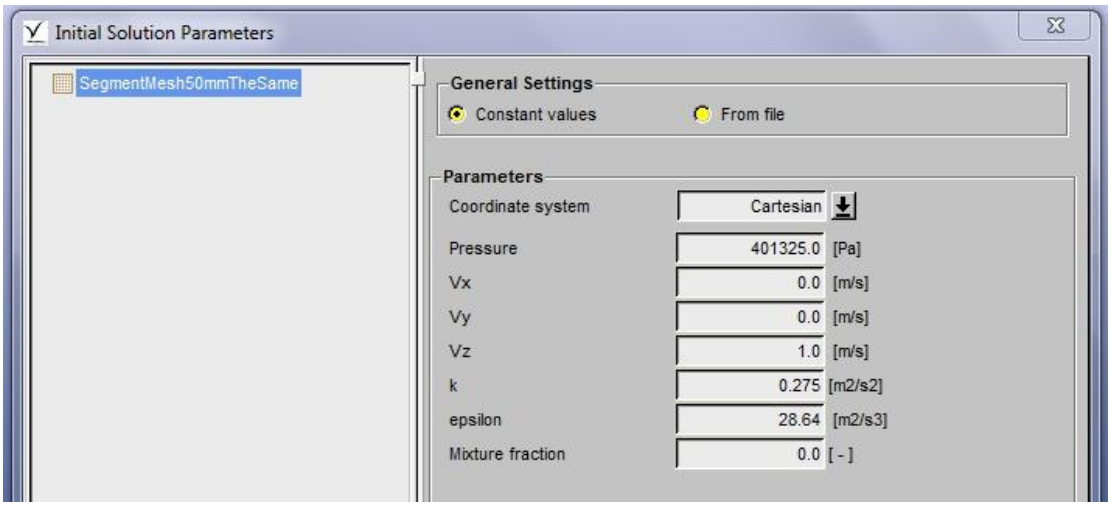

Figure A–1 Initial settings for gaseous combustion simulations (spray0%)

Table A–1 Main settings of the FINE™/Open solver used for numerical simulations

<table>
<tr><td>Fluid model</td><td>Flow model: Navier-Stokes
Turbulence model: k-epsilon (standard)
Reference Length: 0.012 m
Reference velocity: 10 m/s</td></tr>
<tr><td>Combustion</td><td>Combustion type: Non-premixed
Chemistry model: Flamelet
Mixture fraction variance eq.: On
NOx post-processing: None
Combustion look-up tables: choose the tables</td></tr>
<tr><td>Fluid-Particle interaction</td><td>2-way coupling: On
Number of global cycles: 22
Relaxation factor for Lagrangian source terms: 0.25
Number of particles injected per cell: 15
Particle forces: Drag (Schiller-Naumann), Dispersion
Heating/cooling: On</td></tr>
<tr><td>Boundary conditions</td><td>InletOx, InletFuel: Subsonic, Cylindrical, Mass flow imposed (Velocity Direction)
Outlet: Subsonic, Static pressure imposed
Solid: Navier-Stokes, Adiabatic</td></tr>
<tr><td>Initial solution</td><td>For gas cases: Constant values (see Figure A–1)
For cases Spray 30-60%: from file (converged solution Spray 0%)</td></tr>
<tr><td>Numerical parameters general</td><td>Multigrid. Number of grids: 4
Correction damping: On
Number of sweeps: 1 2 3 4 5 6 7 8 9 10 (default)
Maximum number of cycles per grid level: 1000
Convergence criteria on each grid level: -5.5</td></tr>
<tr><td>Numerical scheme</td><td>Central, 2nd order
CFL: 1.5</td></tr>
<tr><td>Preconditioning</td><td>β* coefficient: 3.0

Computational case — Characteristic velocity, m/s
OF1.5, spray 0-30-60% — 120
OF2.2, spray 0-30-60% — 120
OF3.42, spray 0-30-60% — 110
OF4.5, spray 0-30-60% — 70</td></tr>
<tr><td>Computational control</td><td>Number of iterations (spray 0%): 8000
Number of iterations (spray 30-60%): 300
Convergence criteria: -6
Launching mode: serial</td></tr>
</table>

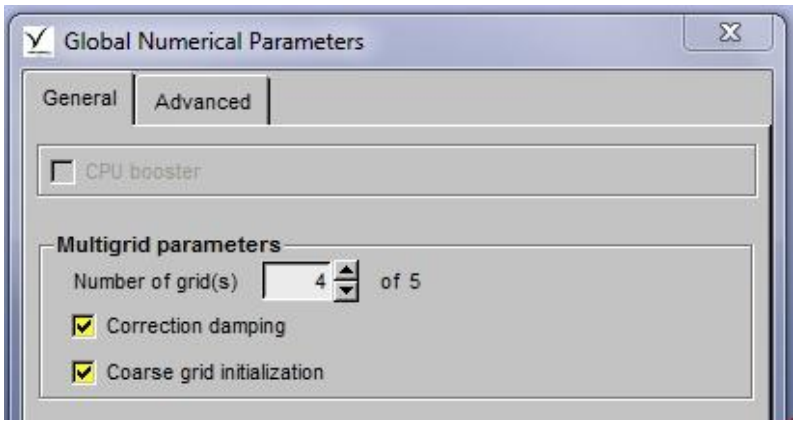

Figure A–2. Multigrid settings. Number of grids

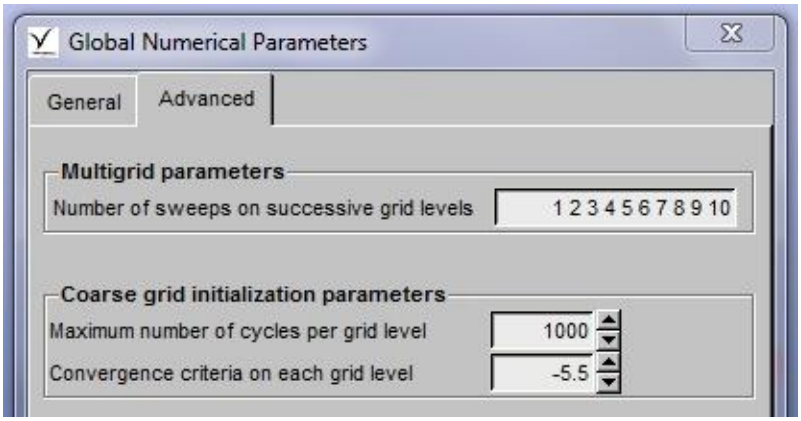

Figure A–3. Multigrid settings. Number of cycles and convergence criteria

The problem of Inlet Diffusion was described in Chapter 4.2.4. The hard coded correction of combustion diffusion coefficient was used by means of OpenLabs. A library in OpenLabs can be set through "Project Parameters => OpenLabs => Resource Manager". Once the code is written, the library has to be built [108].

In current simulations a new definition of combustion diffusion coefficient was introduced to the solver, and the internal definition was overwritten by the new one.

- Two new coefficients were specified for two equations – mixture fraction equation "myDiffCoeff_MF" and mixture fraction variance equation "myDiffCoeff_MFV" – as auxiliary terms. Statement IF-ELSE was used to set the coefficient equal to zero at the first cell of mesh using coordinates.
- New coefficients were used to overwrite the current definitions used by the solver in "=>ALGEBRAIC_DIFFUSION_COEFFICIENTS"
- The internal combustion diffusion coefficient has to be overwritten as a "@TRANSP_PROPERTY" as well, because it's used for "Combustion Mass diffusion calculator"

- The optional settings "->BOUNDARY_UPDATE_PRIORITY: YES" is used to make sure that the newly implemented definitions of combustion diffusion coefficients have higher priority with regards to the internal definitions.

The OpenLabs library is presented below:

```
##############################
# Empty OpenLabs Resource
# (c) NUMECA Int.
##############################

=>CONSTANTS

=>CUSTOM_FLUID_PROPERTIES
@TRANSP_PROPERTY: CombDiffCoef_MF
->EXPRESSION: myDiffCoeff_MF
->BOUNDARY_UPDATE_PRIORITY: YES

@TRANSP_PROPERTY: CombDiffCoef_MFV
->EXPRESSION: myDiffCoeff_MFV
->BOUNDARY_UPDATE_PRIORITY: YES

=>CUSTOM_BOUNDARY_CONDITIONS

=>GLOBAL_QUANTITIES

=>ALGEBRAIC_DIFFUSION_COEFFICIENTS
@ALGDIFFCOEFF: DiffusionCoeff_Mixture_Fraction_Approach
->EXPRESSION(MixtureFractionEquation): myDiffCoeff_MF
->EXPRESSION(VarianceMixtureFractionEquation): myDiffCoeff_MFV

=>EQUATIONS

=>INITIAL_PROFILES

=>SOURCETERMS

=>AUXTERMS
@ myDiffCoeff_MF =  IF ((xCoord>=0.00594 AND xCoord<=0.0061) AND
(zCoord>=0.003 AND zCoord<=0.057)) 0 \
                        ELSE Viscosity/combSchmidtLam_ +
EddyVisc/combSchmidtTurb_
@ myDiffCoeff_MFV =  IF ((xCoord>=0.00594 AND xCoord<=0.0061) AND
(zCoord>=0.003 AND zCoord<=0.057)) 0 \
                        ELSE Viscosity/combSchmidtLam_ +
EddyVisc/combSchmidtTurb_

=>ADDITIONAL_INFORMATION
```

B APPENDIX. INLET DIFFUSION PROBLEM

Inlet diffusion occurs when extra mixture fraction is diffused into the flow when the fluid shears across the fuel inlet rather than the usual case, shown in the Figure B–1, where the mixture fraction in the cells near the boundary is dominated by the convective flux of the adjacent fuel inlet boundary.

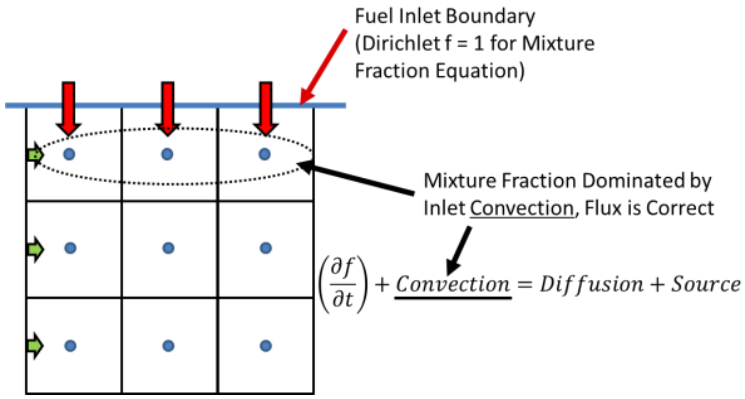

Figure B–1 Convection of fuel flow from inlet dominates the mixture fraction transport in the cells near the boundary, inlet diffusion is not significant in this case.

However, when the convection from the fuel inlet is relatively weak relative to the velocities in the cells near the boundary, and if there exist significant differences in the species concentrations between the inlet faces and the cells adjacent to the boundary, as shown in the figure below, diffusive flux can become significant. In the case of the hybrid rocket motor, extra mixture fraction will be diffused into the flow due to the difference between the mixture fraction specified at the inlet (a Dirichlet-type boundary condition with mixture fraction = 1) and the freestream mixture fraction values.

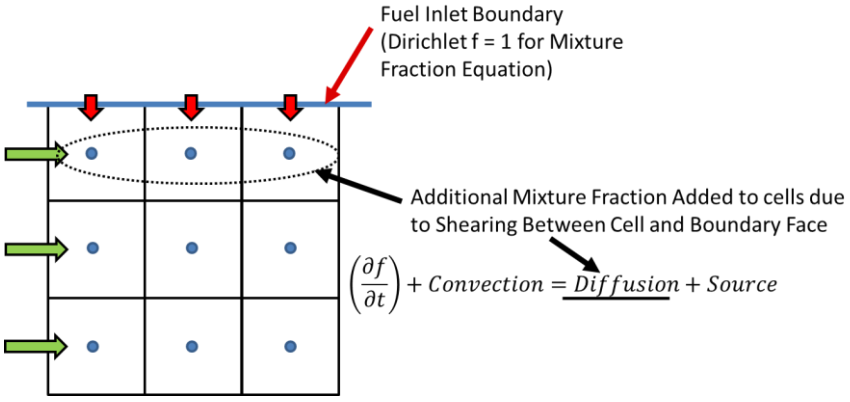

Figure B–2 Extra mixture fraction entering the domain due to diffusion from the fuel inlet into the shearing flow across the boundary face. The flux of mixture fraction into the domain will be higher than the specified convective flux.

There are several potential solutions to this problem, the simplest of these is to derive a convection-only, zero-diffusion boundary condition for the species transport equation that can be assigned to the boundary conditions of any species transport equation as shown in the figure below.

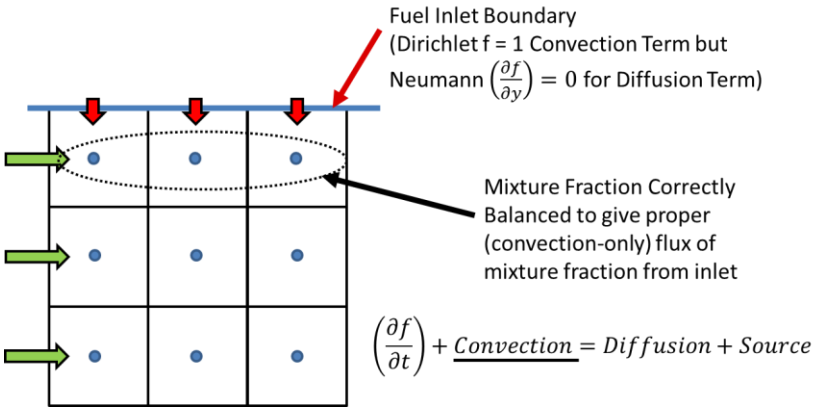

Figure B–3 The most direct method for solving the inlet diffusion problem is to simply implement a boundary condition that specifically negates the diffusive term from the flux calculation at domain boundaries for species transport equations. Unfortunately this is not available in all commercial CFD codes.

This approach for eliminating inlet diffusion via specially-developed boundary conditions has been implemented in some commercial CFD codes such as ANSYS Fluent, as seen in the "options" section of the ANSYS Fluent species model dialogue box.

This type of boundary condition is unfortunately not yet available in FINE/Open so two alternative approaches were devised to work around the problem. Both of these approaches used the OpenLabs extension in FINE/Open to directly manipulate the behavior of the cells adjacent to the fuel boundary. The first of these work-arounds, illustrated in the figure below, consisted of changing the fuel inlet to a solid wall boundary (which always gets a zero-flux boundary condition for the mixture fraction equation) and assigning a source term in the mixture fraction and continuity equations to inject the desired mass of fuel into the cells adjacent to the fuel boundary without the use of an inlet boundary. While this method does add the momentum of the incoming fuel, its momentum is negligible anyway compared to that of the freestream which is what gave rise to the inlet diffusion problem in the first place.

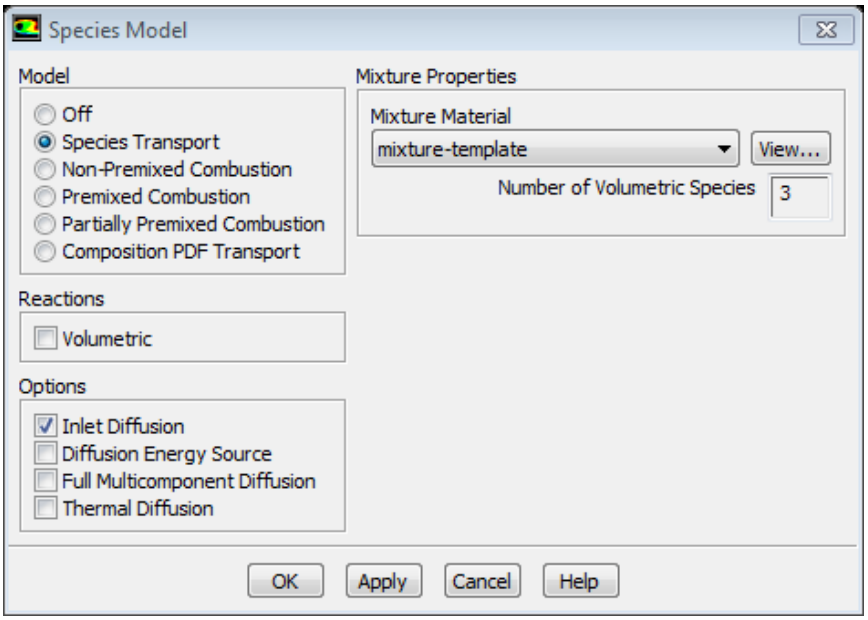

Figure B–4 ANSYS Fluent species model dialogue box showing the "inlet diffusion" checkbox in the "options" section for directly controlling whether the diffusive flux is calculated at domain boundaries for the species transport equations.

This method was very effective at eliminating the inlet diffusion effect, but unfortunately was not compatible with doing simulations of spray combustion since, as of FINE/Open v.4.1, lagrangian particle streams can only be injected at inlet boundaries and not at solid wall boundaries.

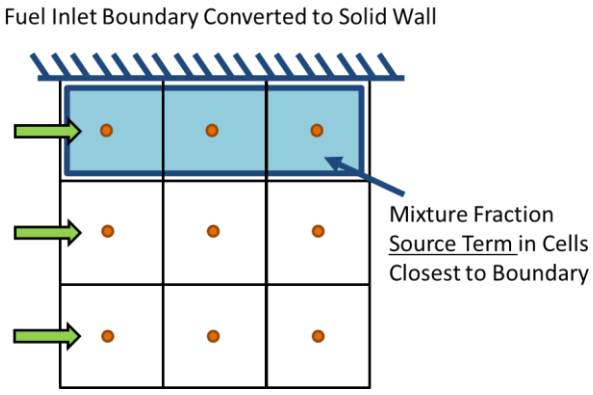

Figure B–5 Demonstration of one of the possible solutions to the Intel diffusion problem – using “wall” boundary condition for the fuel inlet

The next method sought to overcome this limitation by preserving the use of the fuel inlet boundary. This method, illustrated below, also used OpenLabs but this time to modify the diffusion coefficient of the mixture fraction transport equation. Specifically, the diffusion coefficient was set to zero for the cells closest to the fuel inlet boundary.

This method worked well to prevent the inlet diffusion phenomenon from occurring while preserving the presence of the inlet boundary for use with the Lagrangian spray model and also including the correct, albeit small, momentum flux of the incoming fuel.

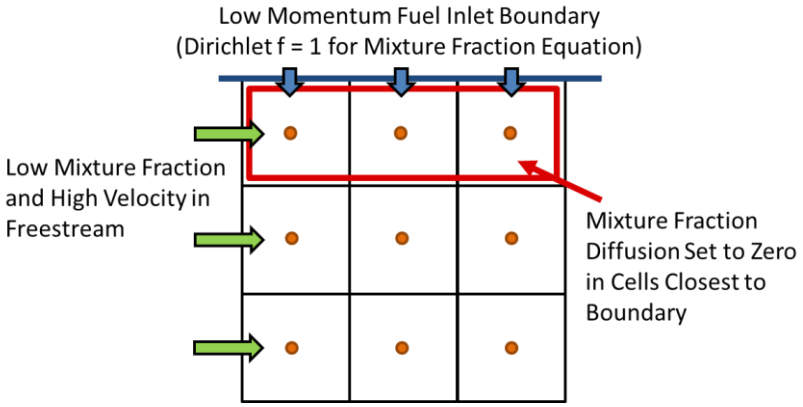

Figure B–6 Illustration of the Inlet Diffusion problem solution for FINE/Open

C Appendix. Correction of the Liquid Fuel Mass Flow Losses

During the first runs of simulations it was observed that about 3-6% of the total liquid mass flow was lost through the fuel inlet. This is first of all possible due to the numerical model assumption that the fuel is simulated as an inlet, thus there can be influxes as well as outfluxes through the inlet. There are two factors that favour this kind of losses.

1. Specific configuration of a hybrid rocket motor implies that the oxidizer is flowing right above the surface of the fuel inlet with a much higher speed than the fuel (see Figure C–1).
2. The reacting flow in HRM is highly turbulent.

These two factors together make it likely for a liquid particle to get a velocity component that would push it towards the fuel inlet, and thus it would flow back through the fuel inlet.

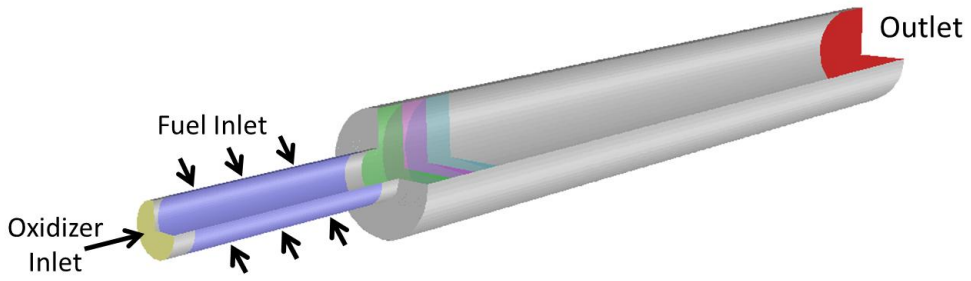

Figure C–1 Configuration of the computational domain

For this reason a correction of liquid mass flows was performed for each simulation. The correction routine consists of the following steps:

1. Run a simulation for 3 lagrangian cycles instead of 22 in order to identify the level of losses for each class $L_{\dot{m}}$. For some simulations lost liquid mass fraction is stabilized even after the first lagrangian cycle (for example, O/F2.2+spray30%, see Figure C–2), but as it's not known beforehand, thus 3 lagrangian simulations were set as satisfying for identification of the amount of losses.
2. Calculate new mass flows assuming that the losses $L_{\dot{m}}$ will remain the same. New mass flow values have to be tuned in a way that the remaining liquid fraction of fuel will satisfy mixture ratio O/F boundary conditions (eq. C–1)

$$\left(\dot{m}_{liquid}\right)_{new} \cdot L_{\dot{m}} = \dot{m}_{liquid} \qquad \text{C–1}$$

3. Set new values of the liquid mass flows, and run full simulation;
4. Check that correction worked well comparing the mass flows calculated by the solver after correction with the value required for the simulation (Table 5–5). According to the output solver data (see example, Figure C–3) the liquid mass flow can be calculated as

$$\left(\dot{m}_{liquid}\right)_{new} = (\text{Mass influx through inlet} - \text{Mass outflux through INL} - \text{Other mass losses}) \cdot 72 \qquad \text{C–2}$$

where Other mass losses include other possible losses such as Mass outflux through EXT, Mass outflux through SOL/MIR, Mass flux of trapped particles, Mass flux of lost particles; multiplication by 72 is required due to the computational domain realization (5 degrees segment, see Chapter 5.1 for details).

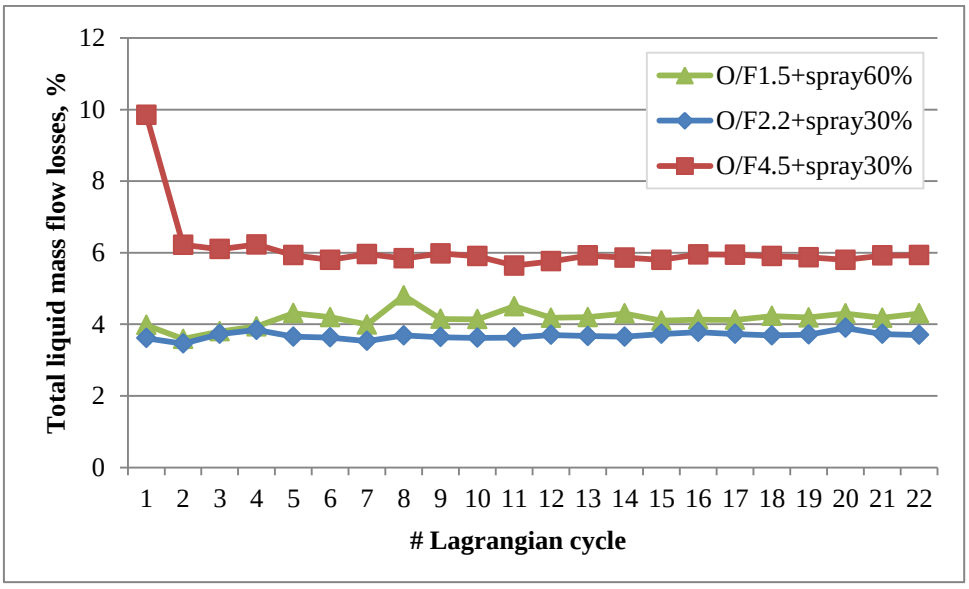

Figure C–2 Losses of the liquid mass flow through the fuel inlet during spray simulation

```
--- Statistics for all classes
------------------------------------------------------------------------------
--- Mean residence length in domain:         0.19127880565 [m]
--- Mean residence time in domain:           0.00708698340163 [s]
---
--- Mass influx through inlet:               1.07211760802e-05 [kg/s]  100.0 %
---
--- Mass outflux through OUT:                2.2821591405e-06 [kg/s]   21.28 %
--- Mass outflux through INL:                3.97301711857e-07 [kg/s]   3.70 %
--- Mass outflux through EXT:                0 [kg/s]     0.0 %
--- Mass outflux through SOL/MIR:            0 [kg/s]     0.0 %
--- Mass flux evaporated:                    8.04171522779e-06 [kg/s]   75.0 %
--- Mass flux of trapped particles:          0 [kg/s]     0.0 %
--- Mass flux of lost particles:             0 [kg/s]     0.0 %
      ---
```

Figure C–3 The lagrangian solver output. Statistics of spray simulation averaged for all classes. Case: O/F2.2+spray30%

An example of correction, see Table C–1, where a case of O/F=2.2 with 30% of liquid fuel fraction is considered. Losses and corrected values of liquid mass flow for each class are reported.

All corrected liquid mass flows for each class of all simulations are reported in the Table C–2.

Table C–1 A case example of corrected liquid mass flows. Losses are also reported. Case: O/F2.2+spray30%

	O/F2.2_spray30%		
	Losses, %	$\dot{m}_{liquid}$ **[kg/s]** (see Table 5–5)	**Corrected** $\dot{m}_{liquid}$ **[kg/s]**
Class #1	11.7	1.042e-4	1.188e-4
Class #2	5	1.711e-4	1.802e-4
Class #3	1.7	1.711e-4	1.744e-4
Class #4	0.85	1.488e-4	1.501e-4
Class #5	0.25	9.672e-5	9.696e-5
Class #6	0.6	5.208e-5	5.239e-5

Table C–2 All corrected mass flows that were used for simulations

	Corrected $\dot{m}_{liquid}$ [kg/s]							
	O/F=1.5		**O/F=2.2**		**O/F=3.42**		**O/F=4.5**	
#class	**30%**	**60%**	**30%**	**60%**	**30%**	**60%**	**30%**	**60%**
1	1.743e-4	3.468e-4	1.188e-4	2.35e-4	7.614e-5	1.571e-4	5.927e-5	1.223e-4
2	2.623e-4	5.27e-4	1.802e-4	3.662e-4	1.171e-4	2.468e-4	9.253e-5	1.976e-4
3	2.557e-4	5.115e-4	1.744e-4	3.511e-4	1.127e-4	2.327e-4	8.826e-5	1.847e-4
4	2.195e-4	4.413e-4	1.501e-4	3.016e-4	9.678e-5	1.97e-4	7.449e-5	1.522e-4
5	1.423e-4	2.846e-4	9.696e-5	1.942e-4	6.247e-5	1.258e-4	4.787e-5	9.686e-5
6	7.684e-5	1.531e-4	5.239e-5	1.044e-4	3.357e-5	6.734e-5	2.559e-5	5.15e-5

D APPENDIX. HYBRID ROCKET MOTOR DESIGN FOR A PRACTICAL APPLICATION

The preliminary design of a rocket motor/engine allows the engineer to evaluate how big and heavy the propulsion would be in order to satisfy certain mission requirements. The calculations presented hereafter follow the preliminary design procedure suggested by R. Humble, 1995 [100].

The fourth stage of launcher Vega, AVUM, was considered for the study.

1. Introduction. AVUM

The VEGA launcher is a 4-stage single-body vehicle consisting of three solid-rocket motor stages (P80, Zefiro-23 and Zefiro-9A) and a liquid-propulsion upper stage, with the following main characteristics [109]:

- Height: 30 m
- Diameter: 3 m
- Liftoff mass: 137 tons
- Payload mass: 1500 kg

The upper module of the Vega is called Attitude and Vernier Upper Module (AVUM) [110] (see Figure D–1). The propulsion module performs the attitude control and axial thrust functions during the final stages of the flight, enabling the payload to be placed in its orbit. Unlike the previous stages, it is equipped with a liquid bipropellant system for primary manoeuvring, that uses nitrogen tetroxide as oxidising agent and unsymmetric dimethylhydrazine as propellant, both of them fed by pressurised Helium, and it has a cold gas attitude control system.

This stage is 1.72 m tall, 1.9 m in diameter and requires a total propellant load of between 250 and 400 kg, depending on its configuration and the mission to be performed.

- Length: 1.742 m
- Max diameter: 1.910 m
- Mass at Lift-off: 1237 kg
- Burn time: 694.5 s
- Total Impulse: 1 702 KN s
- Thrust (vacuum): 2.45 kN
- Structural Ratio: 53.3%

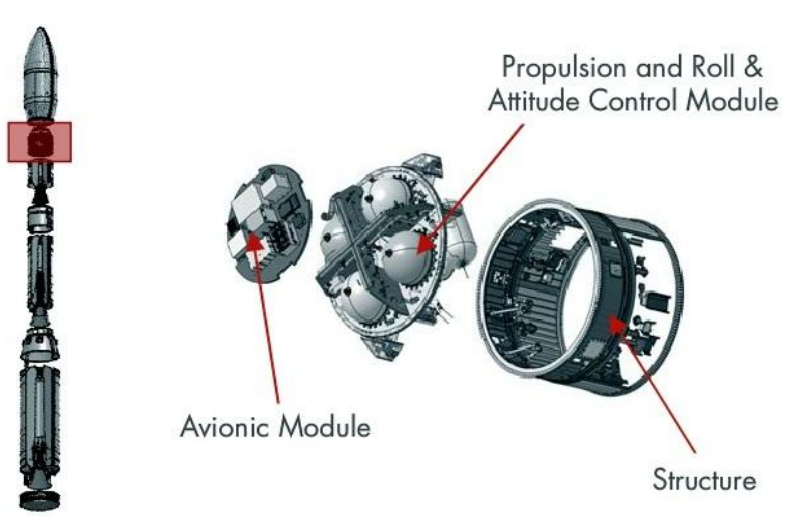

Figure D–1 The fourth stage of Vega – AVUM

2. Mission requirements

The performance is typically described in terms of maneuver ΔV for the stage, range of specific impulse, thrust versus time, or the total impulse.

In order to complete the mission of the fourth stage AVUM [110] by means of a hybrid rocket propulsion system, the performance in terms of maneuver ΔV was chosen as one of major initial requirements for the preliminary design (SSO Mission, Figure D–2). The payload mass of 1500kg must be considered.

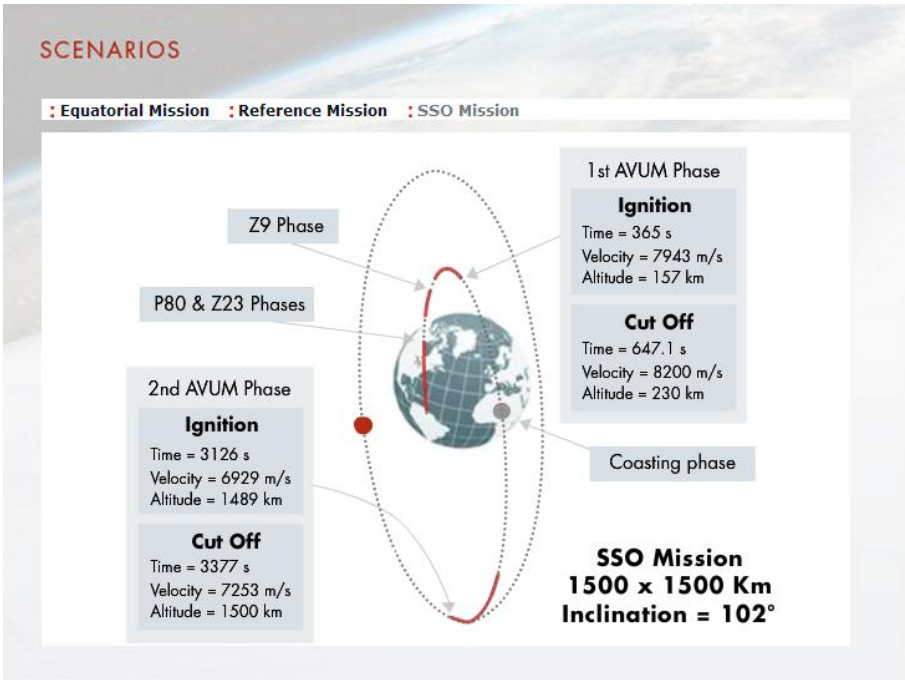

Figure D–2 Mission performance of the Vega's fourth stage AVUM

Mission Requirements:

- ΔV: 581 m/s
- Payload mass: 1500 kg

3. Preliminary design decisions

Propellant

Based on the experimental investigation of thermal, rheological and mechanical properties of paraffin-based fuels (see Chapter 3 "Paraffin-based Fuels: a Way to Increase Regression Rate") the formulation with 15% content of SEBS and 1% content of CB was chosen as a good compromise between rheological, mechanical and ballistic properties. The liquid oxygen is considered as an oxidizer with an assumption that it's preheated and it's gaseous when it enters the combustion chamber. The pair Paraffin+Oxygen is well-storable, non-toxic and not expensive.

Oxidizer-to-fuel ratio O/F

The theoretical performance analysis of the chosen propellant was conducted by means of the software CEA [97]. Considering the fact that O/F ratio in a HRM varies over the burning time from lower values to higher (see Chapter 2.1.2 "HRM characteristics"), the initial O/F ratio was assumed to be constant and equal to 2, which is lower than the O/F that corresponds to the maximum performance; and specific impulse was assumed to be constant, but also slightly lower than the maximum value and equal to 350 s (for the case of combustion chamber pressure = 7 MPa, and nozzle expansion area ratio = 100).

The suggested range of values of the Inert Mass Fraction is 0.16-0.2 (p. 403, [100]). Considering that in this particular case a cryogenic type of oxidizer (LOx) is used and taking into account that the inert mass fraction of the AVUM stage is 0,53, so be more realistic, let's assume a value which is in the range 0.2-0.53 and let it be equal to 0.4.

Preliminary Design Decisions:

- Propellant: SW84-SEBS15-CB1 + LOx
- Oxidizer / Fuel ratio O/F: 2
- Specific Impulse Isp: 350 s
- Characteristic velocity c^*: 1800 m/s
- Inert Mass Fraction: 0.4

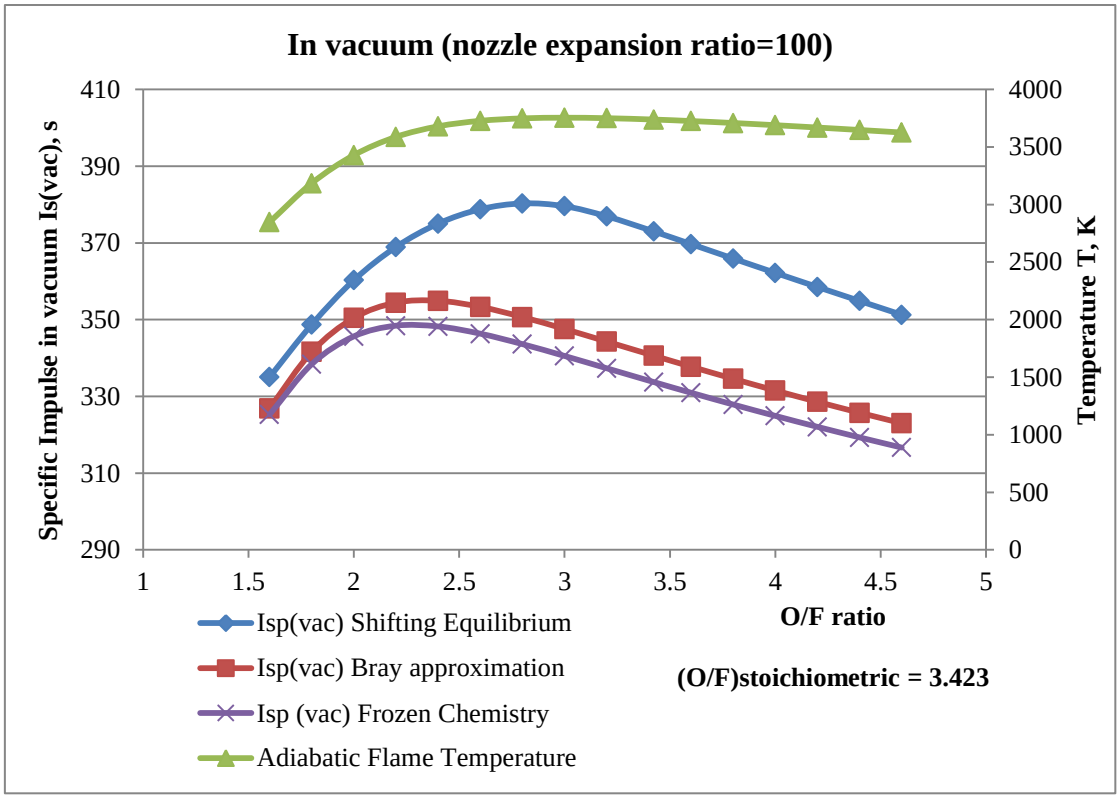

Figure D–3 Theoretical characteristics for a hybrid rocket motor obtained by means of CEA. The motor is utilizing paraffin-based fuel strengthened by SEBS, and is considered to work in space. Combustion pressure is 7MPa, nozzle expansion area ratio is 100

4. Size the propulsion system

Starting from ideal rocket equation the required input data is:

1. Payload mass m_{pay}: 1500 kg
2. Specific Impulse I_{sp}: 350 s
3. ΔV: 581 m/s
4. Inert mass fraction f_{inert}: 0.4

The required propellant mass:

$$m_{prop} = \frac{m_{pay}\left(e^{\frac{\Delta V}{I_{sp}g_0}} - 1\right)(1 - f_{inert})}{1 - f_{inert} \cdot e^{\frac{\Delta V}{I_{sp}g_0}}} \qquad \text{D–1}$$

$$m_{prop} = 316\ kg$$

The inert mass:

$$m_{inert} = \frac{f_{inert}}{1 - f_{inert}} \cdot m_{prop} \qquad \text{D–2}$$

$$m_{inert} = 211\ kg$$

The fuel mass:

$$m_{fuel} = \frac{m_{prop}}{1 - O/F} \qquad \text{D–3}$$

$$m_{fuel} = 106\ kg$$

The oxidizer mass:

$$m_{ox} = m_{prop} - m_{fuel} \qquad \text{D–4}$$

$$m_{ox} = 210\ kg$$

The volumes required to hold these masses:

$$V_{fuel} = \frac{m_{fuel}}{\rho_{fuel}} \qquad \text{D–5}$$

$$V_{fuel} = 0.118\ \ m^3$$

$$V_{ox} = \frac{m_{ox}}{\rho_{ox}} \qquad \text{D–6}$$

$$V_{ox} = 0.184\ m^3$$

where $\rho_{fuel} = 900\ \frac{kg}{m^3}$ and $\rho_{ox} = 1140\ \frac{kg}{m^3}$ are densities of the fuel (Solid Wax + SEBS + CB) and the oxidizer (Liquid oxygen) respectively.

The initial propellant flow rate:

$$\dot{m}_{prop} = \frac{T_{motor}}{I_{sp} g_0} \qquad \text{D–7}$$

$$\dot{m}_{prop} = 0.857\ {}^{kg}/_{s}$$

where T_{motor} is thrust, $T_{motor} = 2450\ N$ (RD-xxx, reference). Considering the fact that thrust is decreasing in a Hybrid engine due to the combustion process, 20% of margin has been applied $T_{motor} = 2450 + 20\% = 2940\ N$.

Once the O/F is known, determine the fuel and oxidizer flow rates:

$$\dot{m}_{fuel} = \frac{\dot{m}_{prop}}{1 + O/F} \qquad \text{D–8}$$

$$\dot{m}_{fuel} = 0.286\ {}^{kg}/_{s}$$

$$\dot{m}_{ox} = \dot{m}_{prop} - \dot{m}_{fuel} \qquad \text{D–9}$$

$$\dot{m}_{ox} = 0.571\ {}^{kg}/_{s}$$

For a small stage and for fuel masses less than 700kg, the simplest design of the fuel grain is preferable. For the fuel mass equal to 100kg the volumetric efficiency is around 75% (p.412 [100]). Thus, cylindrical single port shape of the grain was considered for further calculations.

The initial port area:

$$A_{port.init} = \frac{\dot{m}_{ox.init}}{N \cdot G_{ox.init}} \qquad \text{D–10}$$

$$A_{port.init} = 1.269 \cdot 10^{-3}\ m^2$$

$$G_{fuel.init} = \frac{\dot{m}_{fuel.init}}{N \cdot A_{port.init}} \qquad \text{D–11}$$

$$G_{fuel.init} = 225\ kg/m^2 s$$

where $G_{ox.init}$ – initial oxidizer flux, $kg/m^2 s$ (initial oxidizer flux $G_{ox.init}$ has upper limit between 350-700 kg/m^{2}s. It's been assumed that $G_{ox.init} = 450\ kg/m^2 s$.)

N – number of ports (according to the chosen design of the fuel grain the number of ports is N=1).

The initial port diameter:

$$D_{port.init} = \sqrt{\frac{4 \cdot A_{port.init}}{\pi}} \qquad \text{D–12}$$

$$D_{port.init} = 0.04 \ m$$

The port's length:

$$L_{port} = \left[\left(\frac{\dot{m}_{fuel.init} \cdot \pi^{n-1}}{a \cdot \left(4 \cdot \dot{m}_{prop.init}\right)^{n} \cdot \rho_{fuel}}\right) D_{port.init}^{2n-1}\right]^{\frac{1}{m+1}} \qquad \text{D–13}$$

$$L_{port} = 0.887 \ m$$

Assuming that at the end of the burn, the entire volume of fuel is consumed and the port's length does not change, the final port diameter is defined as

$$D_{port.fin} = \sqrt{\frac{4 \cdot \dot{m}_{fuel}}{\pi \cdot L_p \cdot \rho_{fuel} \cdot N} + D_{port.init}^2} \qquad \text{D–14}$$

$$D_{port.fin} = 0.413 \ m$$

Size and configure components

Nozzle

From the characteristic velocity equation, the throat area is defined as

$$A_t = \frac{\dot{m}_{prop} \cdot c^*}{P_{cc}} \qquad \text{D–15}$$

$$A_t = 2.203 \cdot 10^{-4} \ m^2$$

The nozzle exit area:

$$A_e = A_t \varepsilon_{nozzle} \qquad \text{D–16}$$

$$A_e = 0.022\ m^2$$

where characteristic velocity $c^* = 1800\, m/s$; combustion chamber pressure $P_c = 7\ MPa$; expansion ratio $\varepsilon_{nozzle} = 100$ (design assumption).

Throat and exit diameters:

$$D_t = \sqrt{\frac{4A_t}{\pi}} \qquad \text{D–17}$$

$$D_t = 0.017\ m$$

$$D_e = \sqrt{\frac{4A_e}{\pi}} \qquad \text{D–18}$$

$$D_e = 0.167\ m$$

A conical nozzle with a 15° half angle is used for the sake of simplicity; the length of the nozzle is defined as

$$L_{nozzle} = \frac{D_e - D_t}{2tan(15^\circ)} \qquad \text{D–19}$$

$$L_{nozzle} = 0.281\ m$$

In case of a hybrid propulsion system the length of the **combustion chamber** is literally the length of the fuel grai, but an additional space is needed for the aft mixing section and an injector section. The typical rule for the pre-chamber and the aft mixing chamber is 0.5-1.0 of the grain diameter (Fig. 2.3).

$$L_{cc} = L_{port} + (0.6 + 0.6)D_{port.fin} \qquad \text{D–20}$$

$$L_{cc} = 1.383\ m$$

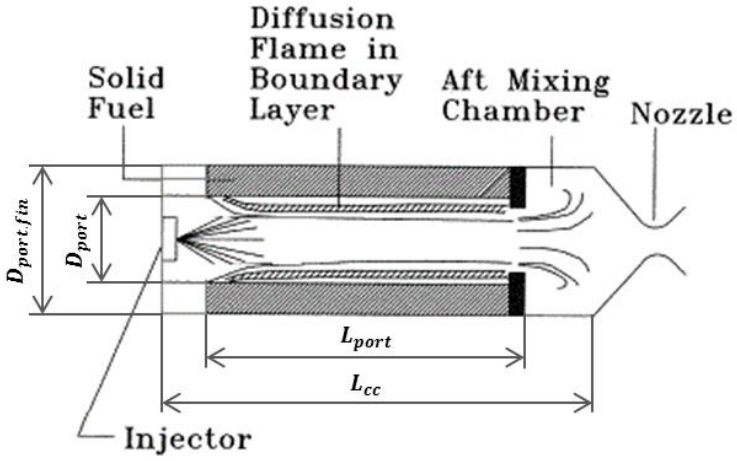

Figure D–4 Scheme of a hybrid rocket motor combustion chamber. Pre-chamber and aft mixing chamber are also shown

Oxidizer tank

The total volume required for the oxidizer $V_{tank.ox} = 0.192\ m^3$ can be stored in 4 spherical tanks. Thereby the diameter of each single spherical tank is

$$D_{tank.ox} = 0.451\ m$$

If using helium pressurant system the total volume of the pressurant required is $V_{pressurant} = 0.031\ m^3$. As well as the oxidizer, the pressurant can be stored in 4 spherical tanks. In this case the diameter of each tank is

$$D_{pressurant} = 0.245\ m$$

The dimensions of a hybrid rocket motor are summarized and confronted in the Table D–1. As can be seen hybrid propulsion system can be fit into existing geometry of the fourth stage of Vega – AVUM. As well as overall dimensions, the total propellant mass lies in the range of the typical propellant mass load for the mission.

Table D–1 Dimensions of AVUM stage confronted with a hybrid propulsion system considered as a possible substitution

AVUM stage length	HRM length (CC + nozzle)
1.742 m	1.664 m
AVUM stage diameter	The overall diameter of the HRM fuel grain + oxidizer tanks
1.910 m	1.315 m
AVUM propellant mass	The HRM propellant mass
250-400 kg	316 kg

5. Performance simulation

The burn of the designed hybrid motor was simulated. Evolutions of the performance parameters such as specific impulse and trust over the burning time were obtained.

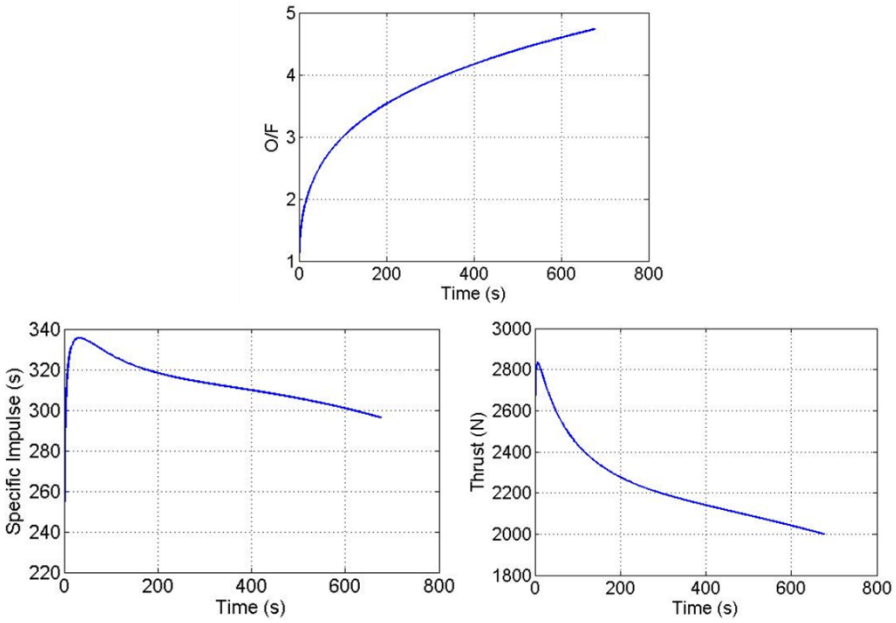

Figure D–5 HRM performance simulation. Oxidizer-to-fuel ratio, specific impulse and trust are reported

Conclusions

The preliminary design study shows that a hybrid propulsion system can be fit into the existing dimensions of the fourth stage of Vega – AVUM, as well as its propellant mass, while meeting the performance requirements in terms of ΔV. The payload mass (1500kg) and the thrust level are maintained.

In terms of propellant costs, overall simplicity of the propulsion system, safety due to the separated propellant components, a hybrid rocket motor is a competitive alternative for an upper stage of a launcher.

A cryogenic oxidizer, like liquid oxygen, is not the simplest type of oxidizer to handle with. It requires a thermal protection. Therefore, other kinds of oxidizers such as nitrogen tetroxide (N2O4) could be also considered.